TOKYO METROPOLITAN UNIVERSITY

首都大学東京

DOCTORAL THESIS

Experimental Study on Influences of Riblets on Laminar-Turbulent Transition and Dependence of Wall Turbulence Generation on Disturbance Nature

Author:
HO Quang Huy

Supervisor:
Prof. Dr. Masahito ASAI

A thesis submitted in fulfillment of the requirements
for the degree of Doctor of Philosophy

in the

Graduate School of Systems Design
The Department of Aerospace Engineering

Tokyo, October 2018

TOKYO METROPOLITAN UNIVERSITY

Abstract

Faculty of Systems Design
The Department of Aerospace Engineering

Doctor of Philosophy

Experimental Study on Influences of Riblets on Laminar-Turbulent Transition and Dependence of Wall Turbulence Generation on Disturbance Nature

by HO Quang Huy

Control of laminar-turbulent transition in boundary layers is one of key technologies to reduce aerodynamic drag of aircraft. Lots of theoretical, experimental and computational studies have been conducted and our knowledge on the mechanism of boundary-layer transition has been much improved for the last few decades. However, some fundamental problems have still remained open to control the transition process. The present thesis deals with some problems related to drag reduction and the underlying mechanisms. The main objective of this thesis is to clarify effects of riblets which are often used for drag reduction of wall turbulence on the instability and transition of boundary layer. Detailed experiments were conducted on the Blasius boundary layer with zero pressure gradient in a low turbulence wind tunnel and a low turbulence channel flow equipment. The thesis consists of five chapters.

Chapter 1 describes the background and objective of the present study, the related work on the boundary-layer instability and transition, and recent studies on wall turbulence and drag reduction by riblets.

Chapter 2 discusses the experimental work on influence of small-sized riblets on the streamwise growth of Tollmien-Schlichting (T-S) waves, which was conducted in a channel flow. Riblets having triangular ridges and trapezoidal valleys, with a height-to-width ratio of 0.5, were used. The result showed that the streamwise riblets had a strong destabilizing effect and reduced the critical Reynolds number for the linear instability by more than 25%. It was also found that when the riblets were inclined to the streamwise direction, the critical Reynolds number increased as the oblique angle ϕ of

riblets. For $\phi \geq 45^\circ$, the riblets had no noticeable influence on the structure of T-S wave and the growth rates were the same as those in the smooth-wall case.

Chapter 3 describes the experimental work on influences of streamwise riblets on the lateral growth of turbulent region localized in span in a boundary layer. The optimal-geometry riblets with drag-reducing size in wall turbulence were used. The lateral spreading angle of the outer edge of laminar-turbulent interface, which approached about 10° in the downstream over the smooth wall, was reduced only by 0.5° by riblets, despite of the destabilizing effect of riblets mentioned in Chapter 2. Thus, the effect of riblets was weak on the lateral turbulent contamination.

Chapter 4 discusses the mechanism of wall turbulence through the experiment on instability and breakdown of a low-speed streak initially forced by disturbances whose frequency-spectrum was similar to that of wall turbulence. Turbulent velocity fluctuations having various spanwise coherencies were used as the forcing signals to excite the streak instability. The results showed that the magnitude of the sinuous instability mode excited was dependent on the initial disturbances, but not very strongly. That is, the magnitude of the sinuous instability mode excited by turbulence components was about 75% of that in the case of anti-symmetric forcing which gave the largest magnitude. Thus the results strongly suggest that fluctuations existing in wall turbulence is rather effective for exciting the streak instability.

Chapter 5 summarizes the important findings described in Chapters 2 to 4.

Contents

List of Figures

Acknowledgements

I take this opportunity to express my sincere gratitude to many people, who so generously contributed to the work presented in this thesis. First and foremost, I want to thank my advisor, Prof. Masahito Asai for the continuous support of my PhD. study and research, for his patience, enthusiasm, and immense knowledge. In all the time of my PhD. course, he taught me fundamentals of conducting scientific research in the fluid dynamics area. Under his supervision, I learned how to define a research problem, find a solution to it, and finally publish the results. Throughout my thesis-writing period, he provided encouragement, sound advice, good teaching, good company, and lots of good ideas. I would have been lost without him. I could not have imagined having a better advisor and mentor for my PhD. study.

Besides my advisor, I would like to thank the rest of my thesis committee: Prof. Masaharu Matsubara (Shinshu University), Prof. Toshio Tagawa (Tokyo Metropolitan University), and Assoc. Prof. Ayumu Inasawa (Tokyo Metropolitan University), for their insightful comments and encouragement, but also for the hard question which incented me to widen my research from various perspectives. I also would like to convey my gratitude to Prof. Naoyuki Watanabe who together with Prof. Masahito Asai went to Vietnam to interview and accept me as a grantee of Asian Human Resources Fund.

In additions, I am also very grateful to Prof. Shohei Takagi, Assoc. Prof. Ayumu Inasawa and Assit. Prof. Hiroshi Ozawa for their support, training especially in the understanding about experimental facilities and meaningful discussion during my times in Fluid Dynamics Laboratory. My sincere thanks also goes to Ms. Yoshiko Uemura for her kind assistance in many of my administrative documents. The PhD. course would not have come to a successful completion, without the help I received from the staff of the Hino Campus and International Office of Tokyo Metropolitan University (TMU). I specially thank Ms. Akemi Ohira for her kind effort to help me to complete many documents related to house renting in Hino. I also received helpful support from Ms. Mari Suzuki in the last graduation procedures. My appreciation is also extended to the former and current long-list lab members of Fluid Dynamics Laboratory. I remember sleepless nights we were spending at lab before deadlines, and for all the fun we have had in the parties and campus life. In particular, I am grateful to Dr. Mochamad Dady Ma'mun, Dr. Masashi Kobayashi, Dr. Ressa Octavianty and current doctoral student Mr. Takaaki Abo for great companionship.

Moreover, I gratefully acknowledge the funding sources that made my PhD. work possible. I really appreciate the financial support from Tokyo Metropolitan Government through "Asian Human Resources Fund" Scholarship Program. This program also helped me to expand the relationships with other international students at TMU.

I would like to thank Dr. Pham Nguyen Hung and all my colleagues in Power Engineering Consulting Joint Stock Company 1, Vietnam Electricity Corporation for their supports. Not forgetting Vietnamese friends in TMU for memorable time spent together, for their encouragements and sharing. I am very much indebted to Mr. Kyota Takahashi and his wife, Mrs. Chiharu Takahashi, they have been very kind, patient and always willing to help us whenever we approached them. I acknowledge and appreciate them as my Japanese parents for all their efforts.

Last but not the least, I would like to express my deepest gratitude to my family members. For my parents, Ho Quang Thanh and Vu Thi Mai Duyen, who raised me with a love of science and supported me in all my pursuits. For my two twin younger brothers, Ho Quang Son and Ho Quang Truong, who understand all my habits and hobbies. And for my wife, Nguyen Thanh Thuy and two beloved daughters, Han Nhi and Hato, who always give me the extra love, strength and motivation to get things done. This thesis is dedicated to them...

Chapter 1

Introduction

1.1 Background of transition and turbulent research: Engineering and scientific aspects

"Wall-bounded shear flows" such as *"boundary-layer"* and *"channel and pipe"*, are of typical through-flow system highly dependent on background turbulence conditions. When the Reynolds number increases, they undergo transition to turbulence, depending on the intensity, spectrum and other nature disturbances existing in the flow. Especially, focusing on the boundary layer on the aircraft wing, the flow state *laminar* or *turbulent* strongly affects the aerodynamic performance such as aerodynamic drag and maximum lift as well as aerodynamic noise. Therefore, transition from laminar to turbulent has received great interests not only scientifically but also in practical applications, in aerospace engineering and automotive engineering. As seen in Figure 1.1, the flow over a wing surface generally includes laminar, transitional and turbulent regimes. Turbulent regime has much larger velocity gradient at the wall due to very strong mixing by turbulent vortices and much larger wall shear stress/friction, thus leading to occurrence of very large friction drag compared to that in the laminar regime. Therefore, in boundary layers on the airplane wing, transition location from laminar to turbulent is a key factor for reduction of aerodynamic drag or fuel consumption, bringing economical as well as environmental benefits.

In natural environments, onset of transition from laminar to turbulent is affected by multiplicity of factors [1] such as aircraft speed (Mach number,

Reynolds number), structural geometry (shape, size of airfoils), surface conditions (waviness, smoothness, imperfections) and flight atmospheric environments. Based on understanding of these factors, efforts have been made to reduce aircraft drag by delaying the transition and thus maintaining laminar flow. Natural Laminar Flow (NLF) technology is one of the most important passive drag reduction technologies in which the wing shape is designed to extend weak favorable-pressure-gradient and zero-pressure-gradient region toward as far downstream as possible at a cruse condition. Concerning active drag reduction technologies, on the other hand, Laminar Flow Control (LFC) such as wall suction, cooling or vibrating have been considered and applied to the aircraft wing, and some remarkable successes were obtained in flight experiments and wind tunnel testing. For applications of NLF and LFC, see series of review papers by author group from NASA Langley Research Center [2–4]. Here, it is emphasized that influences of the complex impact of environmental factors, *e.g.* turbulence, noise, sound, icing, insects, dirt on transition process remains unsolved and is one of the important fluid dynamics problems in aerospace engineering.

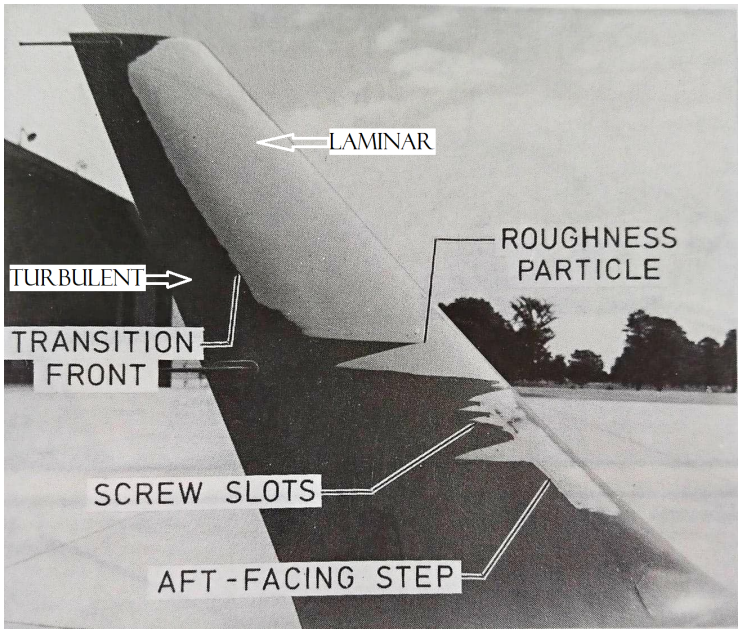

FIGURE 1.1: Boundary-layer transition on a winglet surface (from Obara (1988) [5]).

Laminar-turbulent transition process in boundary-layer is generally divided into three important phases: receptivity, disturbance amplification due

to flow instabilities, and wave breakdown into wall turbulence. *Receptivity* is the process by which disturbances in the external environment penetrate into the boundary layer and generate the initial disturbance of the boundary-layer instability. In second phase, a series of instability stages occurs in a particular path depending on the nature of external disturbances. When the magnitude (amplitude) of initial disturbances is sufficiently small, transition begins with a linear instability to 2-D traveling waves (primary instability waves) known as Tollmien-Schlichting (T-S) waves, followed by non-linear instability stage with the consecutive formation and breakdown of 3-D (Λ-shaped) vortical structures (which is recognized as the secondary instability [6, 7]), and goes to the final stage consisting of the appearance of near-wall low-speed streaks and their breakdown into wall turbulence structures. Transition in this path is often called the classical transition and can be observed in zero-pressure-gradient or weak pressure-gradient boundary layers under very weak background turbulence (usually with turbulent intensity less than 0.1%). With increasing the intensity of background (free-stream) disturbances, transition may skips linear instability stage and is directly caused by occurrence and growth of low-speed streaks right after the receptivity process in the leading-edge region. Therefore, this type of transition is referred to the bypass transition. At the next phase of the bypass transition, low-speed streaks undergo the so-called streak instability causing an oscillatory motion of low-speed streaks and subsequently breakdown into quasi-streamwise vortices often leading to formation of turbulent spots.

The brief description above also emphasized important roles of external disturbances triggering the transition for all the phases of boundary-layer transition process. The environmental factors include free-stream turbulence (vortical disturbances), acoustic disturbances such as engine noise, and surface/roughness conditions (see Figure 1.2). Free-stream turbulence is characterized by its intensity, scales and coherence and can be considered not only as a source of disturbances triggering the initial stage of the transition but also a factor influencing the instability phenomena in the late stage of the transition.

Another route in the bypass transition is roughness-induced transition. Single roughness can directly cause the formation of turbulent wedge if its size in particular its height is large enough to generate strong vortices directly behind the roughness. In such a case, the roughness Reynolds number R_k defined as kU_k/ν where k is the roughness height, U_k the velocity of

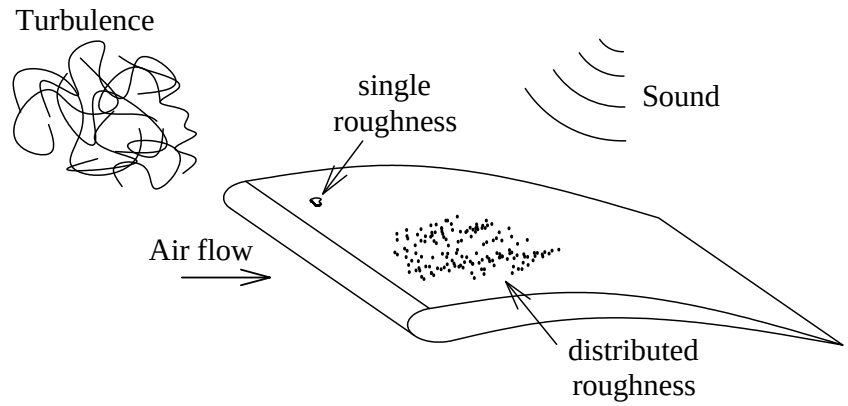

FIGURE 1.2: Disturbance environment affecting laminar-turbulent transition.

boundary layer at the height of the roughness and ν the kinematic viscosity is considered to be a key parameter: The critical value of R_k for occurrence of transition is often cited to be 25 [8, 9]. Here, concerning roughness effects on transition, it should also be mentioned that distributed roughness can delay or amplify the growth of T-S waves.

The following section will provide more details of boundary-layer transition process concerning the present study.

1.2 Laminar-turbulent transition in boundary layers

The well-known pipe-flow experiment by Osborne Reynolds (1883) [10] was the first of the transition research. He observed that the flow in pipe becomes unstable and changes from laminar (non-mixing) motion to highly-mixing motion (turbulence) at a certain critical value of the parameter, later defined as Reynolds number, $Re = Ud/\nu$, where U is free-stream velocity, d the pipe diameter and ν the kinematic viscosity. He also shown that the critical Reynolds number increased when disturbances in the pipe entrance was reduced. Theoretically, from 1880 to 1917, Lord Rayleigh studied the stability of inviscid circular flow between two concentric cylinders [11–15] and stated that the instability could occur only if an inflectional point appeared in velocity profile, this statement is called the Rayleigh's stability criterion,

but it could not explain the transition in boundary-layer in which the velocity profile has no inflection point. The effects of viscosity was added in the equations by Orr (1907) [16] and Sommerfeld (1908) [17] to describe linear two-dimensional modes of disturbance to a viscous parallel flow. This equation was latter referred to as the Orr-Sommerfeld equation. Tollmien in 1929 [18] and Schlichting in 1933 [19] first solved that equation to two-dimensional wave disturbances for the flat-plate boundary-layer and obtained the critical Reynolds number. The most unstable eigen-mode of the Orr-Sommerfeld equation was later called Tomien-Schlichting (T-S) wave. In 1940s, Schubauer & Skramstad [20] verified experimentally the amplification of T-S waves predicted theoretically in a low-turbulence-level wind tunnel. Importantly, they introduced a disturbance artificially by using mechanical vibrations into the boundary-layer along a smooth flat-plate and showed that T-S waves gradually increased in amplitude downstream, leading to the transition to turbulence.

On the other hand, the concept of bypass transition came after Morkovin's statement (1969) that "we can bypass the T-S mechanism altogether if we can replace it with another strongly amplifying mechanism" [21]. Today, more than a century has passed since the experiment of O. Reynolds, many important features to complete the transition process were revealed both for the classical and bypass transition processes. The detail of such features will be described in the following subsections.

1.2.1 Transition initially caused by T-S waves

A laminar-to-turbulent transition process in boundary-layer over a flat plate can be schematically illustrated in Figure 1.3. The basic sketch was introduced by Schlichting in his great book "Boundary Layer Theory" [22] for transition in a flat-plate boundary-layer. It should also be noted that the same path of transition also can be observed in a plane channel flow with low background turbulence [23–25]. This path of transition process is referred to as path A in review paper by Saric *et al.* [26]. It generally includes 6 stages as listed in the caption of Figure 1.3 (number and name of stages of transition process may be different depending on the viewpoint of researchers).

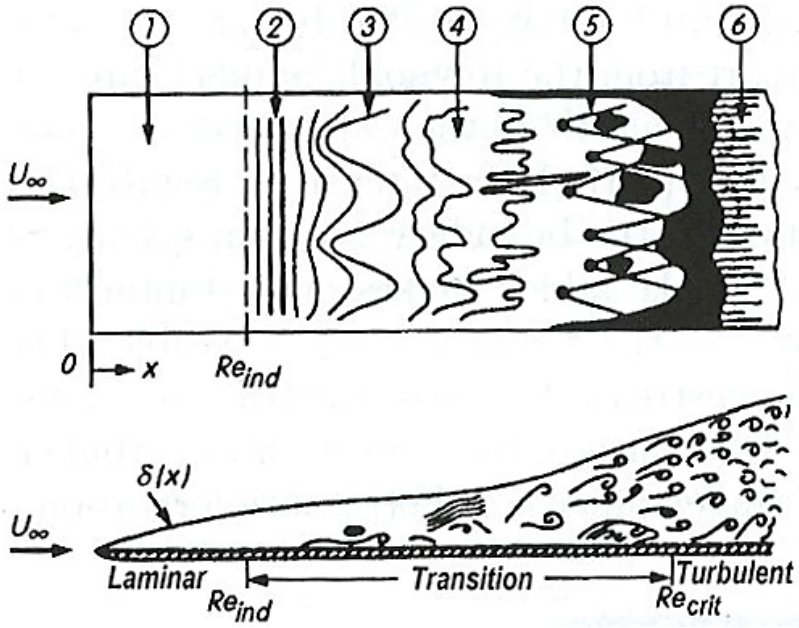

FIGURE 1.3: Sketch of laminar-turbulent transition in the boundary-layer on a flat-plate at zero incidence (from Schlichting (2000) [22]). (1) Stable laminar flow near leading-edge; (2) Unstable 2D Tollmien-Schlichting waves; (3) Development of 3D unstable waves (Λ vortices) and "hairpin" eddies; (4) Wave breakdown at regions of high localized shear and streak formation; (5) Formation of turbulent spots and lateral contamination; (6) Fully turbulent flow

As mentioned in Section 1.1, the first stage of the transition is the receptivity process (coined by Morkovin [27]). During this process, external disturbances penetrate into the boundary layer and prepare (produce) the initial disturbance developing to the eigen-mode of the Orr-Sommerefeld equation [28]. Receptivity process is the wavelength conversion process in which a long wavelength external disturbance (such as sound and free-stream disturbances) are converted to a shorter-wavelength T-S wave with the same frequency. According to Saric *et al.* [29] "Receptivity has many different paths through which to introduce a disturbance into the boundary layer. They include the interaction of freestream turbulence and acoustic disturbances (sound) with model vibrations, leading-edge curvature, discontinuities in surface curvature, or surface inhomogeneities". In the case of flat-plate boundary layer, the important receptivity region is the leading edge region in which an oscillating Stokes Layer induced by external disturbance can develop to T-S wave. As for detail in the leading-edge receptivity to freestream disturbances, see the review paper by Saric, Reed & Kerschen [26].

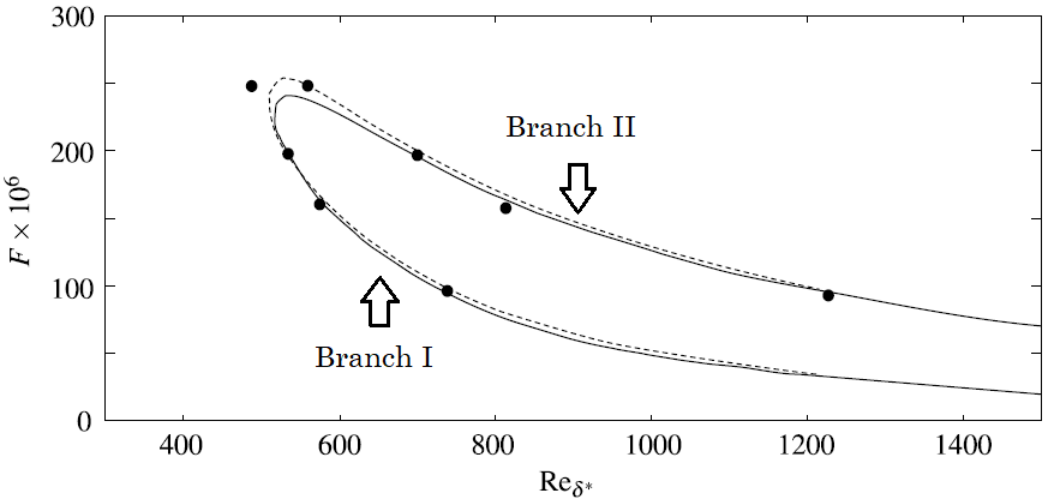

FIGURE 1.4: Neutral stability curve for the Blasius boundary layer (from Boiko (2012) [31]). (•) Experimental data obtained by Klingmann *et. al.* (1993) [32]; Solid and dashed line represent the parallel linear stability theory and non-parallel linear stability theory of Gaster (1974) [33].

In the instability stage, of importance for the onset of primary instability is the critical Reynolds number Re_{cr}. For $Re < Re_{cr}$ the flow always remains laminar and any disturbance is damped in this case. In flat-plate boundary-layer, Re_{cr} was first theoretically predicted by Tollmien in 1929 [18] and Schlichting in 1933 [19] by solving Orr-Sommerfeld equation. Today, under weak disturbance environments, referring to the neutral stability curve calculated by linear stability theory, we understand that $Re_{cr} = Re_{L,\delta^*} = U_e\delta^*/\nu \approx 520$ where δ^* is the displacement thickness and U_e is the freestream velocity. As mentioned before, the linear stability theory was verified experimentally by Schubauer & Skramstad (1943) [20]. They succeeded to prepare very good experimental facility/setup and introduced some advanced experimental techniques. In their experiment, turbulent level at the test section was only $Tu = 0.01 - 0.03\%$, much lower than in any other wind tunnel at that time. In addition, they introduced well-controlled small-amplitude disturbances with mono-frequency by means of the so-called vibrating-ribbon technique and performed measurements using hot-wire anemometer. These techniques have widely been accepted in the society of transition research even now. Their experiment showed qualitative agreement with the theoretical results by Schlichting [30] and founded a classical basis of the transition research in boundary layers.

Figure 1.4 illustrates the neutral stability curve for the Blasius boundary

layer. T-S waves are first damped and then, after reaching the branch I of the neutral stability curve, T-S waves begin to grow. The amplitude of T-S wave gradually increases until the T-S wave reaches the branch II and then T-S wave decays again. Therefore in order to reach the next stage of the transition, that is, onset of the secondary instability leading to 3-D wave growth, the T-S wave has to be amplified to some critical (threshold) amplitude between the branch I and branch II.

The threshold amplitude of T-S wave for onset of the secondary instability was presented by Herbert (1983) [34] and Orszag & Patera (1983) [7] theoretically. They considered the streamwise periodic flow produced by finite-amplitude 2-D T-S wave in plane Poiseuille flow and analyzed its linear instability to 3-D disturbances using the Floquet theorem. Especially, Herbert analyzed two kinds of instability modes, *i.e.*, the fundamental mode leading to the ordered peak-valley wave structure (the ordered array of Λ vortices in the streamwise direction) and the subharmonic modes (symmetric and anti-symmetric modes) leading to the staggered array of Λ vortices. Development of the fundamental and subharmonic modes are visualized in Blasius boundary layer by Saric & Thomas (1984) [35]. Another 3-D mode, *i.e.*, a resonant triad mode was found by Craik (1971) [36]. These three modes are called K-type after the detailed experiment of Klebanoff, Tidstrom & Sargent (1962) [37] for a Blasius boundary-layer, H-type after Herbert [34] and C-type after the theoretical prediction by Craik [36], respectively. Here, the subharmonic wave growth was first observed experimentally by Kachanov, Kozlov & Levchenko [38]. These secondary instability modes have different critical (threshold) amplitudes of 2-D T-S wave above which they can grow, that is, about 0.7% for K-type mode, about 0.4% for H-type and 0.3% for C-type, respectively, in terms of maximum rms value of streamwise velocity fluctuation.

When the three-dimensional wave growth proceeds, the wave breakdown occurs, as first observed by Klebanoff *et al.* [37], Hama & Nutant [39] and Kovasznay, Komoda & Vasudeva [40]. In this stage, the Λ-vortex structure forms a three-dimensional high-shear layer away from the wall and eventually breaks down into smaller-scale (high-frequency) hairpin vortices, which is called the high-frequency secondary instability or the tertiary instability. Similar stages of the secondary instability and breakdown into hairpin vortices were realized in plane Poiseuille flow and the detailed flow structures in this transition process were demonstrated by Nishioka, Asai & Iida (1981)

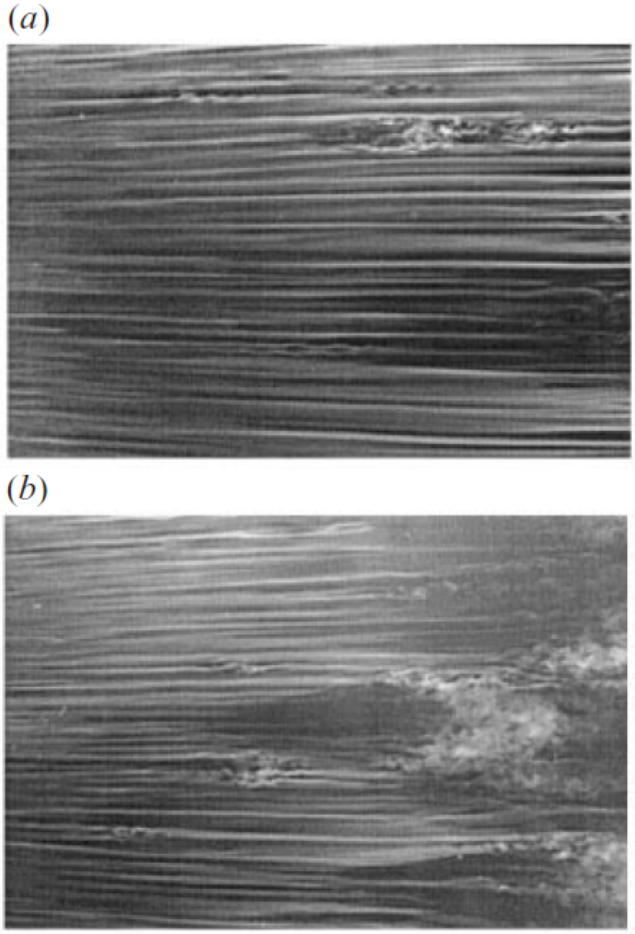

FIGURE 1.5: Bypass transition under the high-level free-stream turbulence visualized by smoke at (a) Tu = 1.5% and (b) Tu = 6.6% in a flat plate boundary-layer (from Matsubara & Alfredsson (2001) [45]).

[41] and Nishioka & Asai (1984, 1989) [25, 42]. In their observation, the near-wall activity in the final stage of transition (K-type transition) were also shown. Later, several authors successfully reproduced these experiments in direct numerical simulations; for instance, see Sandham & Kleiser (1992) [43] and Rist & Fasel (1995) [44].

1.2.2 Bypass transition

As stated in the previous section, the transition initiated by amplification of T-S waves, is only observed when the background turbulence/noise is very small, usually of the order of or less than 0.1% in terms of the rms value of streamwise velocity fluctuations. The scenario of boundary-layer transition caused by higher level of background turbulence is described in this section.

Figure 1.5 displays visualization pictures manifesting the transition process under high disturbance environments (taken by Matsubara & Alfredsson (2001) [45]), in which growth of TS-waves are not observed but many streaky structures appear in the initial stage of the transition. This type of transition is called "bypass transition" which skips the growth stage of T-S waves. With increasing the turbulent intensity in the freestream, streaky structures break down and subsequently turbulent spots are generated at more upstream location and more frequently. The streaky structures or low-speed streaks are originated from penetration of free-stream vortical disturbances into the boundary layer, and the penetrated vortical disturbances (particularly the streamwise vorticity component) cause near-wall low-speed fluids to be lifted up, leading to formation of low-speed streaks. The optimal disturbance with a form of streamwise vortices which causes the largest amplification of streaks was analyzed theoretically and numerically by Andersson, Berggren & Henningson (1998) [46] and Luchini (2000) [47]. The growth mechanism of low-speed streaks can be explained by the transient (algebraic) growth of non-modal disturbances studied by Landahl (1980) [48], Hultgren & Gustavsson (1981) [49] and Butler & Farrell (1992) [50]. Also see Schmid & Henningson (2001) [51] and Fransson *et al.* (2004) [52].

When the low-speed streaks grow and the streak amplitude (of the velocity variation across the low-speed streaks) exceeds a certain value,for instance, by 70% of the freestream velocity (Elofsson, Kawakami & Alfredsson 1999) [53], the streak instability set in, leading to the streak breakdown into a train of quasi-streamwise vortices with alternative sign of vorticity or hairpin-shaped vortices as visualized by Asai, Minagawa & Nishioka (2002) [54]. The streak breakdown was also studied experimentally by Konishi & Asai (2004, 2010) [55, 56], Mans, Kadijk & Lange (2005) [57], Mans, Lange & Steenhoven (2007) [58], Fransson, Matsubara & Alfredsson (2005) [59] and Ho, Asai & Takagi (2017) [60]. Direct nymerical simulations on the streak breakdown were conducted by Brandt & Henningson (2002) [61], Brandt *et al.* (2004) [62], Schlatter *et al.* (2008) [63], Zaki (2013) [64], Hack & Zaki (2014) [65].

1.3 Wall turbulence and drag reduction

In order to reduce the friction drag of aircraft which occupies about 50% of the total drag of civil transport, in addition to application of Laminar Flow Control (LFC) for the wing boundary layer, management/manipulation of wall turbulence structures is also required because most of boundary layers on the main wing and fuselage were governed by turbulent flows. In this section, studies on drag reduction of wall turbulence related to the present thesis are reviewed briefly.

1.3.1 Coherent structures in wall turbulence

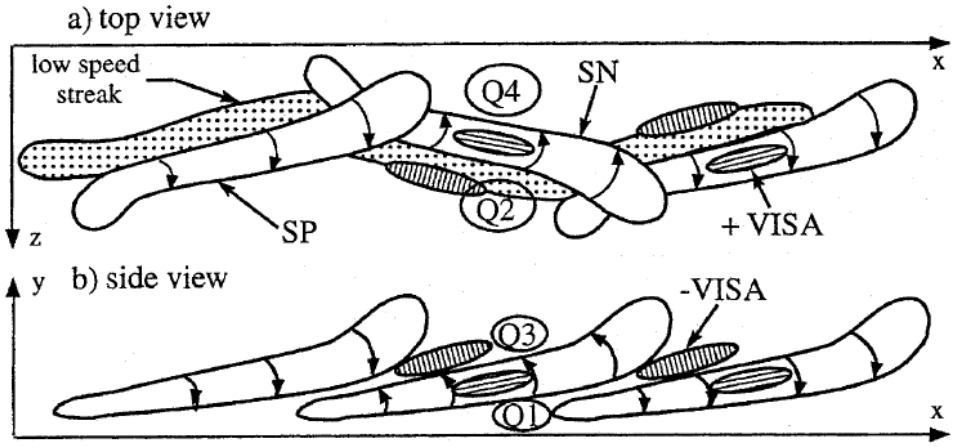

FIGURE 1.6: Schematic view of coherent structures in near-wall turbulence (Schoppa & Hussain (1998) [66] adapted from Jeong *et al.* (1997) [67]).

In turbulent boundary layer, it is known that there exist two kinds of coherent structures, that is, a large-scale motion in the outer region observed by Falco (1977) [68] and Brown & Thomas (1977) [69], and a streaky structure with longitudinal low- and high-speed regions aligned laterally in the region close to the wall observed by Offen & Klein (1974, 1975) [70, 71]. Since their observations, understanding of wall turbulence has been much progressed and improved, especially on the near wall coherent structures. Early development in wall turbulence research mainly focused on the identification of coherent vortices dominating inner and outer regions in wall turbulence, as reviewed by Robinson (1991) [72]. In the near-wall region, one-leg hairpin or

asymmetric hairpin vortices were identified as the important coherent vortices, while larger-scale horseshoe vortices were dominantly identified away from the wall.

As for the dynamics of near-wall turbulence, there has been remarkable progress since 1990s, with the help of development of Computational Fluid Dynamics (CFD) and experimental tools such as the Particle Image Velocimetry (PIV) and visualization techniques. Jeong, Hussain, Schoppa & Kim (1997) [67] analyzed DNS data of near-wall turbulence by using the vortex identification techniques developed by Jeong & Hussain (1995) [73] and showed a train of quasi-streamwise vortices of alternative sign of vorticity as the dominant coherent vortices associated with the low-speed streaks. The coherent near-wall vortices deduced by them are shown in Fig. 1.6, which are now considered to be the most typical near-wall coherent vortices in wall turbulence. Regeneration cycle of the near-wall coherent vortices was proposed and studied by direct numerical simulations (DNS) by several authors: Hamilton (1995) [74], Jiménez & Pinelli (1999) [75], Kawahara & Kida (2001) [76], Itano & Toh (2001) [77], Schoppa & Hussain (2002) [78]. The regeneration cycle consists of generation of low-speed streaks by advection (lift-up) of low speed fluids adjacent to the wall by streamwise vortices, transient growth of streaks during the decaying process of streamwise vortices, and the growth of quasi streamwise vortices due to streak instability. This generation cycle was observed in DNS at the lowest Reynolds number for minimal flow units. As for the growth of quasi streamwise vortices, Schoppa & Hussain (2002) [78] stressed the importance of transient growth mechanism rather than the linear streak instability because the flow was exposed by very high background disturbances in wall turbulence generally.

As for the coherent structures in the outer region, on the other hand, Adrian *et al.* (2000) [79] proposed a packet of hairpin vortices as the dominant large scale coherent vertical structure on the basis of their detailed PIV measurements of wall turbulence.

1.3.2 Drag reduction by riblets

Concerning the reduction of friction drag, both passive and active devices have been proposed and tested thus far. Among the passive devices, one

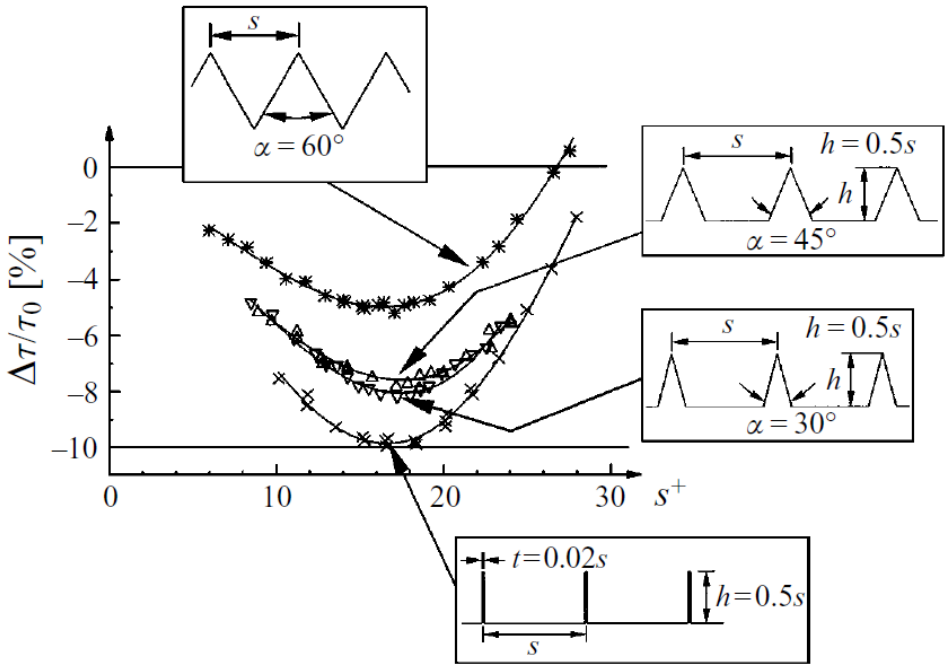

FIGURE 1.7: Drag reduction rates for riblets of various geometries (from Bechert *et al.* (1997) [80]).

of the most successful passive control of wall turbulence, applicable to aerodynamics problems, is surface manipulation of the near-wall structures by tiny streamwise grooves called riblets. The riblets were considered by Walsh (1980) [81] on the basis of grooved surface of shark skin. He tested carefully the drag-reducing ability of riblets and showed a possibility of several-percent drag reduction. Since then, many efforts have been devoted to find the optimal size and geometry of riblets for the largest drag reduction by laboratory experiments and direct numerical simulations: See the papers by Walsh (1983, 1990a, 1990b) [82–84], Choi (1989) [85], Bechert & Bartenwerfer (1989) [86], Bechert *et al.* (1997) [80], Choi *et al.* (1993) [87] and García-Mayoral & Jiménez (2011) [88], Suzuki & Kasagi (1994) [89].

Bechert *et al.* (1997) [80] examined drag-reducing effects of riblets with various cross-section-geometries including triangular, scalloped, trapezoidal and blade riblets and compared the drag-reduction rates, as illustrated in Fig. 1.7. The figure shows that the optimal height-to-spacing ratio (h/s) was 0.5 for most geometries and the largest drag reduction rate was obtained with the riblet spacing over the range of 15 to 20 in wall units for all cases. Among all the cross-section geometries, blade-shape riblets had the largest

drag-reduction rate of 10%. However, the blade riblets are not practical because of structural problem. Practically, riblets having a trapezoidal cross-section with ridge angle of 30° and the height-to-spacing ratio of 0.5 are recommended and they can reduce the friction drag by 8% at most.

1.4 Contents and organization of the thesis

In this thesis, three experimental studies were described. First two experiments deal with flows over riblets. Riblets having a capability of drag reduction of wall turbulence are applied to the laminar and transitional regimes in order to clarify the influences of riblets on the linear instability of laminar flow and on the lateral turbulent contamination related to the development of turbulent spot or wedge. In third experiment, in order to further improve our knowledge on the mechanism of transition and turbulence, influences of disturbance nature on the instability and breakdown of low-speed streak, which are the key mechanisms/events for generation and sustenance of the wall-turbulence. This thesis thus is organized as follows:

Chapter 1: Introduction. This chapter describes briefly the background and objective of the present study, the related work on the boundary-layer instability and transition, and recent studies on wall turbulence and drag reduction by riblets.

Chapter 2: Stability of laminar flow in a channel with riblets. This chapter describes details of the experiment on the influences of streamwise and oblique riblets on the flow instability was described as the main contents, focusing on dependence of the flow instability on the oblique angle of the riblet-alignment. In this chapter, the quality of the low-turbulence channel flow apparatus and the riblet model used in the experiment are also explained.

Chapter 3: Effects of streamwise riblets on lateral turbulent contamination in a boundary-layer. This chapter explains details of the experiment on effects of streamwise riblets on lateral turbulent contamination. The experiment was conducted in a high-quality wind tunnel.

Chapter 4: Dependence of streak breakdown on disturbance nature. This chapter discusses the mechanism of wall turbulence through the experiment

on instability and breakdown of a low-speed streak initially forced by signals of turbulent fluctuations deduced from developed wall turbulence. Particular focus is on the dependence of streak instability on the spanwise coherencies.

Chapter 5: This chapter summarizes all important findings in the thesis.

Chapter 2

Stability of laminar flow in a channel with riblets

2.1 Introduction

Surface manipulation with riblets is one of the most successful passive devices for reducing friction drag in wall turbulence, as has been confirmed experimentally and numerically by many authors since the pioneering work by Walsh [81, 82]. See the papers by Walsh [83, 84], Choi [85], Bechert [80, 86], Choi *et al.*[87] and García-Mayoral & Jiménez [88]. Various cross-sectional geometries of riblets such as sawtooth, scalloped, blade and trapezoidal riblets have been proposed and tested thus far, and the optimal size of the riblet cross section was found for each riblet-geometry, as summarized by Bechert [86]. The optimal riblet spacing (distance between neighboring ridges) was found to lie between 10 and 20 in wall units, with the maximum drag-reduction rate of 6% – 10%. It is also worth noting that according to re-evaluation of experimental data for various cross-section geometries by García-Mayoral & Jiménez [88, 90], the optimal riblet size is well scaled with the square root of the groove cross-sectional area in wall units (A_g^+), that is, the maximum drag reduction is obtained with $(A_g^+)^{1/2} \approx 11$ for all the riblet geometries. The drag reduction rate is linearly proportional to the riblet size for very small riblets (with the ridge spacing less than 10 in wall units, for instance) and its mechanism has been explained by analyzing the friction drag of laminar viscous flow over riblets [86, 91]. When the riblet size increases, the flow adjacent to riblets can interact with near-wall turbulent (streamwise) vortices, which can also control the drag-reducing mechanism of riblets. The past experimental observations [85, 89] and direct numerical simulations [87]

showed that riblets with the optimal spacing or larger could weaken the lateral motion of near-wall vortices and/or interrupt their development, causing the Reynolds stress and turbulent fluctuations to decrease.

In engineering applications of riblets, such as in aircraft, including on wing surfaces, our interest also includes the effects of riblets on the flow instability and transition. The present work focuses on the effects of riblets (longitudinal grooves of viscous scale) on the instability of wall-bounded shear flows. Regarding the effects of longitudinal grooves or riblets on flow instability, Luchini & Trombetta [92] analyzed the instability of a 2-D boundary-layer modified with riblets and showed that riblets could enhance the growth of T-S waves. Ehrenstein [93] computed linear instability characteristics of flow in a channel with the lower wall mounted with riblets of semi-circular scalloped cross-section whose spacing of 50% and 30% of the channel half-depth h, and showed that the critical Reynolds number was reduced significantly, *e.g.*, to about 4500 for grooves with spacing of $0.5h$ and height of $0.09h$. Recently, Moradi & Floryan [94] analyzed the linear stability of flow in a channel with streamwise grooves over a wide range of wavenumbers from 0.1 to 10 using their accurate stability code, and showed that the presence of grooves could destabilize the flow when the groove wavenumber was larger than 4.22, whereas grooves with wavenumbers smaller than this critical value (~ 4.22) had a stabilizing effect, being not strongly dependent on the cross-sectional geometry of grooves. It was also shown that the destabilizing effect of streamwise grooves appeared even when the height of grooves was sufficiently small. Experimentally, Grek, Kozlov & Titarenko [95] examined influences of triangular riblets with lateral spacing of the order of the displacement thickness on development of T-S waves and subsequent three-dimensional development in a laminar boundary layer, and showed that the streamwise riblets promoted growth of T-S waves more intensively than the transverse grooves with the same cross-section geometry.

Our interest here is on the destabilized effects of small riblets with much larger wavenumbers than the critical value (~ 4.22) mentioned above, by which the flow is only modified in the vicinity of ribbed surface. The effects of such small-sized riblets would be important in considering a case in which optimally-sized riblets (with ridge spacing of 10 – 15 in wall units) leading to largest turbulent drag reduction are applied to flow regimes not only in the turbulent stage but also in upstream laminar and transitional regimes. In the present study, in order to show experimentally how small-sized riblets

could modify the stability characteristics of laminar flow, a stability experiment was conducted in a channel generating a plane Poiseuille flow, using small-sized riblets with triangular ridges and trapezoidal valleys which were typical for turbulent drag reduction in actual flows. The experiment also included investigations of the effects of the angle between the riblet alignment and flow direction on flow instability. When the direction of riblet alignment is inclined to the streamwise direction beyond a certain inclination angle, the near wall flow can separate at the riblet-ridges so that the instability characteristics could change significantly. Therefore, it is interesting how the nature of the instability is dependent on the oblique (inclination) angle of the riblets. These are motivations of the present study.

In developed wall turbulence, on the other hand, García-Mayoral & Jiménez [88, 90] pointed out on the basis of their stability analysis that flow near the grooved surface could be locally unstable due to inflectional velocity profiles appearing close to the grooved surface as the groove size increases above a certain critical value (about 7–8 in terms of $(A_g^+)^{1/2}$), and demonstrated in direct numerical simulations that a two-dimensional Kelvin-Helmholtz-like instability close to the grooves/riblets caused spanwise (two-dimensional) vortices (with typical streamwise wavelengths $\sim$ 150 in wall units) to develop, weakening the drag-reducing effect of grooves/riblets (that is called the viscous breakdown) by producing an additional Reynolds stress. In our experiment, the riblet (groove) height and ridge-spacing were selected to be about 5.5% and 11% of the channel half-depth. The riblet size (the spacing s) was the viscous-layer scale and included the critical riblet (groove) size mentioned above in terms of $(A_g^+)^{1/2}$ for the Reynolds numbers over 4000 to 6000. Thus, we may expect that experiments on the instability of laminar flow over such small riblets are helpful in elucidating the viscous breakdown of drag reducing effect of riblets in wall turbulence, too. This is the other motivation of the present study.

In the following, Section 2.2 describes the experimental setup and the riblet model used in the experiment. Section 2.3 provides the channel flow quality and the comparisons of the instability characteristics in the smooth-wall channel between the experiment and the linear stability theory to confirm good accuracy of the stability experiment. Sections 2.4 and 2.5 examines influences of streamwise and oblique riblets on the flow instability, respectively. Close comparisons on the stability characteristics of channel flows with and without riblets are made. Section 2.6 summarizes the main results

of the experiment.

2.2 Experimental setup and procedure

The experiment was conducted in a rectangular channel, whose width, height and length were 400 mm, 15 mm and 6000 mm, respectively. The aspect ratio of the channel cross section (the ratio of width to depth) was 26.7. A schematic diagram of the wind channel facility is illustrated in Fig. 2.1. The flow was provided by a sirocco fan. After the diffuser section, four 40-mesh damping screens and a honeycomb were installed in the settling chamber of $400 \times 400mm^2$, and the flow was led to the channel through a smooth two-dimensional contraction. As shown later, the flow developed sufficiently to a plane Poiseuille flow in the test section 5000 mm downstream from the channel inlet and remained laminar even at supercritical Reynolds numbers at least up to 6500: The Reynolds number Re was defined as $U_c h/\nu$ where U_c was the center-line velocity, h the channel half depth and ν the kinematic viscosity. Note that even though disturbance growth occurred in the unstable frequency range beyond the critical Reynolds number for the linear instability, $Re_{cr} = 5772$, it would not cause a transition to turbulence under low background turbulence because of the finite length of the channel. The schematic of the channel test section is illustrated in Fig. 2.2. The channel facility was the same as that used in the recent experiment [96]. The upper and lower walls of the channel were built with 5-mm-thick glass plates. The surfaces of the glass walls were sufficiently flat and smooth to conduct the stability experiment with good accuracy. Here, a slight waviness of the channel walls (especially long-wavelength waviness), if it existed, could affect the stability characteristics. Therefore, the flatness of the glass-walls was confirmed by comparing the stability characteristics to the theoretical ones calculated from the Orr-Sommerfeld equation; that will be shown in the next section. As for the coordinate system, x was the streamwise distance, y the normal-to-wall distance, and z the spanwise distance.

A vibrating ribbon system was employed to excite two-dimensional (2-D) traveling waves. A phosphor bronze ribbon that was 5 mm wide and 0.05 mm thick was stretched in the spanwise direction, 1.2 mm away from the lower wall ($y/h = -0.84$) at a location 5000 mm ($\approx 650h$) downstream from the channel inlet (or about 1 m upstream from the channel exit). Twelve

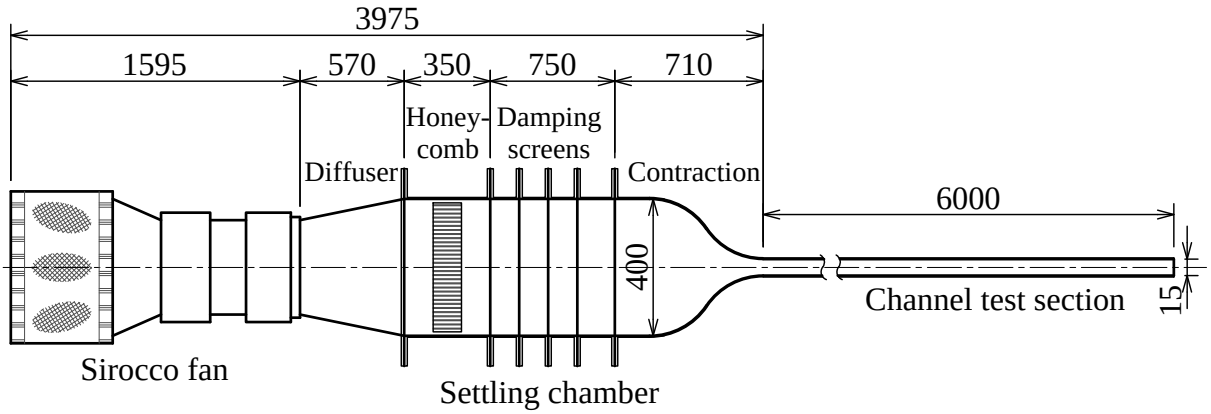

FIGURE 2.1: Low-turbulence wind channel (dimensions in mm, not in scale).

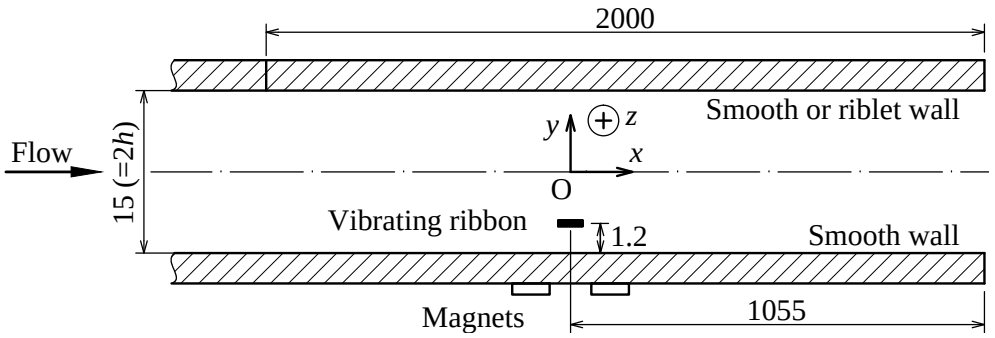

FIGURE 2.2: Schematic of test section (dimensions in mm, not in scale).

pieces of permanent magnet made of neodymium were glued on the back side of the lower glass wall to generate an electro-magnetic force perpendicular to both the ribbon and the normal-to-wall direction when electric current was applied to the ribbon. The vibrating ribbon was driven at a single frequency using a sine-wave generator through a power amplifier. The amplitude of the excited disturbance was well controlled by changing the input current to the ribbon.

The geometry of the riblets used here is illustrated in Fig. 2.3(a). The riblets had triangular ridges with ridge angle of 30° and trapezoidal valleys. The ridge-spacing (s) was 0.83 mm and the height-to-spacing ratio (k/s) was 0.5. Note that the edge thickness of the triangular ridge was 0.005 mm. Riblets were created by coating paint on a thin flexible plastic panel (0.3 mm thick), and the riblet-sheet was glued to the upper channel wall over the range of 2000 mm in the downstream test section, while the lower wall was

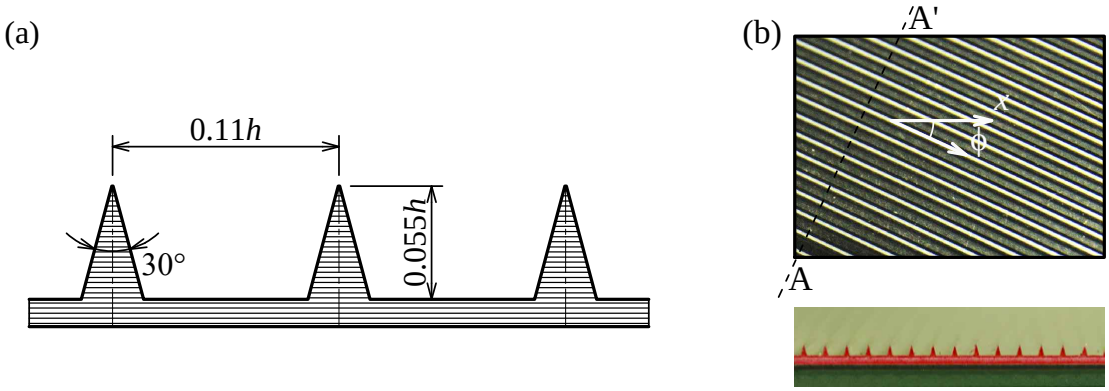

FIGURE 2.3: Riblet model. (a) Geometry, (b) photograph (upper; top view, lower; cross-section (AA') view).

flat and smooth. The ribbed wall was connected to the upstream flat wall in such a way that the tips of riblet-ridges were placed at almost the same height as the upstream smooth surface. According to a theoretical analysis of the shear flow over streamwise grooves by Luchini *et al.* [91], the virtual wall position where the velocity distribution approaches zero is lower than the tips of riblets by about 20% of the riblet spacing for the streamwise riblets of the present geometry. Therefore, the center-line velocity (U_c) could be slightly decreased compared to the upstream flat-wall region for the fixed mass flow rate, but the difference in U_c between the flat and ribbed regions would be less than 1% for the present riblet size.

In addition to the experiment with streamwise riblets, investigations were conducted with oblique riblets whose ridge-alignment was inclined to the streamwise direction as illustrated in Fig. 2.3(b) in order to examine how much the nature of the instability is sensitive to the angle ϕ between the directions of the riblets and the main flow. In all of the experiments, riblet sheets with the same size and geometry were used.

The streamwise velocity component, whose time-mean and fluctuation components were denoted by U and u, respectively, was measured using a constant temperature hot-wire anemometer. The length of the hot-wire sensor, a tungsten wire of 5 μm in diameter, was 1 mm, which could sense a streamwise velocity component averaged almost over one riblet spacing ($\sim$ 0.83 mm) in the spanwise direction. Calibration of the hot-wire was made using a calibration function $U = (AE^2 - B)^{1/0.45}$, where E is the output voltage of the hot-wire at velocity U, and A and B are the calibration constants. The hot-wire probe was inserted from the downstream end of the channel and

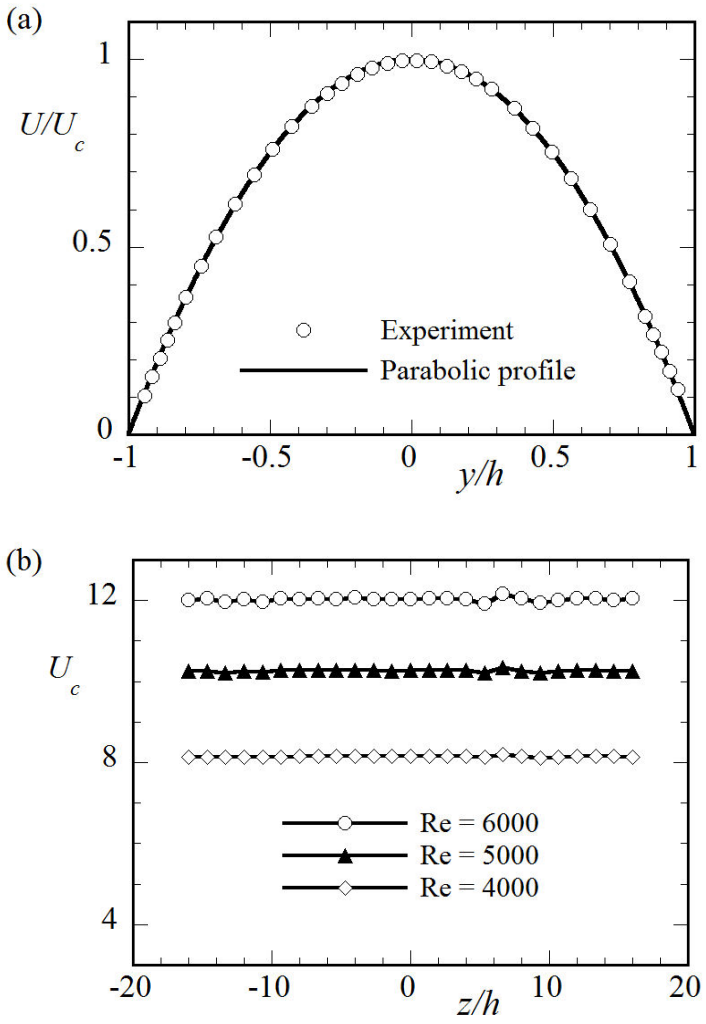

FIGURE 2.4: Velocity profile. (a) y-distribution of U, (b) z-distribution of U at the center line.

could be traversed in all directions. Hot-wire data were stored in a PC after 16-bit analogue-to-digital conversion with a sampling frequency of 10 kHz, together with the current input to the vibrating ribbon used as the reference signal for the phase measurement of the excited T-S waves.

2.3 Base flow and stability characteristics

Before investigating the effect of riblets on the flow instability, we should confirm that the stability characteristics of the flow in a channel with a smooth surface agree well with the prediction of the linear stability theory. First let

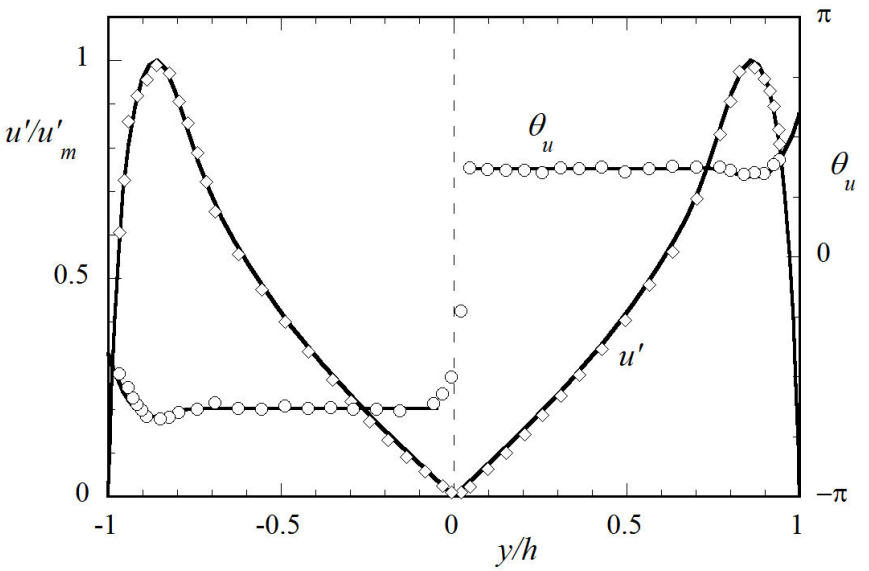

FIGURE 2.5: Comparison of the amplitude (◇) and phase distributions (○) of T-S wave (ω = 0.27) between the experiment and the linear stability theory (——) at Re = 6000.

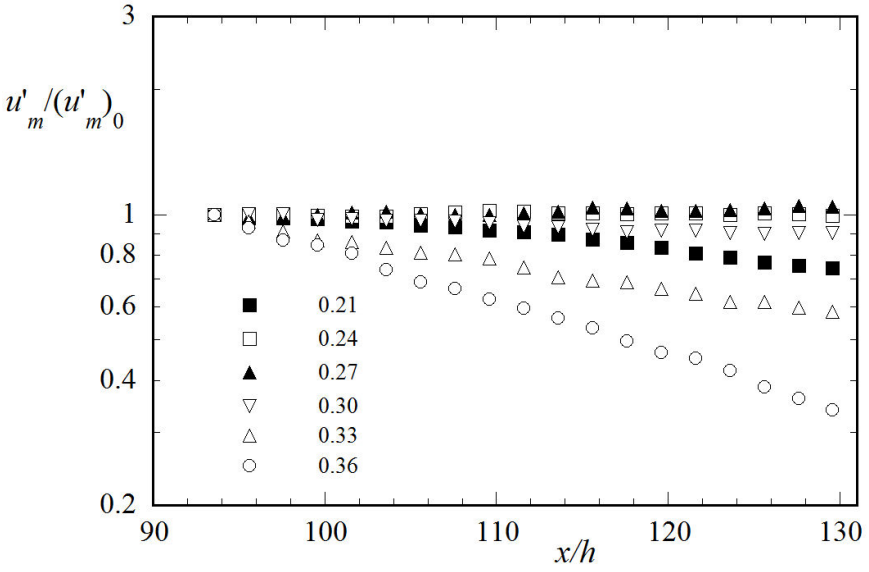

FIGURE 2.6: Development of T-S waves excited with ω = 0.21, 0.24, 0.27, 0.30, 0.33 and 0.36 at Re = 6000.

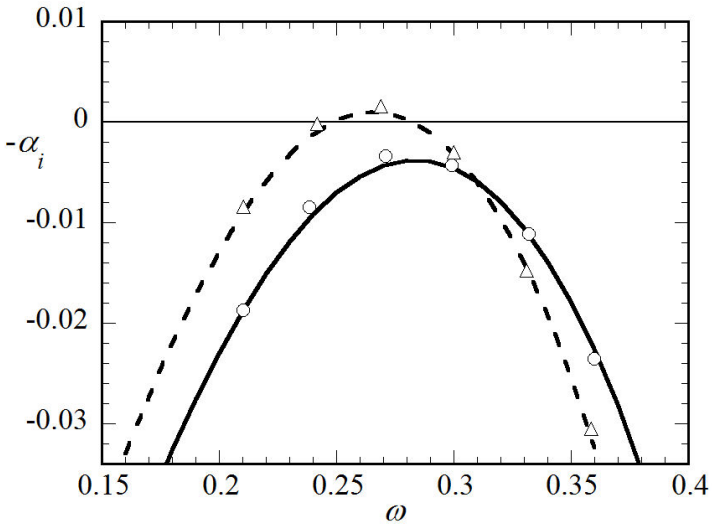

FIGURE 2.7: Comparisons of growth rates between the experiment and the linear stability theory at Re = 5000 (○) and Re = 6000 (△) in smooth-wall case.

us explain the quality of the channel flow. Needless to say, the stability characteristics are very sensitive to the channel flow quality. To realize a fully developed plane Poiseuille flow experimentally, a long channel without surface imperfections is required. Furthermore, stability experiments require not only sufficiently weak residual turbulence but also channel walls with sufficient flatness; slight surface waviness (*i.e.*, small-amplitude waviness), if it existed, could affect the growth of T-S waves in a channel flow.

As analyzed theoretically by Sadri & Floryan [97] and verified experimentally by Asai & Floryan [98], the deviation of the velocity profile $U(y)$ from the parabolic flow profile $U_0(y)$, ΔU ($= U - U_0$) decays exponentially with streamwise distance, as $\Delta U \propto exp[-28.22(X/h)/Re]$ where X was measured from the channel inlet. In the present channel of $800h$ in length, ΔU was reduced to about 1% of the center velocity U_c at the test section (beyond $700h$ downstream from the inlet of the channel) at Re = 6000, the highest Reynolds number in the present experiment. Fig. 2.4(a) compares the velocity profiles at Re = 6000 to the parabolic profile. The measurement was done at a location $780h$ downstream from the inlet of the channel. The agreement was quite good. Spanwise variations in the center-line velocity U_c at Re = 4000, 5000 and 6000 are displayed in Fig. 2.4(b), showing that the flow is two-dimensional except $5 < z/h < 10$ where the spanwise variation was at most 2% in terms of the peak-to-peak value at Re = 6000. In the region of

$-8 < z/h < 4$, the magnitude of the variation (peak-to-peak value) was less than 0.2% and 0.4% at Re = 5000 and 6000, respectively.

The quality of the channel flow was further verified by conducting experiments on the linear stability. Fig. 2.5 illustrates the y-distributions of the amplitude u' (r.m.s. value of streamwise velocity fluctuation) and phase θ_u of the T-S wave excited by the vibrating ribbon at $Re = 6000$ by comparing it to the normal mode of the Orr-Sommerfeld equation of the linear stability theory, where the amplitude was normalized with its maximum u'_m. Here the vibrating ribbon was forced at a non-dimensional angular frequency ω ($= 2\pi fh/U_c$) = 0.27 where f was the forcing frequency, and the distributions were measured at x/h = 120 where x was measured from the center of the vibrating ribbon as illustrated in Fig. 2.2. The agreement between the experiment and the linear stability theory was quite good. Fig. 2.6 displays the development of T-S waves excited with ω = 0.21, 0.24, 0.27, 0.30, 0.33 and 0.36 at a supercritical Reynolds number Re = 6000 in terms of the amplitude ratio $u'_m/(u'_m)_0$ where u'_m was the maximum of u' at each x-location and $(u'_m)_0$ was u'_m at x/h = 90. The disturbances excited exhibited exponential growth or decay of T-S waves with an almost constant exponent for all the frequencies and thus their spatial growth rates ($-\alpha_i$) could be obtained with good accuracy. Here, it is noted that in all cases, the amplitudes of T-S waves did not exceed 0.5% in terms of u'_m/U_c, that is, the T-S amplitude was kept less than the threshold value for the secondary instability ($u'_m/U_c \simeq 0.7\%$) [6, 42]. Indeed, the wave development sufficiently maintained two-dimensionality. Fig. 2.7 compares the growth rates ($-\alpha_i$) scaled with h to those predicted by the linear stability theory at Re = 5000 and 6000. We see that the agreement between the experiment and the linear stability theory was quite good. We also confirmed that the phase θ_u at a fixed y varied linearly with x completely and the wavenumber of T-S wave (scaled with h) α_r which was given by the x-derivative of θ_u was in good agreement with that by the linear stability theory: The comparison between the theory and experiment will be shown later. These results enabled us to examine the effect of riblets on the instability characteristics with good accuracy.

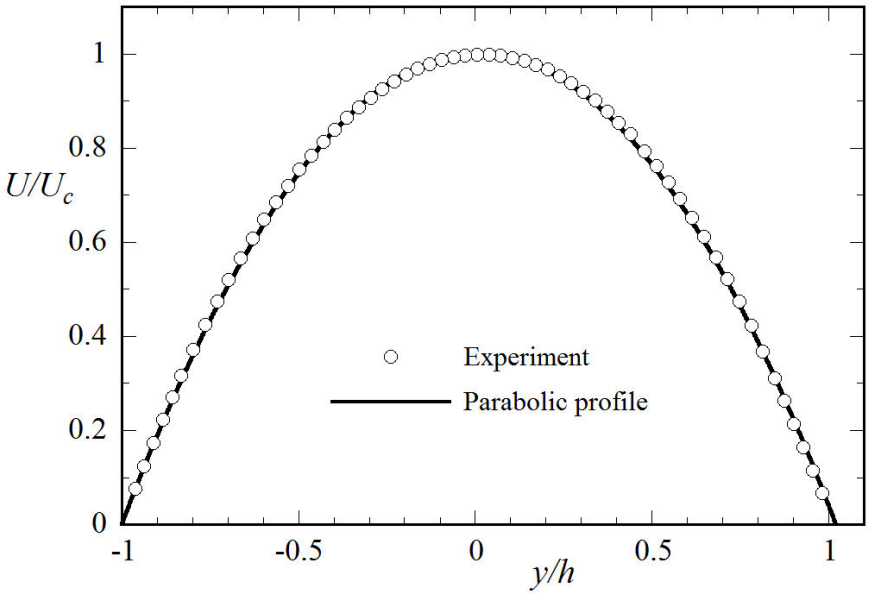

FIGURE 2.8: The y-distribution of U at Re = 6000 in the channel with streamwise riblets.

2.4 Influences of streamwise riblets on the flow instability

In the experiment with riblets, the channel depth $2h$ was defined as the distance between the flat surface of the lower wall and the top of the riblet-ridges on the upper wall. Therefore, the height (k) and spacing (s) of the riblet-ridges were $0.055h$ and $0.11h$, respectively, and the non-dimensional wavenumber of the ridge-spacing $2\pi h/s$ was 57. Here, these riblet sizes were chosen such that they would correspond to those of the drag-reducing riblets ($s^+ \sim 20$, $k^+ \sim 10$) if the flow underwent transition to turbulent with the same volumetric flow rate as that of the laminar parabolic flow at Re = 5000; as for the relationship between the laminar and turbulent channel flows, see the paper [99]. In the laminar flow condition, the riblet height k^+, that was given by $(k/h)(2U_c h/\nu)^{1/2}$ for the parabolic flow, was only 5.5 at Re = 5000. This was comparable with the often-cited critical roughness height (k^+ = 5) for the hydraulic smoothness. It is also worth noting that the square root of the groove cross-sectional area $(A_g^+)^{1/2}$ that is the other length scale of riblets introduced by García-Mayoral & Jiménez [88], was about 7.8 at Re = 5000.

Here, according to the theoretical work by Luchini *et al.* [91], the so-called

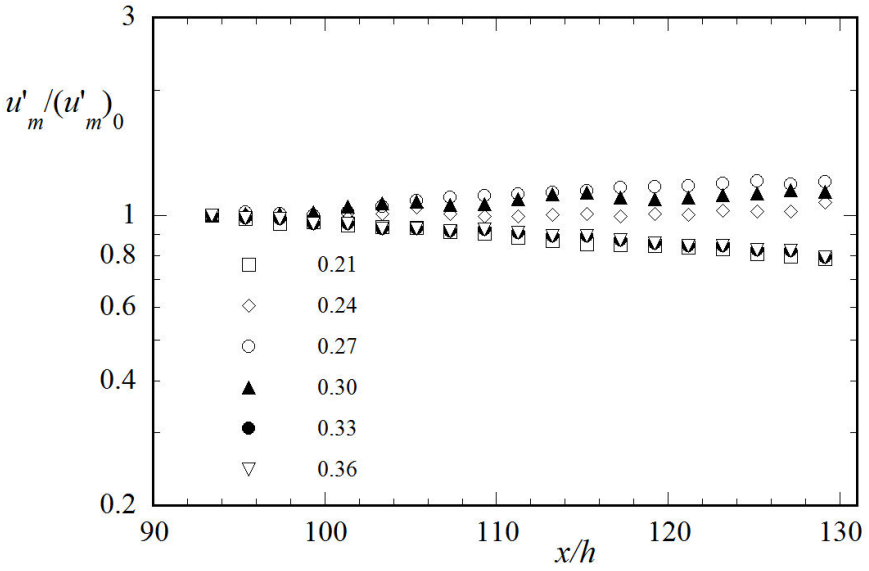

FIGURE 2.9: Development of T-S waves excited with ω = 0.21, 0.24, 0.27, 0.30, 0.33 and 0.36 at Re = 5000 in the channel with streamwise riblets.

protrusion height [86] which is an offset between the virtual wall position and the riblet tip would be about 20% of the riblet spacing for the present riblet geometry. In order to confirm this, we carefully examined the velocity distributions over the riblets. Fig. 2.8 compares the velocity distributions in the upper channel half to the parabolic profile: Note that the hot-wire sensor (1 mm long) measures the velocity averaged almost over one riblet spacing ($\sim$ 0.83 mm). The parabolic profile was plotted over $-1 \leq y/h \leq 1.02$, that is, the virtual wall position on the ribbed surface was taken to be $1.02h$, inside the grooves. Note that the bottom of grooves (the valley of riblets) was located at y/h = 1.055. The comparison shows that the velocity distribution coincided with the parabolic profile very well, and thus the distance between the riblet tip and the virtual wall position, about 40% of the riblet height ($0.055h$), was in good agreement with the protrusion height given by Luchini *et al.* [91].

Then, we examined effects of streamwise riblets on the flow instability. Fig. 2.9 displays the streamwise development of T-S waves excited with ω = 0.21, 0.24, 0.27, 0.30, 0.33 and 0.36 at Re = 5000 in terms of the amplitude ratio $u'_m/(u'_m)_0$ where $(u'_m)_0$ was u'_m at x/h = 90. Here, the measurement of u'_m was conducted in the lower half of the channel ($-1 < y/h < 0$), *i.e.*, in the smooth-wall side, and the amplitude $(u'_m)_0$ was kept not to exceed

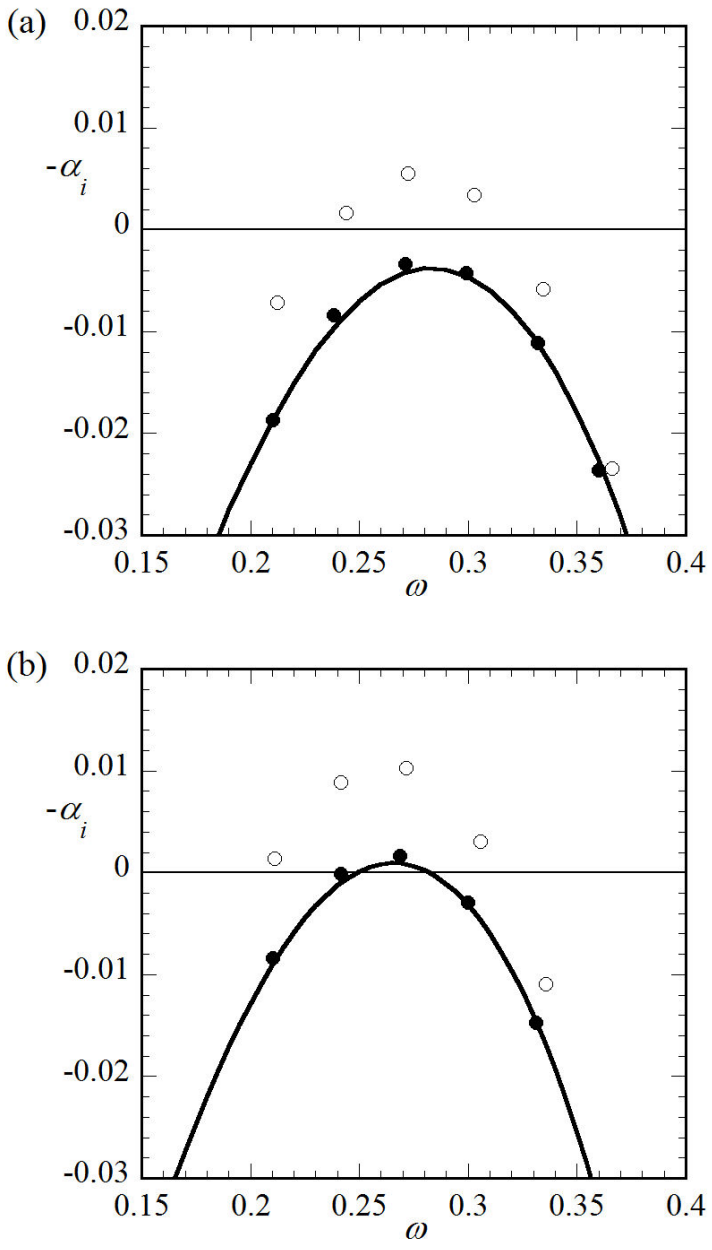

FIGURE 2.10: Comparisons of growth rates between riblet and smooth walls. (a) Re = 5000, (b) Re = 6000. (○) riblet-wall, (●) smooth-wall. Solid curve represents the linear stability theory for the smooth-wall case.

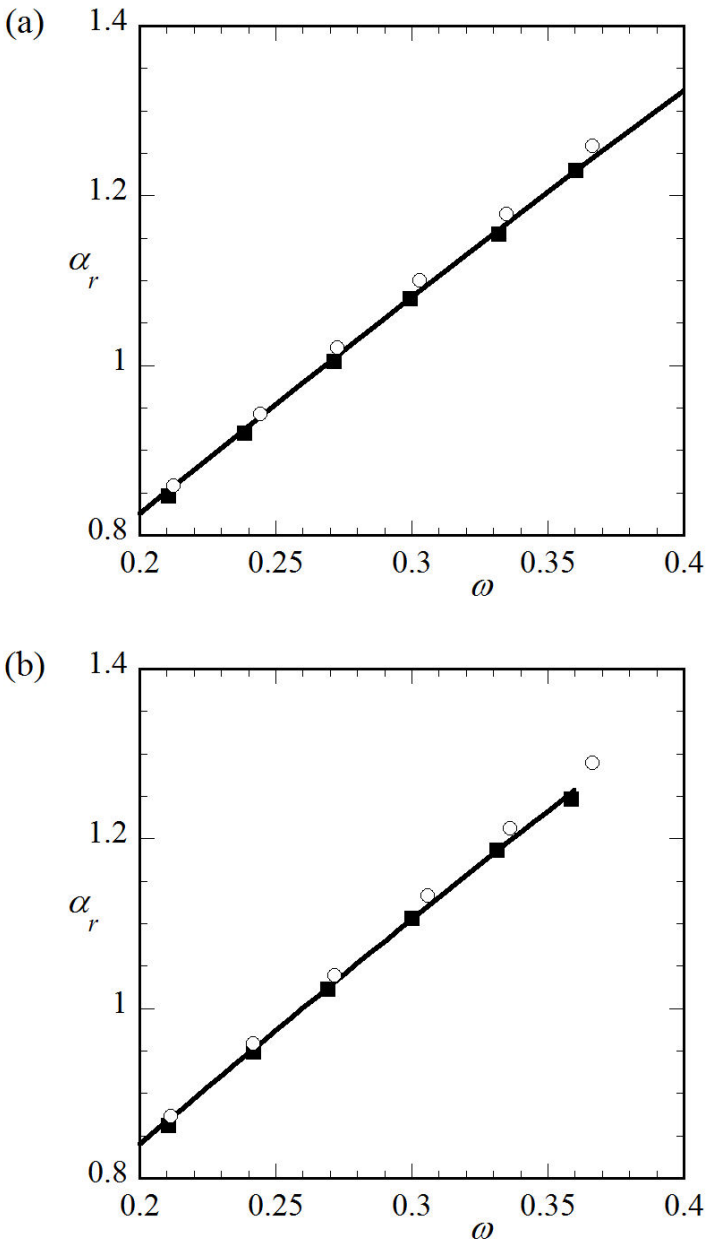

FIGURE 2.11: Comparisons of wavenumbers between riblet and smooth walls. (a) Re = 5000, (b) Re = 6000. (○) riblet-wall, (■) smooth-wall. Solid curve represents the linear stability theory for the smooth-wall case.

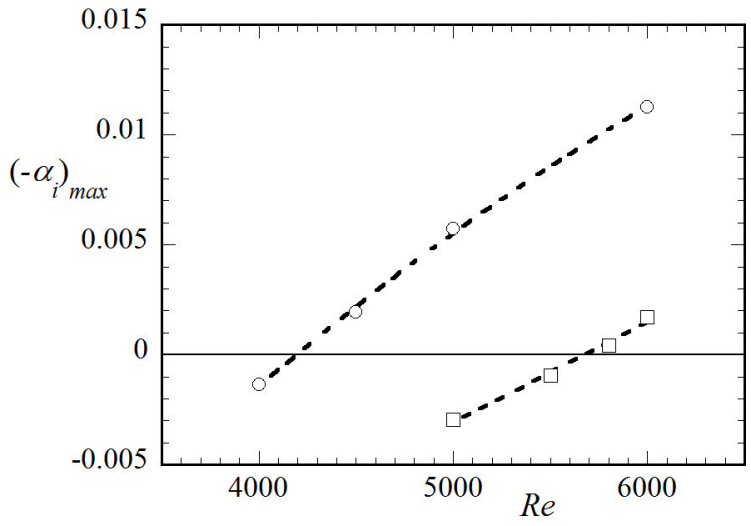

FIGURE 2.12: Growth rate of the most unstable T-S mode $(-\alpha_i)_{max}$ versus Re in the channel with riblet-wall (○) and smooth-wall (□).

0.3% of U_c for all the cases. We see that the T-S waves with ω = 0.27 and 0.30 grow slowly in the streamwise direction. Thus, the riblets destabilized the otherwise subcritical Poiseuille flow even with the viscous-layer scale of $k^+ \sim 5.5$. In order to show the destabilizing effect of riblets more quantitatively, Figs. 2.10(a) and (b) compare the spatial growth rates of T-S waves $(-\alpha_i)$ in the riblet-wall channel to those for the smooth wall case at Re = 5000 and 6000, respectively. The comparisons showed clearly that the unstable frequency range appeared over ω = 0.24 – 0.31 even at Re = 5000 in the channel with the riblets. We also see that the riblets caused the most unstable frequency to shift towards the lower frequency only slightly at both the Reynolds numbers. Similarly, Figs. 2.11(a) and (b) compare the wavenumbers of T-S waves (α_r) in the riblet-wall channel to those for the smooth wall case at Re = 5000 and 6000, respectively. The wavenumber was only slightly larger than that in the smooth-wall case for all the frequencies.

The development of T-S waves was further examined at lower Reynolds numbers and the growth rate of the most amplified T-S mode at each Reynolds number, denoted by $(-\alpha_i)_{max}$, is plotted against the Reynolds number in Fig. 2.12. Interpolating the experimental data, we found the critical Reynolds number Re_{cr} to be about 4200, which was about 73% of the value for the smooth-wall channel (Re_{cr} = 5772). Here, we refer to the stability analysis by Moradi & Floryan [94], in which a sinusoidal surface variation represented

by $y_w = 1 + A_w \cos(\beta z)$ was considered as a simple groove model and the analysis was conducted over β = 0.1–10, with various values of A_w. Their result showed that the grooves could enhance the flow instability for $\beta >$ 4.22 and reduced Re_{cr} to 5500 for β = 10 (the largest groove wavenumber examined in their analysis) and $2A_w$ = 0.06h (almost the same groove height as the present). Thus, we elucidate that the destabilizing effect of the present large-wavenumber-riblets with ($\beta = 2\pi h/s$ = 57) is much stronger than the grooves with β = 10. Note that according to their computation [94], the velocity profiles on the grooves were quite different between β = 10 and 50, though the stability analysis was not conducted with β = 50.

As shown above, the velocity profile was little affected by the presence of the small-scale riblets except inside the riblets. Therefore, the destabilizing effect of the riblets is attributed to the existence of an inflection point in the mean velocity inside the riblets, although it was difficult to measure the flow field inside the small riblets experimentally. Then, we examined how the structure of the instability wave (T-S wave) was changed by the riblets. Figs. 2.13(a) and (b) display the y-distributions of the amplitude u'/u'_{mL} and phase θ_u of the streamwise velocity fluctuation (excited with ω = 0.27) respectively at $Re = 6000$, where u'_{mL} is the maximum amplitude in the lower channel half ($y < 0$). We can see that the peak amplitude on the ribbed surface was by about 15% larger than that on the lower smooth surface. Besides, the y-position of the amplitude peak shifted towards the ribbed surface by about 0.04h, without changing the shape of the phase distribution. Therefore, assuming that the Stokes layer thickness of T-S wave ($\sim (\nu/\omega)^{1/2}$) was unchanged by the presence of riblets, the disturbance velocity no doubt existed insides the riblets with sufficient intensity. Note that the amplitude distribution on the ribbed surface could be extrapolated to y/h = 1.04, across the virtual wall position for the mean velocity profile (y/h = 1.02). Considering the amplitude and phase distributions were not largely different from those of the T-S wave in the smooth-wall channel, the disturbance growth observed was essentially governed by the viscous instability mechanism in which the energy production due to the Reynolds stress occurs mainly in the Stokes layer. Even though the near-wall disturbance was strongly influenced by viscosity, the shear layer of the mean flow insides the riblets would be slightly free from the bottom of riblets, which could cause the flow to be more unstable than in the smooth-wall case. This was consistent with the fact that the disturbance appeared inside the grooves across the virtual wall

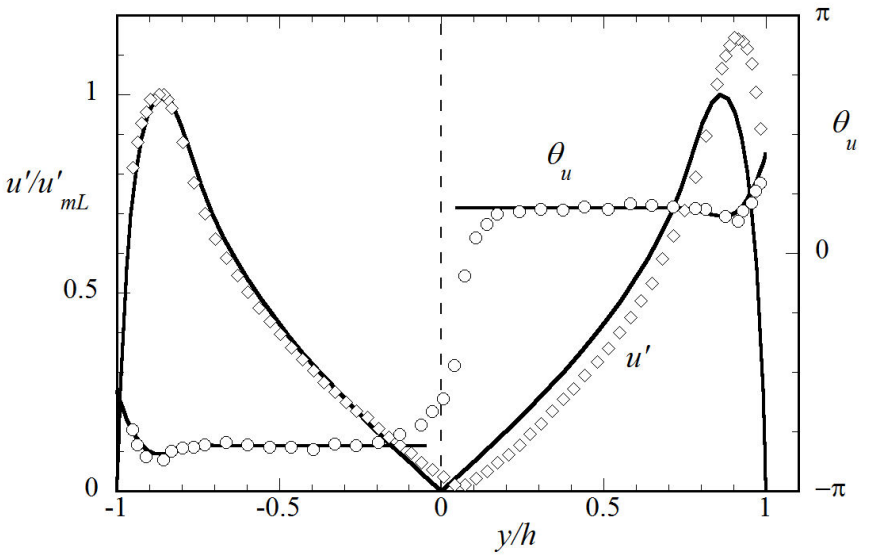

FIGURE 2.13: The amplitude (◇) and phase (○) distributions of T-S wave ($\omega = 0.27$) at $Re = 6000$ in the channel with streamwise riblets. Solid curves represent the linear stability theory in the smooth-wall case.

position of the velocity profile.

In addition, we compared the value of the square root of the groove cross-sectional area in wall units, $(A_g^+)^{1/2}$ at the critical Reynolds number to a stability analysis for a model flow with a piecewise-linear velocity profile over the grooved wall by García-Mayoral & Jiménez [88] which was conducted to elucidate a mechanism of viscous breakdown for the drag reducing effect of riblets in wall turbulence. Their result showed that the critical value of $(A_g^+)^{1/2}$ for the onset of the instability was 7–8. In the present stability experiment, on the other hand, the value of $(A_g^+)^{1/2}$ was about 7.2 at the critical Reynolds number $Re_{cr} = 4200$. Thus the critical values of $(A_g^+)^{1/2}$ were close together in both the cases in spite of the difference in the base flow profile.

2.5 Dependence of the flow instability on the oblique angle of the riblet-alignment

Next, to see the dependence of the flow instability on the oblique angle (ϕ) of the riblet-ridge alignment, we glued a riblet-sheet of the same geometry and size by inclining it to the streamwise direction at angles of 20°, 30° and

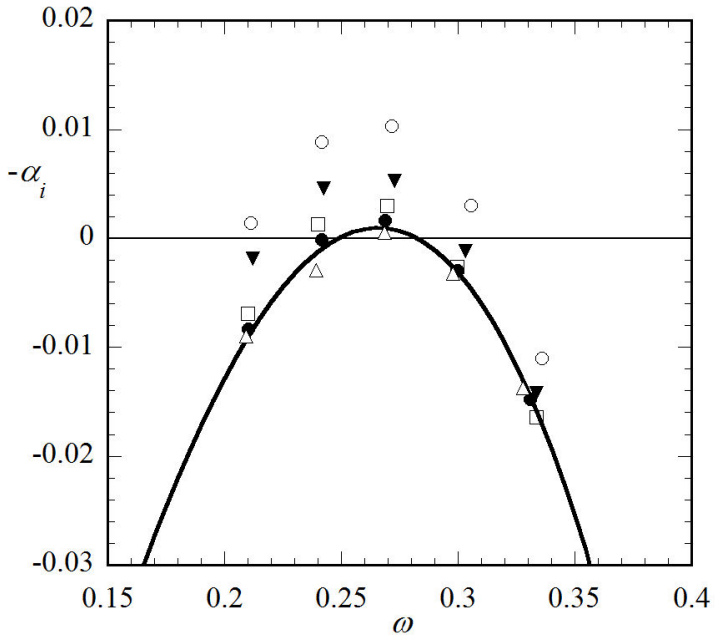

FIGURE 2.14: Comparisons of growth rates for oblique riblets [$\phi = 20°$ (▼), 30° (□) and 45° (△)] to the streamwise-riblet case (○) and the smooth-wall case (●) at Re = 6000. Solid curve represents the linear stability theory for the smooth-wall case.

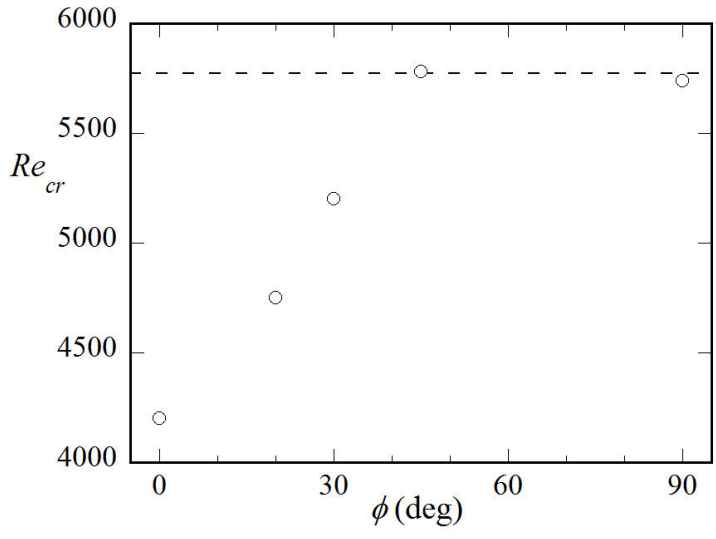

FIGURE 2.15: The critical Reynolds number (Re_{cr}) versus the oblique angle of riblet alignment (ϕ). Dotted line denotes the critical Reynolds number of plane Poiseuille flow (Re_{cr} = 5772).

45°, and similarly examined streamwise development of T-S wave. Fig. 2.14 plots the growth rates ($-\alpha_i$) against ω at Re = 6000 by comparing them to the growth rates for the cases of the streamwise alignment ($\phi = 0°$) and the smooth wall (without riblets). The comparison clearly shows that the destabilizing effect of the riblets was weakened rapidly as the oblique angle of the riblets increased. Interestingly, the growth rates of T-S waves closely approached those of the smooth wall case at $\phi = 30°$, and became almost the same as those in the smooth wall case when the riblets were inclined with ϕ = 45°. The similar result was obtained at Re = 5000. In order to show the dependence of the destabilizing effect on the oblique angle of the riblets more definitely, we examined the critical Reynolds numbers for each inclination of the riblets. Fig. 2.15 plots the critical Reynolds number Re_{cr} against the oblique angle of the riblets ϕ. In the figure, Re_{cr} for transverse riblets with $\phi = 90°$ where the riblets were aligned perpendicular to the streamwise direction is also plotted for comparison. Re_{cr} increased to about 4750 even when the riblets were inclined to the streamwise direction at ϕ = 20°, and rapidly increased with further increasing ϕ until it reached the value for the plane Poiseiulle flow (Re_{cr} = 5772) at $\phi = 45°$. When the riblets were inclined up to 90°, the critical Reynolds number remained at the same value as that in the smooth wall case. In other words, the transverse riblets which had a very small spacing of $0.11h$ (or a large wavenumber of 57) did not work as the distributed 2-D roughness from the instability viewpoint. Furthermore, we confirmed that the wavenumbers of the instability waves for these oblique riblets were in between those for the streamwise-riblet and smooth-wall cases.

Here, the result on the transverse riblets with small ridge-spacing is in contrast to the case of 2-D grooves with larger wavelengths (*i.e.*, lower wavenumbers less than 10) examined thus far [100–103] in which 2-D small-amplitude surface corrugations (or transverse grooves with sinusoidal cross-section) reduced the critical Reynolds number for the linear instability significantly. In the stability analysis by Floryan [101], the 2-D grooves definitely promoted the growth of T-S waves even with extremely small groove height over the wide range of groove wavenumbers from 0.1 to 10. Furthermore, Ma'mun & Asai [104] examined experimentally the effect of oblique corrugations (sinusoidal grooves) with the wavenumber of 2–3 times the T-S wavenumber in a boundary layer and showed that the destabilizing effect was strongest for 2-D grooves. On the other hand, when the groove wavenumber was much larger than the wavenumver of T-S waves ($\sim$ 1) like as in the present

experiment, the interaction between 2-D T-S waves and the transverse riblets/grooves would be too weak to influence on the development of long-wavelength T-S waves. Here, the streamwise wavenumber of the oblique riblets $\beta_x = 2\pi h sin\phi/s$ were 19.5, 28.5 and 40 for $\phi = 20^\circ$, 30° and 45°, respectively. Thus, we may say that the interaction between the 2-D T-S wave (with wavenumber of 1) and the mean flow distortion due to oblique riblets was not significant for the ratio of the streamwise wavenumber of riblets to the T-S wavenumber larger than 40.

To further elucidate the difference in the destabilizing effect between the streamwise and oblique riblets, we examined the structure of the instability wave on the oblique and transverse riblets. Figs. 2.16(a) and (b) display the amplitude distributions of the streamwise velocity disturbance (excited at ω = 0.27) at Re = 5000 in the channel with oblique (45°) and transverse riblets, respectively, by comparing to that of the T-S wave in the plane Poiseuille flow without riblets. In the figure, the mean velocity profile is also plotted. Here, the measurement was conducted at the mid position of the riblet valley. We can see that the peak amplitudes in the upper and lower channel halves were the same and the amplitude distribution was almost the same as that of T-S wave in the smooth-wall channel, without shifting toward the bottom of riblets, for both the cases. We also examined the amplitude distributions for $\phi = 20^\circ$ and 30° and found the peak amplitude on the ribbed surface was larger than that on the smooth surface but the difference in the peak amplitude observed in the case of the streamwise riblets was reduced with increasing ϕ. That is, the difference in the peak amplitude between the smooth and ribbed surfaces were 6.7% and 2.7% for $\phi = 20^\circ$ and 30°, respectively. The gradual change in the amplitude distribution was in correspondence to the dependence of the destabilizing effect on the oblique angle of riblet alignment.

2.6 Conclusions

The effect of riblets (longitudinal grooves) on the streamwise growth of T-S waves was examined experimentally in a channel flow. Riblets having triangular ridges and trapezoidal valleys, with a height-to-width ratio of 0.5, were glued on the upper channel wall, while the lower wall was sufficiently smooth. The ridge spacing of riblets (s) was 11% of the channel half-depth (h)

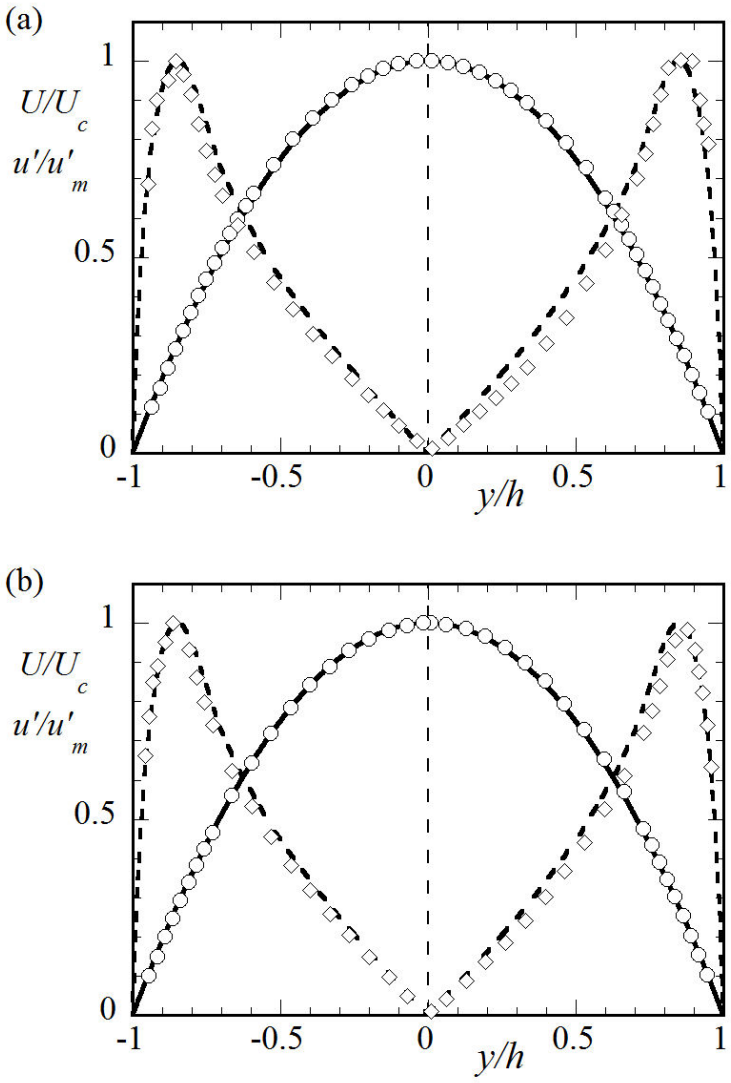

FIGURE 2.16: The y-distributions of the mean velocity U ($\circ$) and the amplitude u' of T-S wave excited with $\omega = 0.27$ ($\diamond$) at $Re = 5000$ in the channel with oblique riblets ($\phi = 45°$) in (a) and transverse riblets in (b). Solid and dotted curves represent the parabolic profile and the amplitude distribution by the linear stability theory for the smooth-wall case, respectively.

which gave a non-dimensional wavenumber ($2\pi h/s$) of 57, and the height of the ridges was $0.055h$. In terms of the roughness Reynolds number using the riblet height (k) and the friction velocity (u_τ) of the laminar parabolic flow, $u_\tau k/\nu$, the riblet height was only 4.9 – 6.0 for Re = 4000 – 6000, and therefore the riblets in the present experiment was considered to be of viscous-sublayer size. It is also noted that the square root of the groove cross-sectional area $(A_g^+)^{1/2}$ (introduced by García-Mayoral & Jiménez [88]) was 7 – 8.5 for Re = 4000 – 6000. In addition to the flow response to streamwise riblets whose ridges were aligned in the streamwise direction, the responses to oblique riblets whose ridges were inclined to the streamwise direction were examined to clarify how the instability characteristics were modified by the riblet alignment.

We first showed that the growth of T-S waves was intensified significantly by the streamwise riblets. Consequently, the critical Reynolds number for the small-amplitude T-S waves Re_{cr} (5772 for the linear instability of plane Poiseuille flow) was decreased to about 4200. The destabilizing effect of the present viscous-layer-scale riblets was much stronger than that for lower-wavenumber (≤ 10) grooves studied by Moradi & Floryan [94] in which the grooves with wavenumber of 10 and height of $0.06h$ reduced Re_{cr} only to 5500. The present riblets only modified the velocity field very close to and inside the grooves and the mean flow (base flow) exhibited a parabolic velocity profile with an offset of $0.02h$ between the virtual wall position and the riblet tip. Indeed, the amplitude and phase distributions of the instability wave were almost the same as those of the 2-D T-S wave except in the vicinity of the ribbed surface where the local maximum in the amplitude distribution was slightly larger than that for the smooth wall. Nevertheless, an instability mechanism due to the presence of an inflection point in the velocity profile inside the grooves worked against the viscous effect and enhanced the instability of the Poiseuille flow. Thus, the experiment clearly showed that only a slight change in the near-wall flow due to the presence of small-sized riblets could control the flow instability. Here, $(A_g^+)^{1/2}$ was 7.2 at the critical Reynolds number Re_{cr} = 4200, which was close to the critical value (for the onset of the instability of flow over riblets) analyzed by García-Mayoral & Jiménez [88].

Secondly, we examined the dependence of the instability characteristics on the oblique (inclination) angle (ϕ) of riblet alignment and found that as the oblique angle of the riblet alignment was increased, the destabilizing effect of

the riblets weakened. The critical Reynolds number increased to about 4750 when the riblets were inclined at $\phi = 20^\circ$ and approached that in the smooth-wall case at $\phi = 45^\circ$. Correspondingly, we found no noticeable difference in the amplitude and phase distributions of the disturbance velocity from those in the smooth-wall case in the whole flow region including the vicinity of the ribbed surface when the riblet alignment was inclined at $\phi = 45^\circ$. Such a dependence of the instability characteristics on the oblique angle of riblet alignment contrasted with the case of grooves with much lower wavenumbers where transverse grooves ($\phi = 0^\circ$) had the strongest destabilizing effect [94, 101, 104].

Chapter 3

Effects of streamwise riblets on lateral turbulent contamination in a boundary-layer

3.1 Introduction

In chapter 2, the effect of riblets with drag-reducing size (for wall turbulence) on the linear instability stage concerning growth of Tollmien-Schlichting (T-S) waves was clarified. When streamwise grooves/riblets are applied in the flow including laminar and transitional regimes, it is also important to examine another possible influence on the boundary-layer transition, that is, effects of riblets on the lateral growth of turbulent spot or wedge. When a boundary layer is subjected to high free-stream turbulence, the transition is often caused by transient disturbance growth generating low-speed streaks, which breakdown due to the streak instability and are followed by the occurrence of turbulent spots (Matsubara & Alfredsson (2001) [45]; Asai, Minagawa & Nishioka (2002) [54]; Mans, Kadijk, de Lange & van Steenhoven (2007) [58]; Brandt, Schlatter & Henningson (2004) [62]; Asai, Konishi, Oizumi & Nishioka (2007) [105]; Zaki (2013) [64]; Ho, Asai & Takagi (2017) [60]). On the other hand, an isolated roughness element such as a small protuberance or the attachment of a small particle on the surface can directly cause a turbulent wedge to develop if the roughness Reynolds number is above a certain critical value (Mochizuki (1961) [106], Morkovin (1990) [9]). Thus, in order to estimate the friction drag in the whole boundary layer including the transition regime (over riblets), it is important to clarify the influences of riblets on the lateral growth of localized turbulent region, i.e., the lateral turbulent

contamination.

Development of a turbulent spot and wedge has been studied by many researchers since Emmons (1951) [107] first reported occurrence of turbulent spots in a boundary layer transition: for instance, see Schubauer & Klebanoff (1956) [108]; Elder (1960) [109]; Mochizuki (1961) [106]; Wygnanski, Sokolov & Friedman (1976) [110]; Gad-el-hak, Blackwelder & Riley (1981) [111]; Perry, Lim & Teh (1981) [112]; Wygnanski & Friedman (1982) [113]; Lindeerg, Fahlgren, Alfredsson & Johansson (1985) [114]; Henningson, Spalart & Kim (1987) [115]; Asai, Sawada & Nishioka (1996) [116]; Jocksch & Kleiser (2007) [117]; Kuester & White (2016) [118] and Goldstein, Chu & Brown (2017) [119]. A first detailed experiment by Schubauer & Klebanoff (1956) [108] included development of both a turbulence wedge and spot which were generated artificially by a small sphere and spark, respectively. Results showed that the turbulent wedge grew laterally with a half vertex angle of 6.4° for a fully turbulent region and 10.6° for a region including an intermittent region, while the turbulent spot grew with the same lateral spreading angle as the turbulent wedge. Henningson, Spalart & Kim (1987) [115] reproduced development of a turbulent spot in a direct numerical simulation and showed that the spot developed with a self-similar structure downstream at a half-angle of 7° or 10° depending on the definition of the edge of the turbulent region.

Several mechanisms have been considered for the growth of a turbulent spot/wedge. Gad-el-hak, Blackwelder & Riley (1981) [111] proposed a growth mechanism termed growth by destabilization on the basis of their visualization study of turbulent spots. They considered that turbulent eddies inside the spot excited instability of the ambient laminar boundary layer, leading to the new generation of turbulence there. Wygnanski, Sokolov & Friedman (1976) [110] and Wygnanski & Friedman (1982) [113] generated a turbulent spot by a spark disturbance and observed that oblique waves appearing outside the spot broke down to generate new vortices; they considered that breakdown of the oblique waves, if it occurred, could contribute to the lateral spreading of the spot. In a direct numerical simulation, Henningson, Spalart & Kim (1987) [115] reported the breakdown of oblique waves at both tips of the spot. For a turbulent wedge, on the other hand, development and breakdown of oblique waves (like for the spot) have not been reported, while successive generation of streamwise vortices and related low-speed streaks has been observed in the ambient laminar boundary layer. They were considered to be responsible for the lateral contamination, as revealed

in visualizations by Mochizuki (1961) [106] and Asai, Sawada & Nishioka (1996) [116]. A recent visualization study by Kuester & White (2016) [118] and a numerical simulation by Goldstein, Chu & Brown (2017) [119] also strongly suggested that successive generation of low-speed streaks in a turbulent wedge was a main growth mechanism for the lateral spreading of the wedge as well as for that of a turbulent spot. Importantly, despite the fact that the details of turbulence structures in the interface region were not the same in the spot and wedge, the lateral growth that finally occurred had the same half-spreading-angle of about 10° in both cases, as first reported by Schubauer & Klebanoff (1956) [108].

Here, our interest is in the influence of streamwise riblets on the lateral spreading of a turbulent wedge when drag-reducing-sized riblets around s^+ = 20 (for the turbulent region) are applied. In this concern, Strand & Goldstein (2011) [120] examined growth of a turbulent spot over triangular cross-section riblets (with height-to-spacing ratio ~ 1) for $R_x \leq 2 \times 10^5$ by a direct numerical simulation and demonstrated that the riblets reduced the lateral spreading angle of the spot (about 6.3° in the absence of riblets) by 14%. In their result, riblets whose height was 21 in wall units using the averaged friction velocity inside the spot significantly affected the early stage of turbulent-spot development, but this influence appeared to weaken in the downstream development stage. In their simulation, the momentum thickness Reynolds number of the Blasius boundary layer was only about 145, very close to the critical Reynolds number (based on the momentum thickness) $R_\theta \sim 130 - 150$ for the subcritical transition of Blasius flow caused by highly energetic hairpin vortices (see Asai & Nishioka, 1995 [121]). We therefore speculate that the early development of the turbulent spot might be sensitive to the presence of riblets, but not so much to the developed turbulent wedge/spot. It remains to be clarified how significantly the lateral turbulent contamination of the developed turbulent wedge could be influenced by riblets at higher Reynolds numbers.

We also point out another possible influence. Our recent experiment (Ho & Asai, 2018 [122]) demonstrated clearly that streamwise riblets of drag-reducing size could strongly destabilize the laminar flow, and thus such a destabilizing effect might have some influence on lateral growth when the Reynolds number increases. On the other hand, riblets generally have the effect of suppressing near-wall turbulence. The maximum rms value of streamwise velocity fluctuations was reduced by about 10% in the near-wall region

over riblets, compared to that over the smooth surface, in the experiment by Choi (1989) [85]. In a numerical simulation of a flow over triangular riblets, Choi, Moin & Kim (1993) [87] found that the normal-to-wall and spanwise velocity fluctuations were reduced by 10% while the streamwise velocity fluctuations were lower by 5%. It is interesting to clarify how these opposite effects of riblets (in laminar and turbulent flows) can affect the lateral contamination at sufficiently high Reynolds numbers.

In the present experimental study, a developed turbulent boundary layer was produced locally (in span) by cylinder roughness elements placed over a spanwise portion in a zero-pressure-gradient boundary layer to investigate the effects of riblets on the lateral growth of developed turbulent wedge, including the above-mentioned points. In the following, Section 3.2 describes the experimental setup and the flow condition in the experiment. Section 3.3 explains lateral growth of the localized turbulent region generated by roughness elements over the smooth surface up to $R_x = 6 \times 10^5$, focusing on the development of wall turbulence structures in the laminar-turbulent interface region. Section 3.4 compares lateral growth of the turbulent region to clarify possible influences of riblets on lateral turbulent contamination. Section 3.5 summarizes the main results.

3.2 Experimental setup and procedure

The whole experiment was conducted in a low turbulence wind tunnel of the open jet type. Fig. 3.1 display a schematic of the wind tunnel and a photograph of the test section. The wind tunnel had three damping screens spanning the diffuser, and five damping screens and a honeycomb in the settling chamber of 1200 $\times 1200 mm^2$ in cross section. The area ratio of the contraction to the test section of 400 $\times 400 mm^2$ was 9. The maximum flow velocity in this tunnel was 12 m/s in the test section. As illustrated in Fig. 3.2, the boundary-layer plate consisted of a 5-mm thick and 300-mm long aluminum plate with an elliptic nose whose major axis was 20 times the minor axis, followed by a 20-mm thick and 900-mm long resin plate. As for the coordinate system, x was the streamwise distance measured from the leading edge, y the normal-to-wall distance, and z the spanwise distance.

The experiments were conducted at the free-stream velocity U_∞ = 8 and

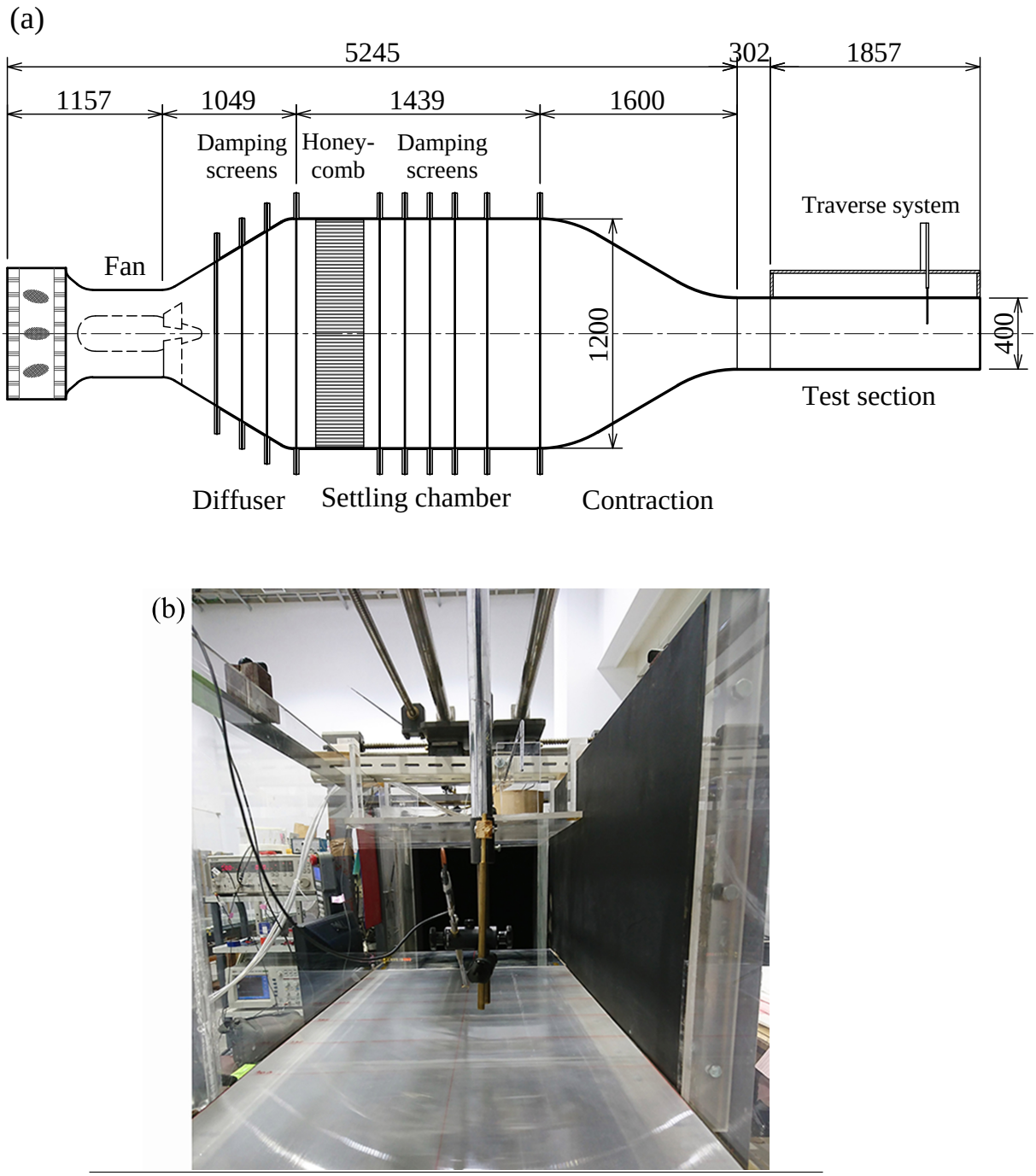

FIGURE 3.1: Wind tunnel facility. (a) Schematic of the wind tunnel (dimensions in mm, not in scale), (b) photograph of the test section.

11.5 m/s. The free-stream turbulence was less than 0.1% of U_∞ at the leading edge location in terms of the root-mean-square (rms) value of the streamwise velocity fluctuations u'. Inside the boundary layer, u' was gradually increased downstream but the boundary layer was kept laminar up to the most downstream observation location x = 800 mm at the maximum freestream

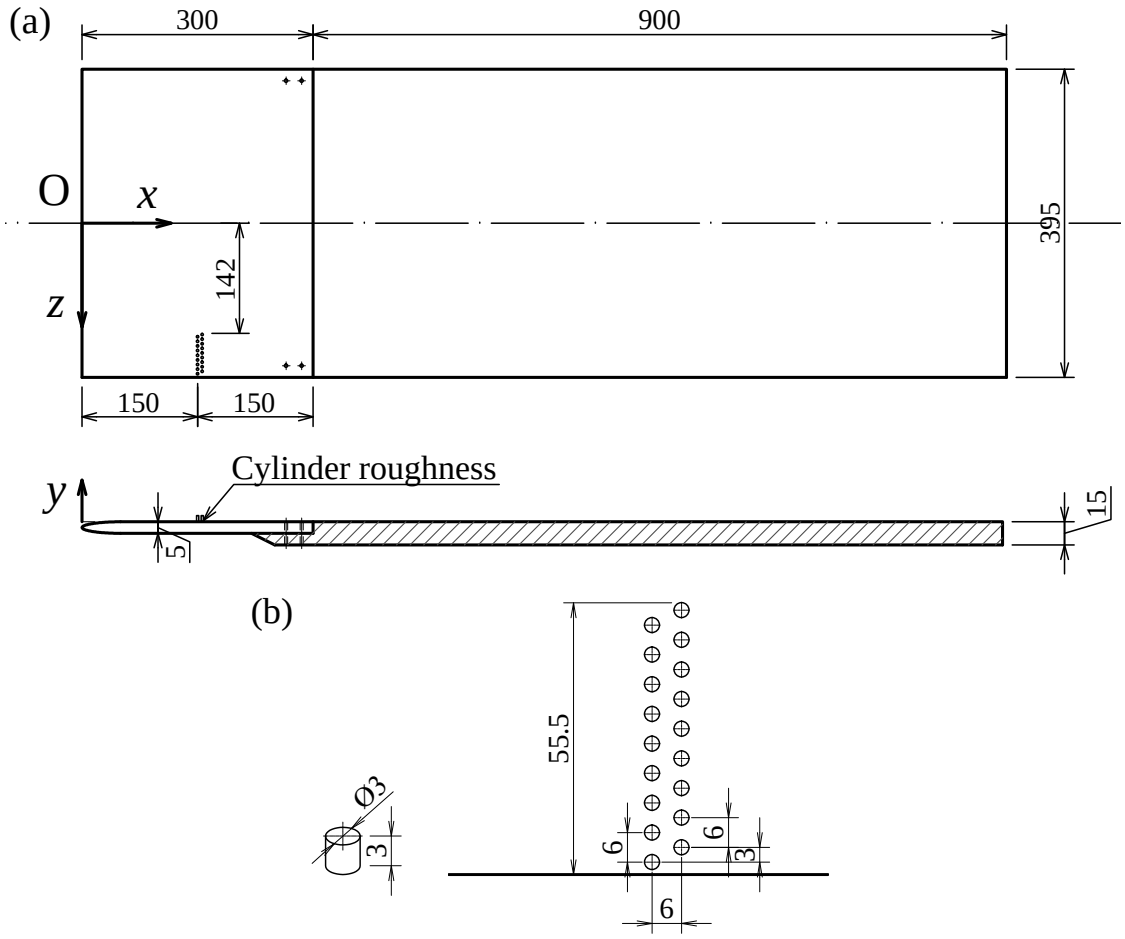

FIGURE 3.2: Boundary-layer plate (dimensions in mm, not in scale) and the coordinate systems. (a) Flat plate and (b) details of roughness elements

velocity (U_∞ = 11.5 m/s), in the absence of tripping device at an upstream location. As shown later, the velocity profiles in the laminar boundary-layer exhibited the Blasius flow profiles. The displacement-thickness Reynolds number $R^* = U_\infty \delta^* / \nu$ was about 1120 and 1340 at x = 800 mm at U_∞ = 8 and 11.5 m/s, where δ^* was the displacement thickness of the Blasius flow on the smooth wall and the ν was the kinematic viscosity. Here, the critical Reynolds number for the linear instability of the Blasius flow is 520 in terms of R^* according to the linear stability analysis (with parallel-flow assumption) and is about 450 according to the direct numerical simulation of the Navier-Stokes equations by Fasel & Konzelman (1990) [123] and the calculation based on the parabolized stability equations by Bertolotti, Herbert & Spalart (1992) [124].

In order to examine lateral turbulent contamination, cylinder-roughness-elements were over some spanwise extent (over z = 142 – 196 mm) of the

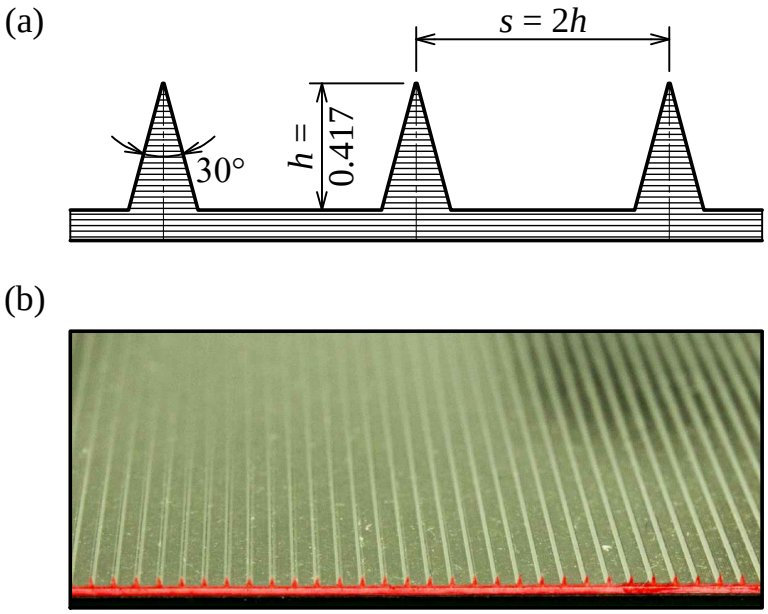

FIGURE 3.3: Riblet model. (a) Geometry (dimensions in mm), (b) photograph of riblet surface.

boundary layer plate at an upstream location, x = 150 mm. The diameter (d) and height (k) of the cylinders were both 3 mm, and they were arranged in a two-row configuration. In each spanwise row, the cylinder spacing was 10 mm, and the two rows (separated by 10 mm in the streamwise direction) were staggered by 5 mm in the spanwise direction. The roughness Reynolds number R_k was about 1580 and 2270 for U_∞ = 8 m/s and 11.5 m/s, respectively. Downstream of the cylinder roughness elements, a turbulent boundary layer developed with spreading the turbulent area laterally.

The photograph and geometry of the riblets used here are given in Fig. 3.3. The present riblets were the same as those used in our recent paper (Ho & Asai, 2018 [122]). The riblets had triangular ridges with ridge angle of 30° and trapezoidal valleys. The ridge-spacing (s) was 0.83 mm and the height-to-spacing ratio (k/s) was 0.5. Note that the edge thickness of the triangular ridge was 0.005 mm. Riblets were created by coating paint on a thin flexible plastic panel, and the riblet-sheet was glued to the boundary-layer plate over the range of x = 300 – 1200 mm. The riblet surface of 900 mm in length was connected to the upstream flat-surface part in such a way that the tips of riblet-ridges were 0.15 mm higher than the upstream smooth surface. The riblet sheet was replaced to a flat plastic plate in the smooth-surface experiment.

The streamwise velocity component, whose time-mean and fluctuation components were denoted by U and u, respectively, were measured using a constant temperature hot-wire anemometer. The length of the hot-wire sensor, a tungsten wire of 5 μm in diameter, was 1mm, which could sense a streamwise velocity component averaged almost over the riblet-ridge spacing (0.83 mm) in the spanwise direction. Calibration of the hot-wire was made using a calibration function $U = (AE^2 - B)^{1/0.45}$, where E is the output voltage of the hot-wire at velocity U, and A and B are the calibration constants. The hot-wire probe could be traversed in all directions. Hot-wire data were stored in a PC after 16-bit analogue-to-digital conversion. In order to visualize lateral turbulent contamination, PIV measurements as well as smoke-wire visualization were performed. In PIV measurements, micron-sized smoke particles were seeded uniformly in the flow from the inlet of the wind tunnel, and double-pulsed Nd:YAG laser-sheet images were captured using a CCD camera with 2048 $\times$ 2048 pixels. The double-frame images (more than 800 pairs) were analyzed using the adaptive correlation algorithm (DANTEC Dynamic Studio) with a final interrogation window of 16 $\times$ 16 pixels. The interrogation cells were overlapped by 50% in each direction, giving 255 $\times$ 255 velocity vectors with a spatial resolution of 0.55 $\times$ 0.55 mm^2 for the area of 140 $\times$ 140 mm^2 in the (x, y) plane. In the smoke-wire visualization, a smoke-wire was stretched in the spanwise direction near the wall and a sequence of top-view pictures were taken with a digital high-speed video camera with 1024 $\times$ 1024 pixels.

3.3 Lateral turbulent contamination on the smooth surface

Before focusing on the effects of riblets, we would like to explain lateral growth of wall turbulence artificially generated locally in span in a laminar boundary layer over the smooth surface. Fig. 3.4 illustrates velocity profiles of laminar boundary layer at x = 500, 600 and 700 mm at U_∞ = 8 m/s in the absent of roughness elements triggering the transition by comparing to the Blasius profiles at the corresponding x-locations. Here, in comparison, we assumed that the Blasius boundary-layer started at a location 10 mm upstream of the leading edge (due to the elliptic leading edge). The velocity distributions almost completely coincided with the Blasius flow profiles. The

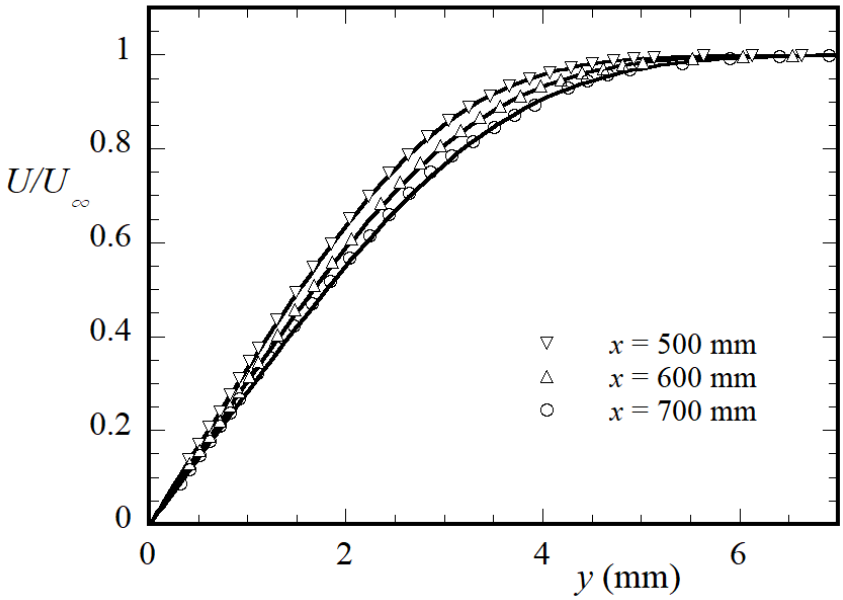

FIGURE 3.4: The y distribution U at x = 500, 600 and 700 mm in the laminar boundary layer at U_∞ = 8 m/s. Solid curves represent the profiles of Blasius flow.

displacement thickness δ^* and the momentum thickness θ were respectively 2.01 mm and 0.770 mm at x = 700 mm. Therefore, the shape factor H exhibited a constant value of 2.61, very close to the value of the Blasius flow (H = 2.59).

Turbulent boundary layer was produced locally in span in this boundary layer by gluing the cylinder-roughness-elements (mentioned above) over a short span of z = 142 – 196 mm on the boundary layer plate at an upstream location, x = 150 mm. The roughness Reynolds number R_k (= $U_\infty k/\nu$ where k was the height of cylinder-roughness and ν the kinematic viscosity) with k= 3 mm was about 1580 and 2270 at U_∞ = 8 and 11.5 m/s, respectively. The x-Reynolds number, R_x, was 0.8×10^5 and 1.15×10^5 at the roughness location x_k= 150 mm, at U_∞ = 8 and 11.5 m/s, respectively. Here, according to an experiment on the relationship between the transition Reynolds number and the roughness Reynolds number by Mochizuki [106], the Reynolds number, R_x =0.8×10^5 at the roughness location was sufficiently higher than the critical value at which the turbulent wedge can soon develop with lateral contamination from the roughness location with R_k = 1580. The detail of the lateral growth of turbulent region will be explained later. Fig. 3.5 displays the y-distribution of mean velocity U at x = 800 mm (the furthest downstream

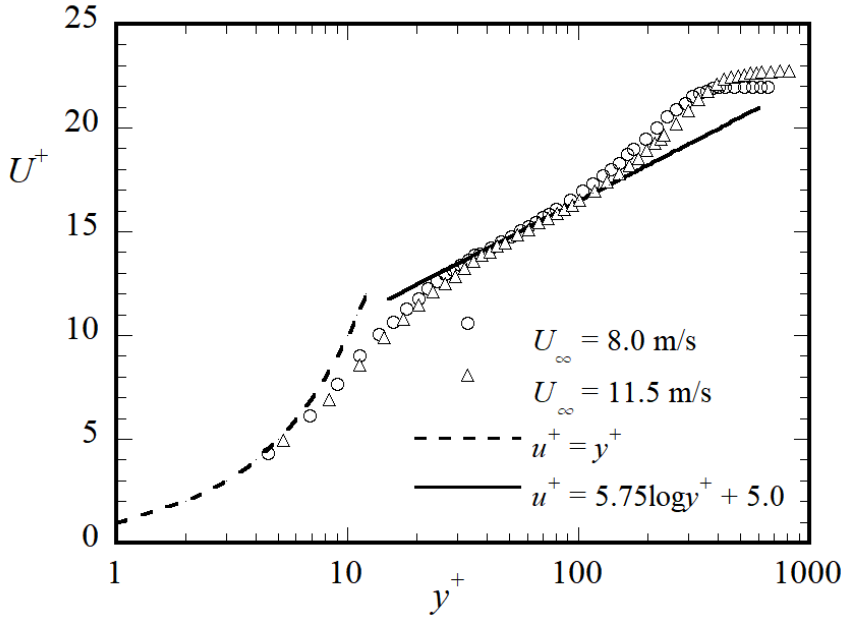

FIGURE 3.5: The y-distributions of U at x = 800 mm in the developed turbulent region downstream of roughness elements at U_∞ = 8 m/s and 11.5 m/s.

observation location) in the developed turbulent region (at z = 150 mm) at U_∞ = 8 and 11.5 m/s. The velocity distribution exhibited a log-law (with κ = 0.40) and the turbulent Reynolds number (R_τ) based on the friction velocity u_τ and the boundary-layer thickness δ was about 400 and 520 at U_∞ = 8 and 11.5 m/s, respectively. The momentum-thickness Reynolds number (R_θ) at x = 800 mm was about 940 and 1310, respectively, at U_∞ = 8 and 11.5 m/s.

Then, let us explain the lateral turbulent contamination in these cases. Figs. 3.6(a) to (d) display the distributions of rms value of streamwise velocity fluctuations u' in the (y, z) cross-section at x = 350, 500, 650 and 800 mm (R_x = 1.84, 2.63, 3.42 and 4.21$\times 10^5$), respectively, at U_∞ = 8 m/s. Here, u' was measured by a hot-wire anemometer. The contour maps exhibit a similar structure of the laminar-turbulent interface, and u' took a maximum more than $0.12U_\infty$ near the wall in the interface region at each x-location. As shown later, the appearance of the local maximum in u' in the interface region resulted from the fact that a large-scale turbulent motion/structure developed intermittently at the outer edge of the turbulent region. The similar structure of the laminar-turbulent interface (in the mean flow field) enabled us to determine the edge location (z_t) of the turbulent region definitely. Fig. 3.7(a) displays the distribution of u' in the (x, z) plane near the wall (y = 0.6 mm)

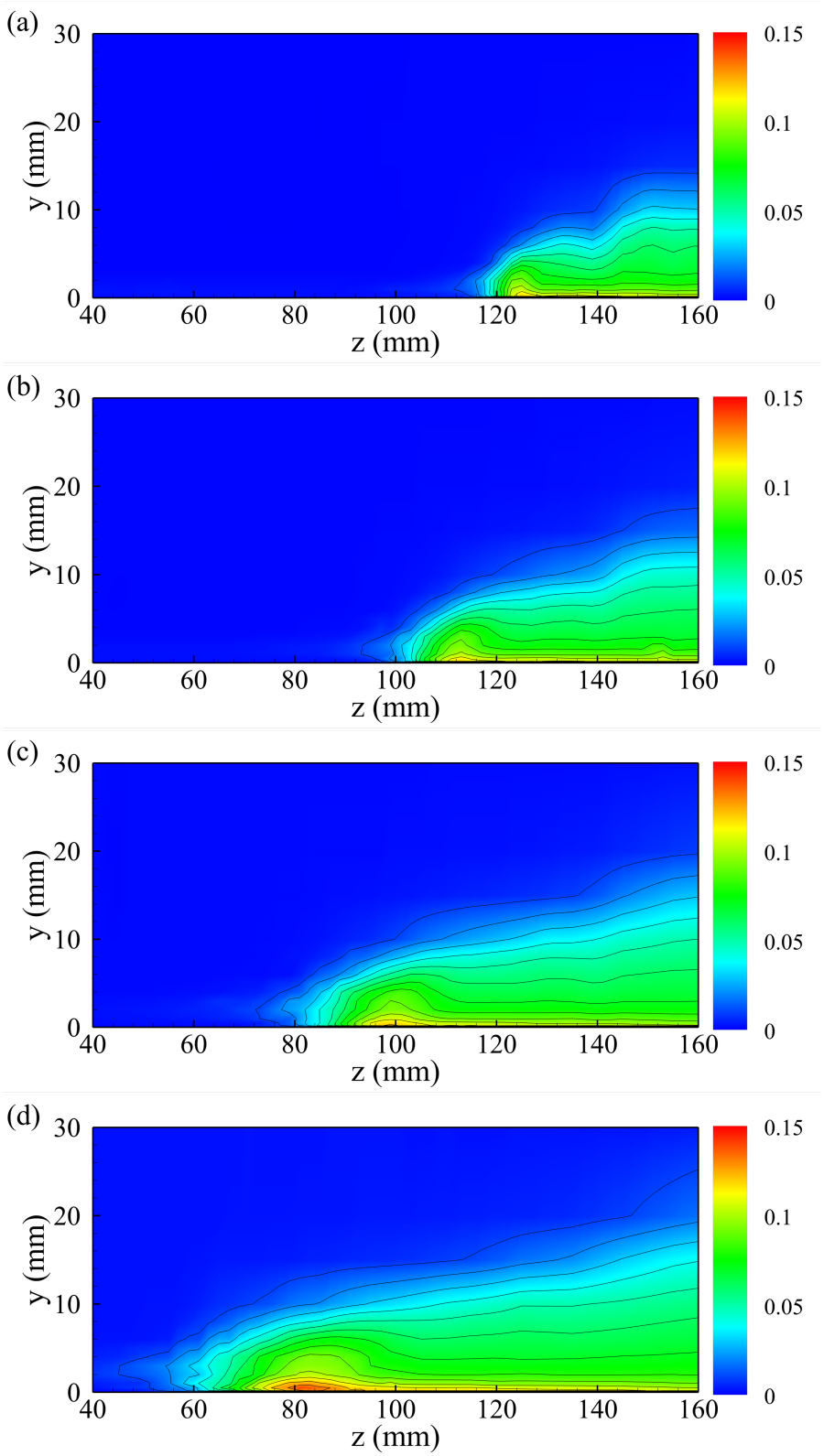

FIGURE 3.6: Contour maps of the rms value u'/U_∞ over smooth surface in the (y, z) plane at (a) x = 350; (b), 500; (c), 650 and (d), 800 mm at U_∞= 8 m/s. The interval of contour lines is 0.01.

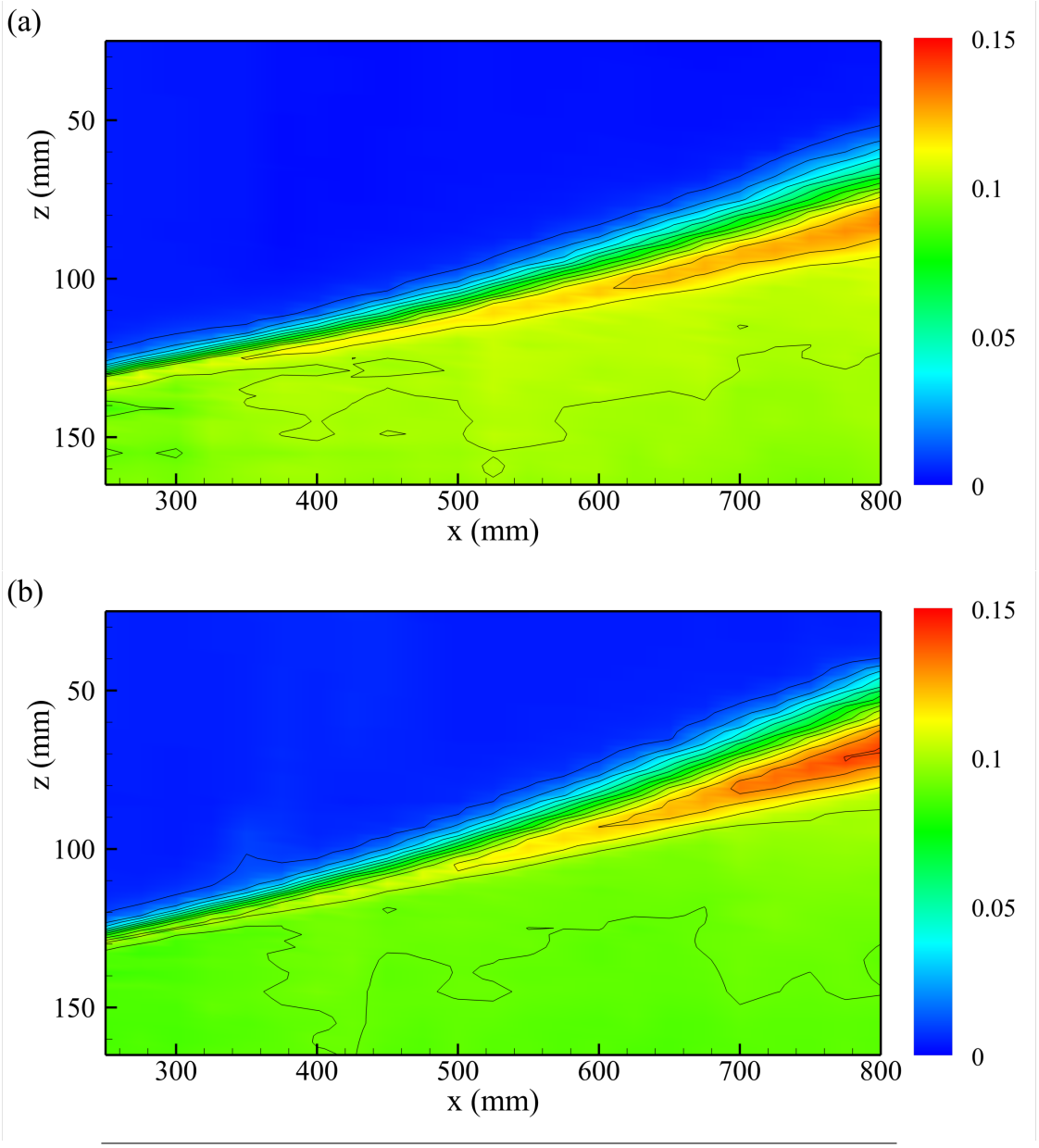

FIGURE 3.7: Contour maps of the rms value u'/U_∞ over smooth surface in the (x, z) plane at $y = 0.6$ mm (measured by a hot-wire). (a) $U_\infty = 8$ m/s and (b) $U_\infty = 11.5$ m/s. The interval of contour lines is 0.01.

at $U_\infty = 8$ m/s: here, note that u' took a maximum at and around $y = 0.6$ mm at each x-location in the interface region (see Fig. 3.6). The similar measurement was also conducted at $U_\infty = 11.5$ m/s and the result is illustrated in Fig. 3.7(b). From these figures, we determined the edge of the turbulent region (including the intermittent region). Below, we defined the edge location of the turbulent region as the z position at which u' near the wall (Fig. 3.7) was decreased down to 30% of the maximum value of u' at each x-location.

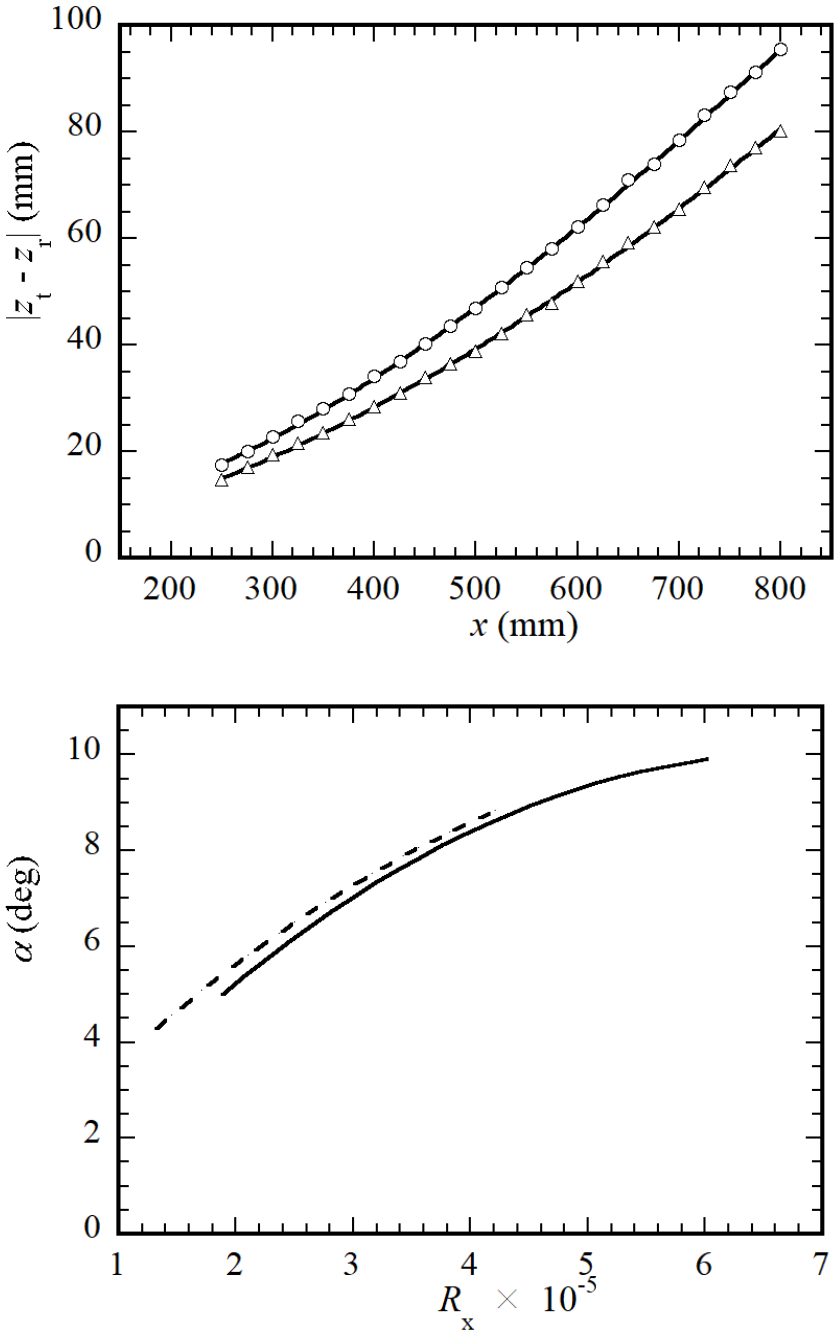

FIGURE 3.8: Lateral growth and spreading angle (α) of the turbulent region in the smooth-surface case. (a) $|z_t - z_r|$ vs x at U_∞ = 8 m/s (△) and 11.5 m/s (○); (b) α vs R_x at U_∞ = 8 m/s (dotted curve) and 11.5 m/s (solid curve).

Figure 3.8(a) illustrates the edge location of the turbulent region against x at U_∞ = 8 m/s and 11.5 m/s, in terms of $|z_t - z_r|$, in which the distance from the edge of the roughness area (z_r) is 142 mm. Both spreading curves could be extrapolated to the upstream roughness x-location (x = 150 mm). We could

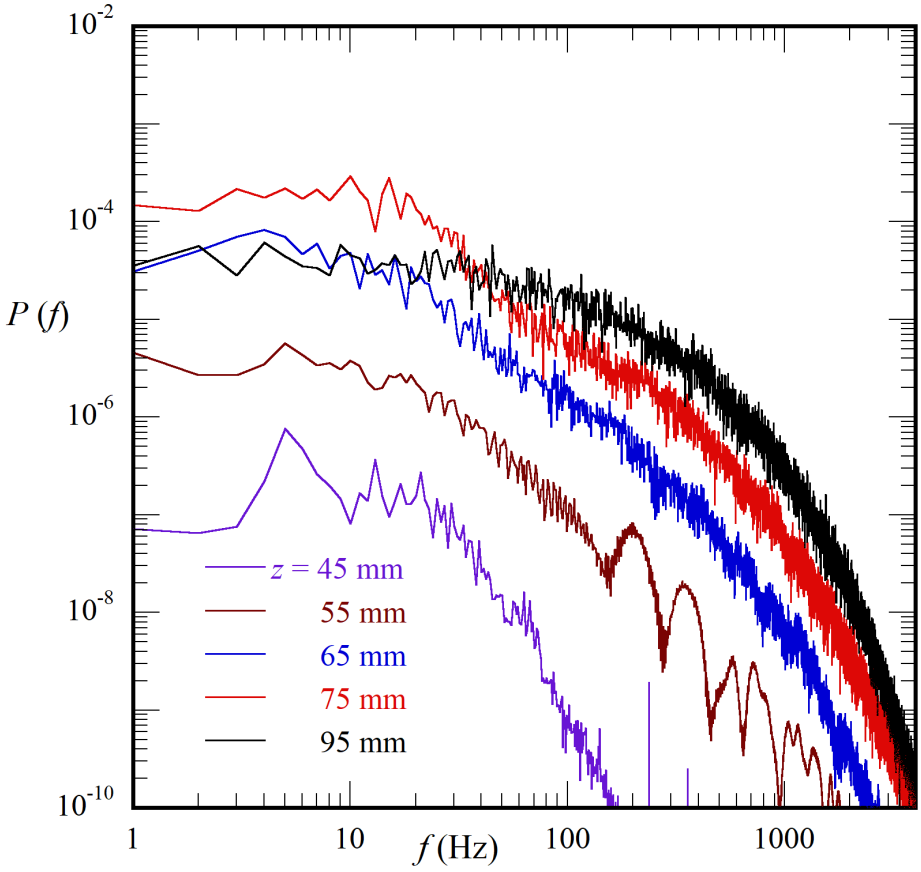

FIGURE 3.9: Power spectra of streamwise velocity fluctuations $P(f)$ near the wall (y = 0.6 mm) at x = 800 mm at and around the laminar-turbulent interface region, at U_∞ = 8 m/s.

therefore see that the lateral growth of the turbulent region started from the roughness location in both cases. We could also see that the spreading angle of the turbulent region depended on the Reynolds number, as seen from the comparison. The spreading angles were obtained from Fig. 3.8(a), and plotted against the x-Reynolds number R_x in Fig. 3.8(b) to show the dependence of the Reynolds number on lateral contamination. The lateral spreading angle approached a value slightly larger than 10° for $R_x > 6 \times 10^5$, which was almost the same as the half spreading angle of the turbulent wedge or spot including an intermittent region (about 10° -– 10.6°) in the experiment by Schubauer & Klebanoff (1956) [108]. Here, we note that the spreading angle of course depends on the definition of the outer edge of the turbulent region. When we defined the edge as the z-position at which u' took a local maximum in the laminar-turbulence interface region for each x location (see Fig. 3.7), the spreading angle was found to approach about 7.5°.

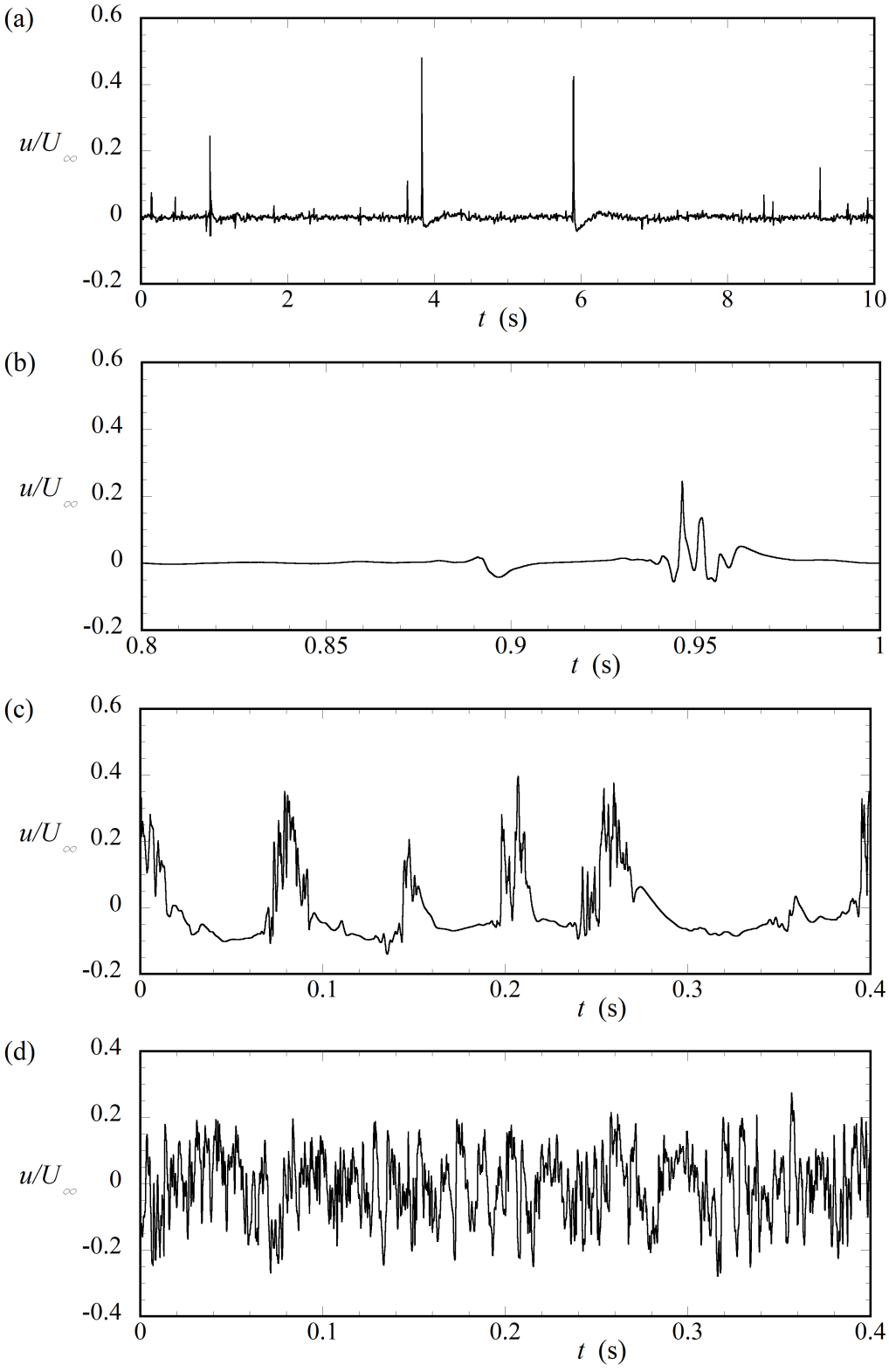

FIGURE 3.10: Waveform of u-fluctuations in the laminar-turbulent interface region over the smooth surface at (x, y) = (800 mm, 0.6 mm) at U_∞ = 8 m/s. (a, b) z = 55 mm, (c) 75 mm, (d) 95 mm.

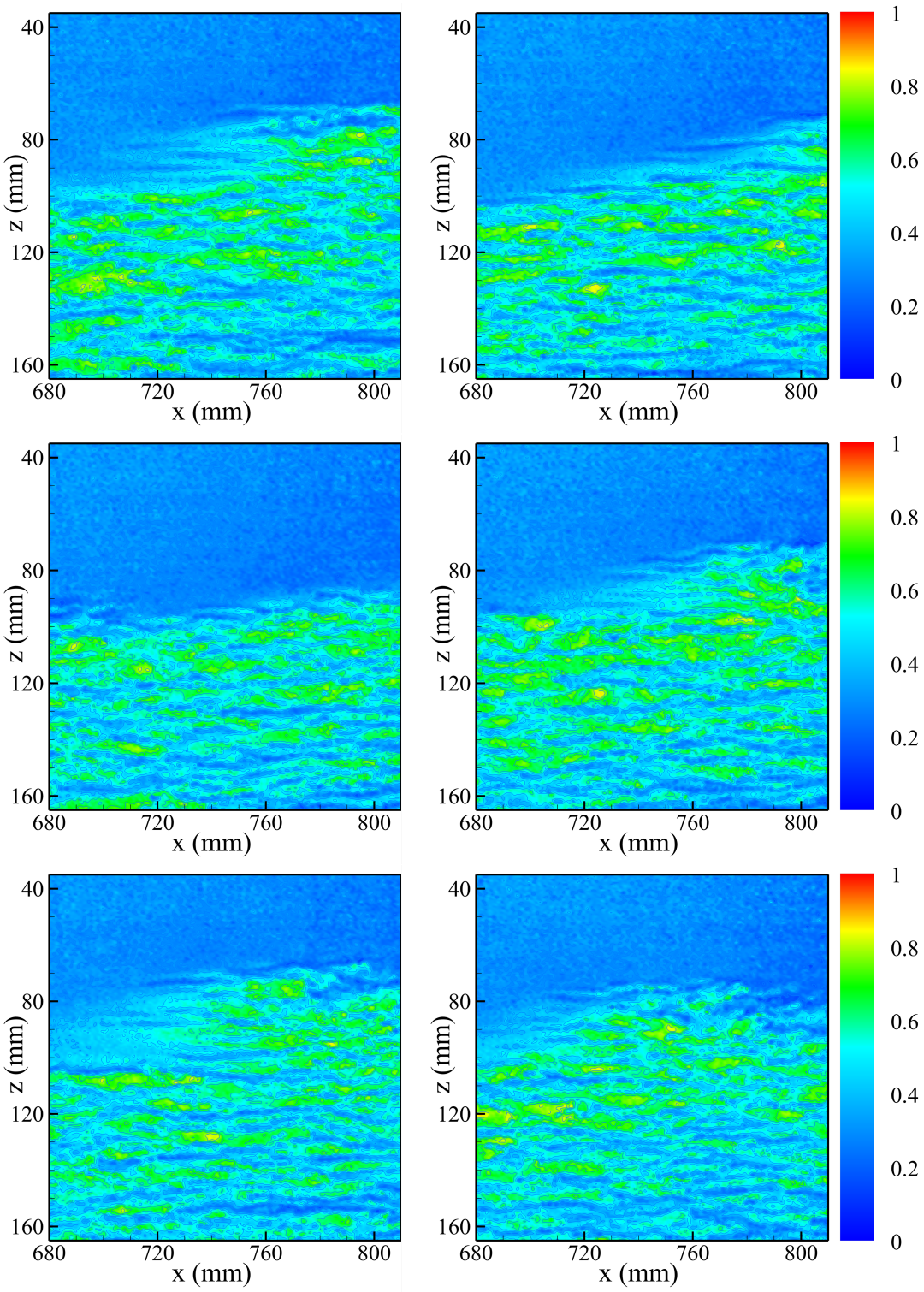

FIGURE 3.11: Instantaneous streamwise-velocity ($U + u$) in the (x, z) plane at y = 1.0 mm around the laminar-turbulent interface region, at U_∞= 8 m/s.

Another feature of the laminar-turbulent interface was also found by comparing spectra of streamwise velocity fluctuations at various z positions across the interface. Figure 3.9 displays power spectra $P(f)$ (scaled with U_∞^2) near the wall (y = 0.6 mm) in the interface region (over z = 45 – 95 mm) at x = 800 mm, at U_∞ = 8 m/s; the frequency resolution in the spectral analysis was 1 Hz. Referring to Fig. 3.7, u' took a maximum value at and around z = 75 mm, at which the spectrum exhibits growth of low-frequency components below 30 Hz. It is reasonable to speculate that a large packet of turbulent eddies like a large-scale structure consisting of multiple hairpins in the turbulent boundary layer (Adrian, 2007 [125]; Deng *et al.*, 2018 [126]) intermittently occurred in the interface region and/or was intermittently carried from the turbulent region towards the laminar region. Fig. 3.10 displays waveforms of streamwise velocity fluctuations (u) in the interface region (at and around z = 75 mm) corresponding to the spectra in Fig. 3.9, and showing that a turbulent packet (with time-scale of 0.02 – 0.03 s) consisting of high-frequency spike-like fluctuations (more than 200 Hz) was passing the hot-wire sensor at z = 75 mm intermittently with intervals over 0.05 – 0.1 s (or 10 – 20 Hz).

In order to identify the turbulence structure(s) in the interface between the laminar and turbulent region, the near-wall flow was visualized using PIV data. Figure 3.11 shows the instantaneous velocity field near the surface, including the edge of the turbulent region at U_∞= 8 m/s in terms of some typical pictures of streamwise-velocity contours. Here, a laser sheet illuminated a (x, z) plane (parallel to the wall) at $y \sim 1$ mm, which corresponded to a height of about $\delta^*/2$ in the laminar region and to about 24 in wall units in the developed turbulent region. As for the z-location corresponding to the edge of the turbulent region in average, see Fig. 3.7(a). Low-speed streaks, some of which exhibited a wavy motion due to streak instability, were observed at the outer edge of the interface region (see the upper right figure). In addition, we could see a large-scale structure followed by many low-speed streaks not unlike a turbulent spot (the lower left figure). Such a turbulent packet has not been demonstrated in past experiments on the turbulent wedge. The intermittent occurrence of the large-scale turbulent motion at the interface caused the increase of low-frequency spectral components (below 30 Hz) in Fig. 3.9, and correspondingly the largest intensity of u' at the outer edge of turbulent region became more and more remarkable with x, as seen in Fig. 3.7. Thus, it seems that the structure of the laminar-turbulent interface observed in the downstream was rather different from that in the early stage of turbulent

wedge which was mainly dominated by regeneration of streamwise or hairpin vortices (see Smith *et al.* (1991) [127]; Asai, Sawada & Nishioka (1996) [116]; Goldstein, Chu & Brown (2017) [119]). Development of such a large-scale turbulent structure with 10 -– 20 Hz (Figs. 3.9 and 3.10(c)) suggests that some instability mechanism (such as instability of Kelvin-Helmholtz type in a turbulent mixing layer) might set in the laminar-turbulent interface region, although the origin and generation mechanism of the large turbulent packet were not clarified in this study.

3.4 Effects of riblets on lateral turbulent contamination

In this section, to examine how lateral growth of the turbulent region was affected by riblets, a riblet sheet (shown in Fig. 3.3) was glued over part of the boundary-layer plate over x = 300 — 1200 mm. Here, the surface transition from smooth surface to ribbed surface at x = 300 mm was such that the tips of the riblet-ridges were about 0.15 mm (about 20% of the ridge spacing of riblets) higher than the upstream smooth surface, taking into account the virtual wall position of the ribbed surface where the mean velocity distribution approaches zero according to the theoretical analysis on a laminar viscous flow over riblets by Luchini, Manzo & Pozzi (1991) [91]. The upstream boundary-layer plate with cylinder roughness was the same as in the smooth-surface experiment and the whole experiment on riblet effects was conducted under almost the same experimental (air flow and temperature) conditions as the smooth-wall case so that we could directly compare the lateral growth of the turbulent region to the smooth-wall case (Section 3.3). In the following, y position over the riblets was measured from the virtual wall position 0.15 mm below the tips of riblet-ridges.

Figures 3.12(a) and (b) illustrate the distribution of the rms value of u-fluctuations u' in the (x, z) plane at y = 0.6 mm and 0.5 mm (where u' took a maximum in the interface region) over the riblets at U_∞ = 8 m/s and 11.5 m/s, respectively. The value of u' was slightly lower than that for the smooth-wall case in the laminar-turbulent interface region, but the other features of the lateral contamination were similar to those of the smooth-wall case. From these data, we obtained the lateral spreading angles as we did for the smooth

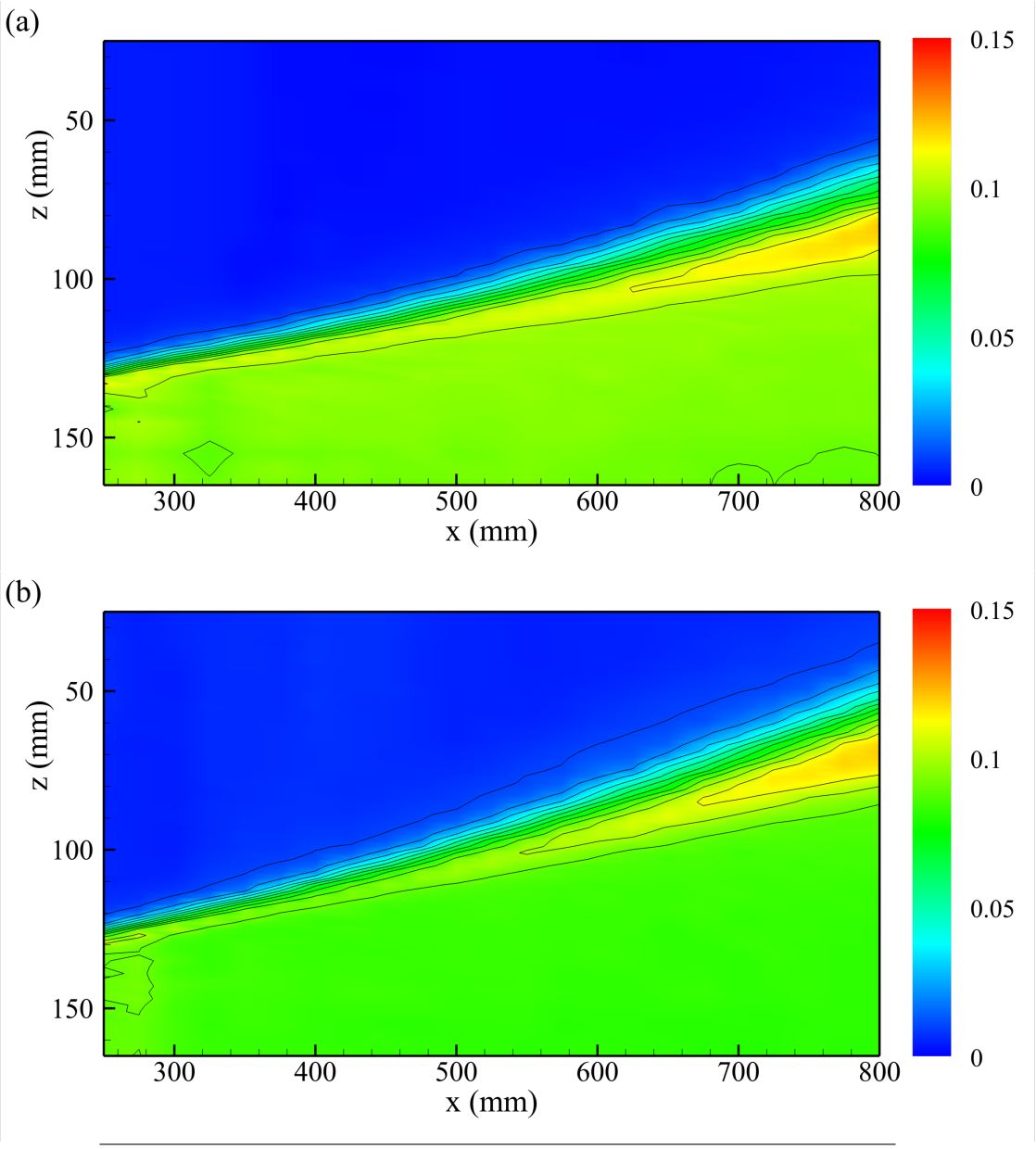

FIGURE 3.12: Contour maps of the rms value u'/U_∞ over riblets in the (x, z) plane at (a) y = 0.6 mm for U_∞= 8 m/s and (b) y = 0.5 mm for 11.5 m/s. Contour lines range from 0.01 to 0.12 with interval of 0.01.

wall case, and compared them. Figure 3.13 compares the lateral growth of the laminar-turbulent interface, in terms of the edge location (z_t) of the intermittently turbulent region to that for the smooth-wall case, at U_∞ = 11.5 m/s. We see only a small difference in the edge location of the turbulent region between the smooth surface and riblets. Indeed, taking the derivative of each curve in Fig. 3.13 similarly to the smooth-surface case, we obtained the streamwise variation in the spreading angle (α), and compared it to the smooth-surface case in Fig. 3.14. Note that the ribbed surface started at x =

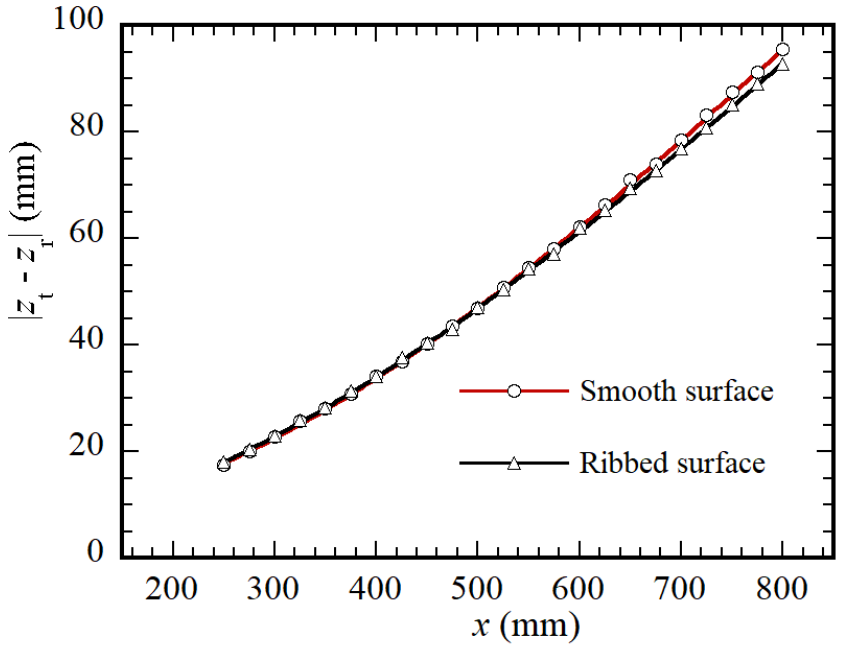

FIGURE 3.13: Comparisons of the lateral growth of turbulent region between the smooth surface and ribbed surface at U_∞ = 11.5 m/s.

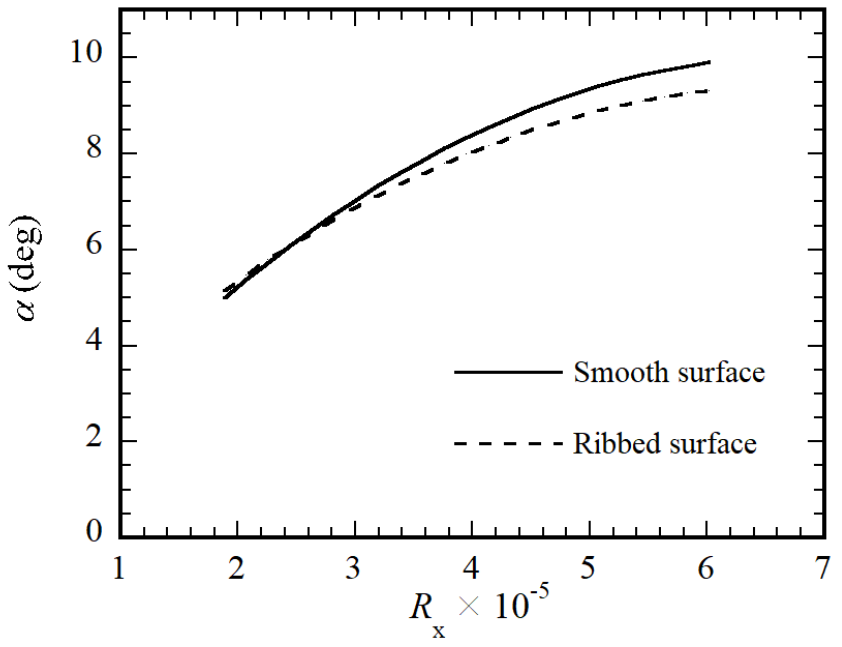

FIGURE 3.14: Comparisons of the lateral spreading angle between the smooth surface and ribbed surface at U_∞ = 11.5 m/s. R_k = 2270.

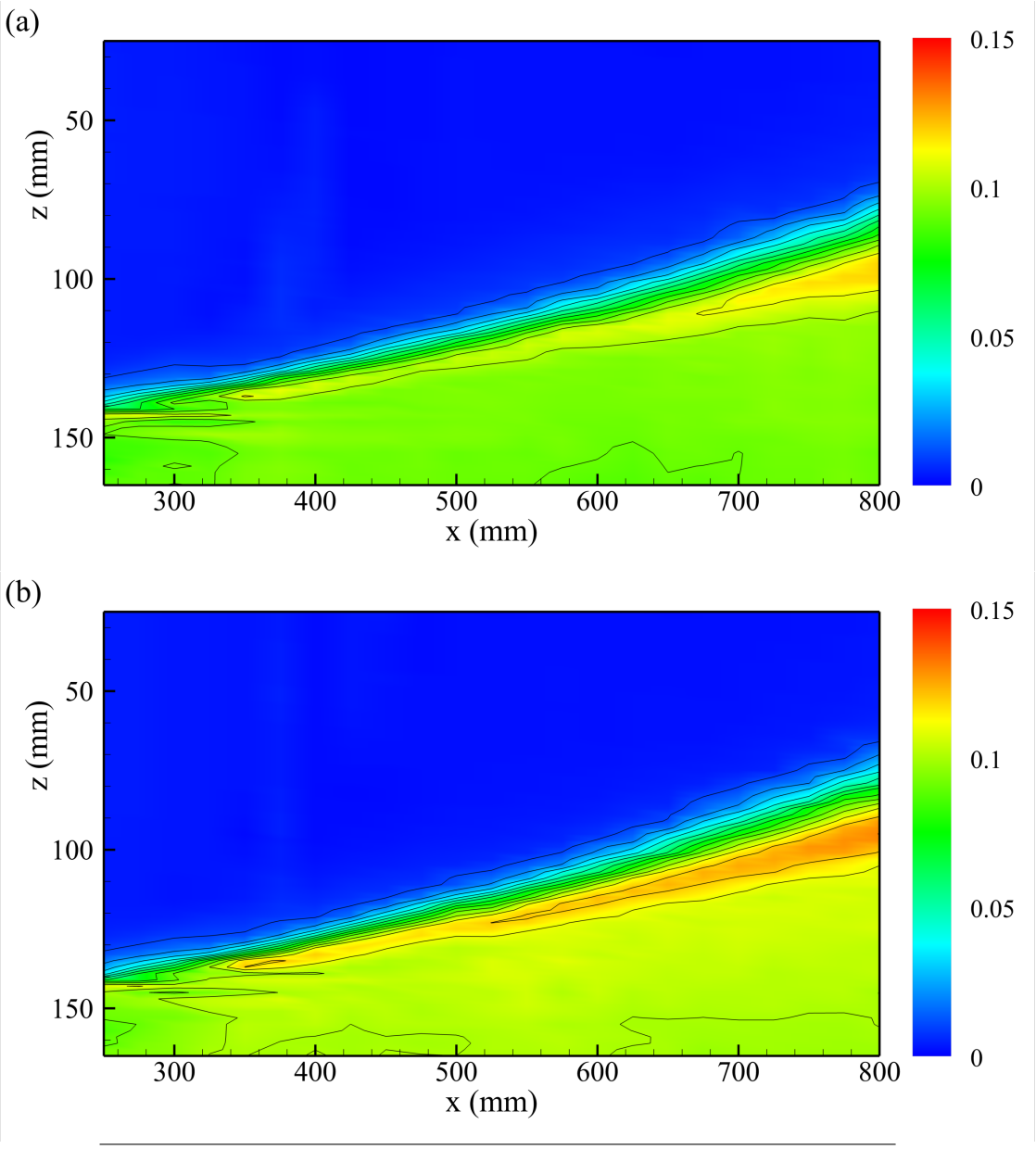

FIGURE 3.15: Contour maps of the rms value u'/U_∞ in the (x, z) plane at y = 0.6 mm at U_∞= 8 m/s for roughness Reynolds number R_k = 790. The interval of contour lines is 0.01. (a) flow over riblets, (b) flow over smooth surface.

300 mm where $R_x = 2.4 \times 10^5$ at U_∞ = 11.5 m/s. The figure shows that the spreading angle over the riblets was slightly smaller than that in the smooth-surface case: the difference in spreading angle was at most 0.6°.

We also compared the spreading angle at U_∞ = 8 m/s. In addition, to see how the riblet effect depended on the roughness Reynolds number R_k, we conducted a similar experiment with a lower roughness Reynolds number at the same free-stream velocity U_∞ = 8 m/s, replacing the 3-mm-height

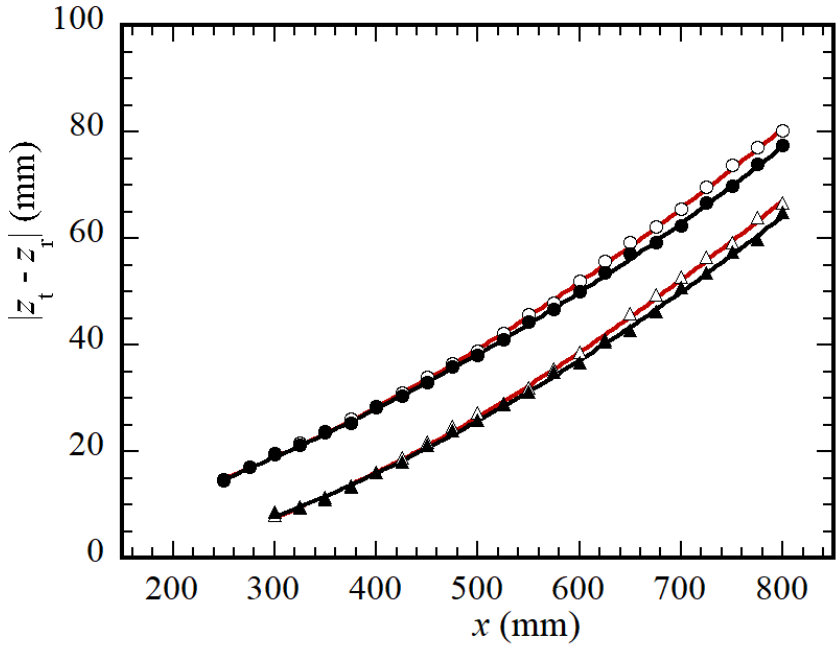

FIGURE 3.16: Comparisons of the lateral growth of turbulent region between the smooth surface (open symbols) and ribbed surface (solid symbols) at U_∞ = 8 m/s for roughness Reynolds number R_k = 790 (△, ▲) and 1580 (○, ●). Solid lines represent approximated curves by third polynomials.

cylinder roughness with 1.5-mm-height cylinder roughness. R_k was 790 and 1580 for k = 1.5 mm and 3 mm, respectively at U_∞ = 8 m/s. Figures 3.15(a) and (b) display contour maps of u' in the (x, z) plane at y = 0.6 mm at U_∞ = 8 m/s for the lower roughness Reynolds number case (R_k = 790), over the riblets and smooth surface, respectively. It is easy to point out that for these cases, the lateral growth did not start immediately downstream of the roughness elements but was delayed more than about 100 mm downstream of the roughness elements. Similar to the results showed for the cases of R_k = 1580 (Fig. 3.7(a) and Fig. 3.12(a)), in the case of lower roughness Reynolds number (R_k = 790) we see no marked difference in the lateral growth of the interface region except slightly weak turbulent intensity over the riblets compared to the smooth surface. In order to show influences of riblets on the lateral contamination more clearly, Fig. 3.16 compares the lateral spreading of turbulent region at U_∞ = 8 m/s, with R_k = 790 and 1580, in terms of the z location (z_t) of the edge of turbulent region. As has been seen in Fig. 3.15(a) and (b), the lateral spreading of turbulent region for the smaller roughness Reynolds number (R_k = 790) was delayed compared to the case of R_k = 1580 (Fig. 3.7(a) and Fig. 3.12(a)) and started beyond x = 350 mm. However, in the downstream

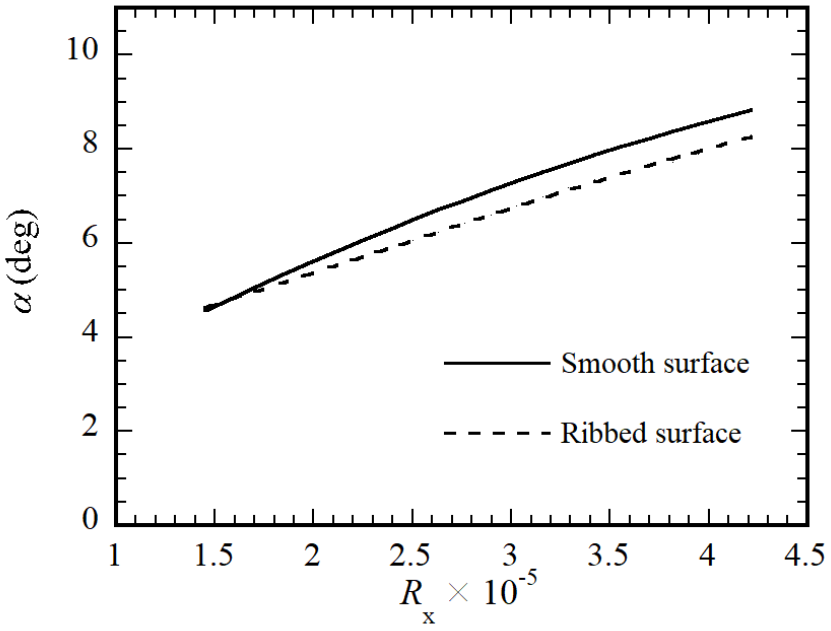

FIGURE 3.17: Comparisons of the lateral spreading angle between the smooth surface and ribbed surface at U_∞ = 8 m/s. R_k = 1580.

region, it seems that lateral spreading occurred with the same spreading angle at both roughness Reynolds numbers. Importantly, in both cases (R_k = 790 and 1580), the riblets could reduce lateral growth of the turbulent region but only slightly, similar to the case of U_∞ = 11.5 m/s (Fig. 3.13).

Figure 3.17 compares the lateral spreading angles (α) over the smooth surface and riblets for R_k = 1580 (at U_∞ = 8 m/s). The reduction in spreading angle by riblets was at most 0.6°. This was also the case for the lower roughness Reynolds number R_k = 790. Thus, the effect of riblets on lateral spreading was not strongly dependent on R_x and R_k, at least for the present experimental conditions. This was different from the case of early development of the turbulent spot observed in the numerical simulation by Strand & Goldstein (2011) [120] where the momentum thickness Reynolds number R_θ was much lower than in the present experiment: note that R_θ was 145 at the roughness location in the numerical simulation, while it was about 180 (at U_∞ = 8 m/s) in the present experiment.

The suppression effect on the turbulence fluctuations in the laminar-turbulent interface region is one possible influence on the lateral turbulent contamination. Figures 3.18(a) and (b) show the magnitudes of velocity fluctuations in

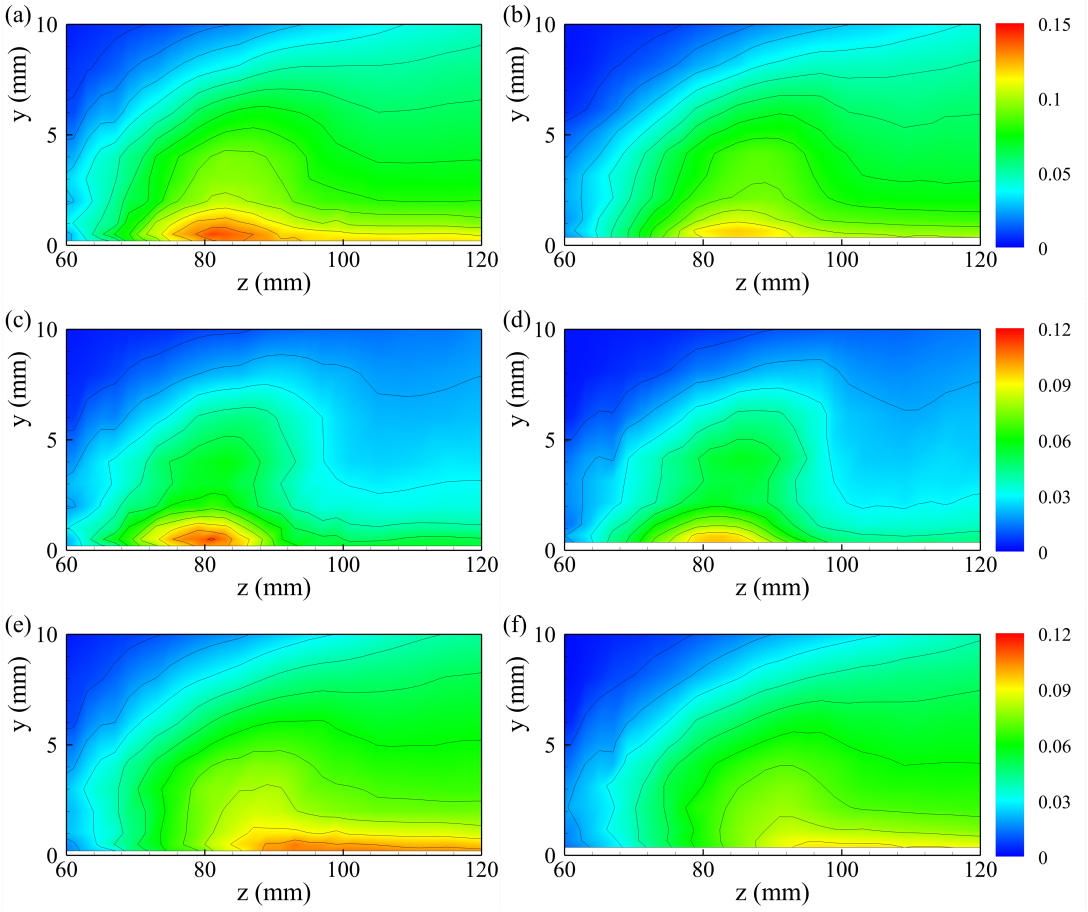

FIGURE 3.18: Contour maps of u'/U_∞ in the (y, z) plane at x = 800 mm, at U_∞ = 8 m/s. (a, c, e) Smooth surface; (b, d, f) riblets. (a, b) u'/U_∞; (c, d) u'_{1-30}/U_∞, (e, f) $u'_{30-2000}/U_\infty$. Interval of contour lines is 0.01.

the laminar-turbulence interface region over the smooth surface and riblets, respectively, in terms of the rms value of streamwise velocity fluctuations u'/U_∞ in the (x, z) plane at x = 800 mm, at U_∞ = 8 m/s. The comparison clearly shows that turbulent intensity (u') was significantly suppressed in the interface region by riblets. We have already seen that a large-scale turbulent packet appeared frequently in the laminar-turbulence interface (intermittently turbulent) region, which no doubt corresponded to occurrence of the largest rms value of velocity fluctuations at and around the intermittent laminar-turbulent interface (see Fig. 3.7 and 3.12). A slight decrease in the lateral spreading angle over the riblets is consistent with the fact that riblets could reduce the intensity of turbulent fluctuations in the intermittent region. In order to show such a riblet effect in more detail, low-frequency spectral components (below 30 Hz) and higher frequency components (30 – 2000 Hz) were extracted by Fourier analyses and their rms values, u'_{1-30} and $u'_{30-2000}$

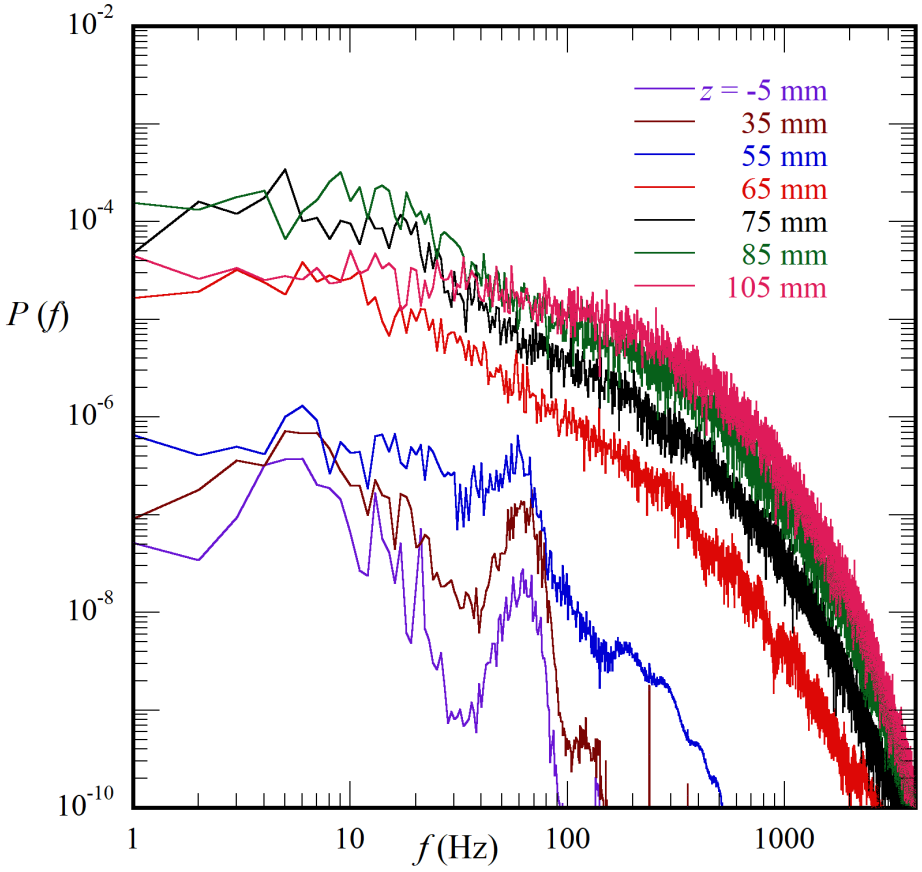

FIGURE 3.19: Power spectra in the laminar-turbulent interface region at (x, y) = (800 mm, 0.6 mm) in the flow over riblets at U_∞ = 8 m/s.

over the smooth surface and riblets are compared in Figs. 3.18(c) to (f). Interestingly, the distributions of u'_{1-30} and $u'_{30-2000}$ separated the intermittent (laminar-turbulent interface) and developed turbulent regions clearly, and both components were reduced by about 10% over the riblets.

Another possible influence is the destabilizing effect of riblets in the laminar region. Figure 3.19 displays power spectra of u-fluctuations near the wall (y = 0.6 mm) in the laminar-turbulent interface region over riblets at x = 800 m/s ($R_x = 4.2 \times 10^5$) at U_∞ = 8 m/s, compared to the spectra for the smooth-wall case (see Fig. 3.9). Inside the turbulent region including the intermittent region ($z \geqslant 65$ mm), we find no essential difference between the smooth surface and riblets. In the laminar boundary layer outside of the turbulent region (i.e., at z = -5, 35, 55 mm), on the other hand, we can see growth of spectral components in a range of 40 – 90 Hz. We extracted the spectral components over 40 – 90 Hz by Fourier analysis, and displayed

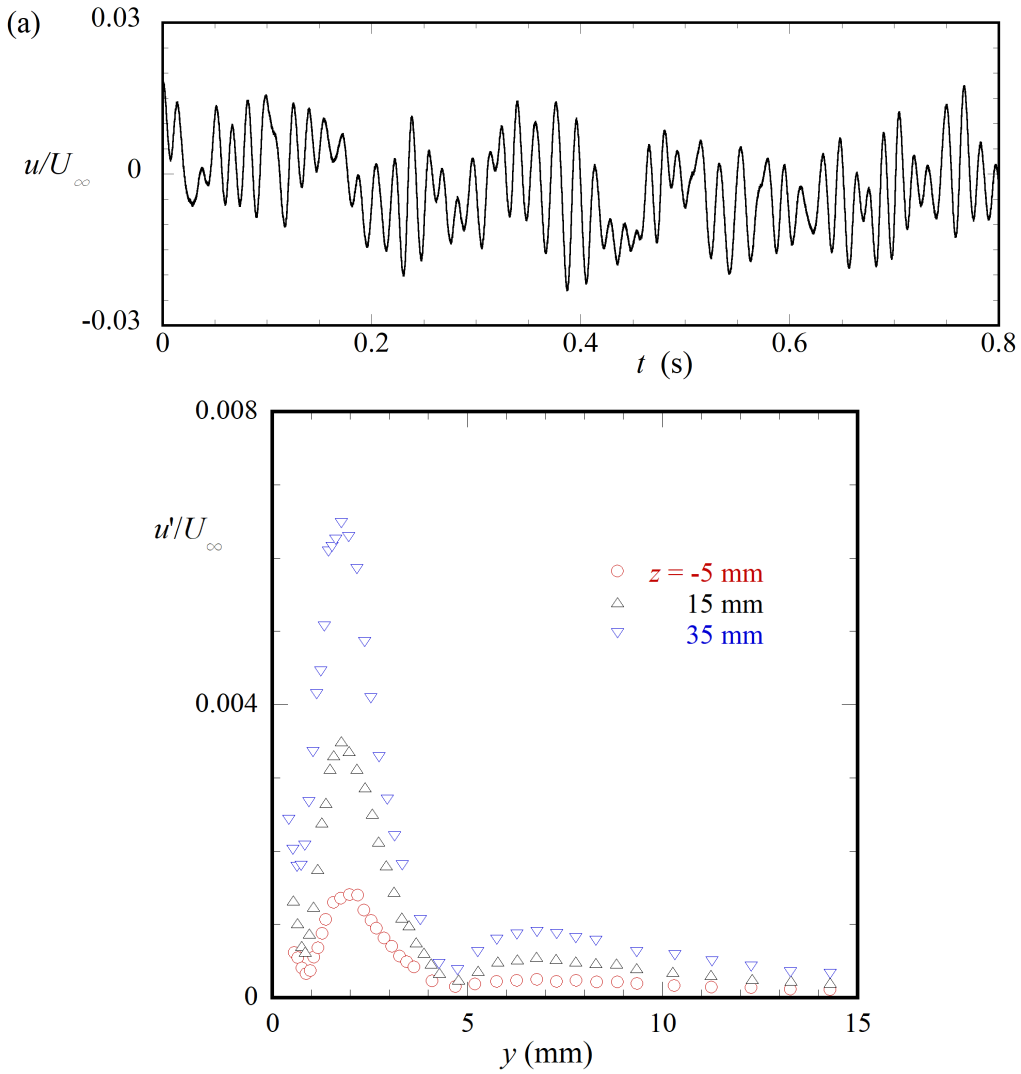

FIGURE 3.20: The waveform and y-distributions of the rms value of spectral component u'_{40-90} at x = 800 mm in the flow over riblets at U_∞ = 8 m/s. (a) Waveform at (x, y, z) = (800 mm, 1.8 mm, 35 mm); (b) amplitude distributions.

the waveform in Figs. 3.20(a). We can see rather sinusoidal waves (with a peak frequency in the spectrum, about 65 Hz), although they were highly modulated in amplitude. The non-dimensional value of the peak frequency (f = 65 Hz), $F = 2\pi f\nu/U_\infty^2 \times 10^6$, was about 90, which was on the upper branch of the neutral stability diagram of the Blasius flow (see Fig. 1.4) at the displacement-thickness Reynolds number $R^* \simeq 1120$ (x = 800 mm). Note that the frequency on the upper branch is $F \sim 100$ at $R^* \sim 1120$. In order to identify the wave observed, Figs. 3.20(b) illustrates the y-distributions of the rms value of spectral components (f = 40 -– 90 Hz), u'_{40-90} at z = 35, 15 and -5 mm at x = 800 mm in the laminar region adjacent to the interface. The maximum amplitude (y-maximum) decreased monotonously with the

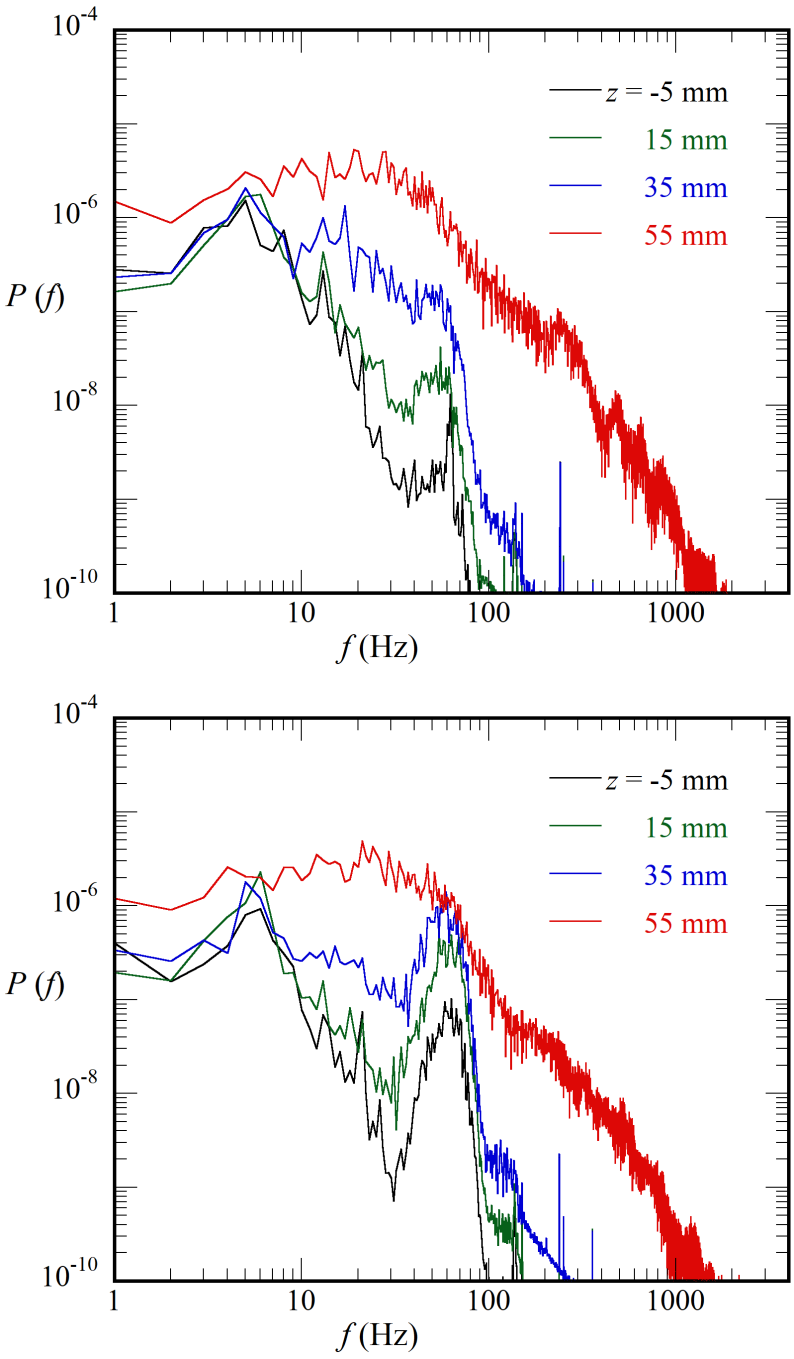

FIGURE 3.21: Power spectra in the laminar region at (x, y) = (800 mm, 2 mm) over (a) smooth surface and (b) riblets, at U_∞ = 8 m/s.

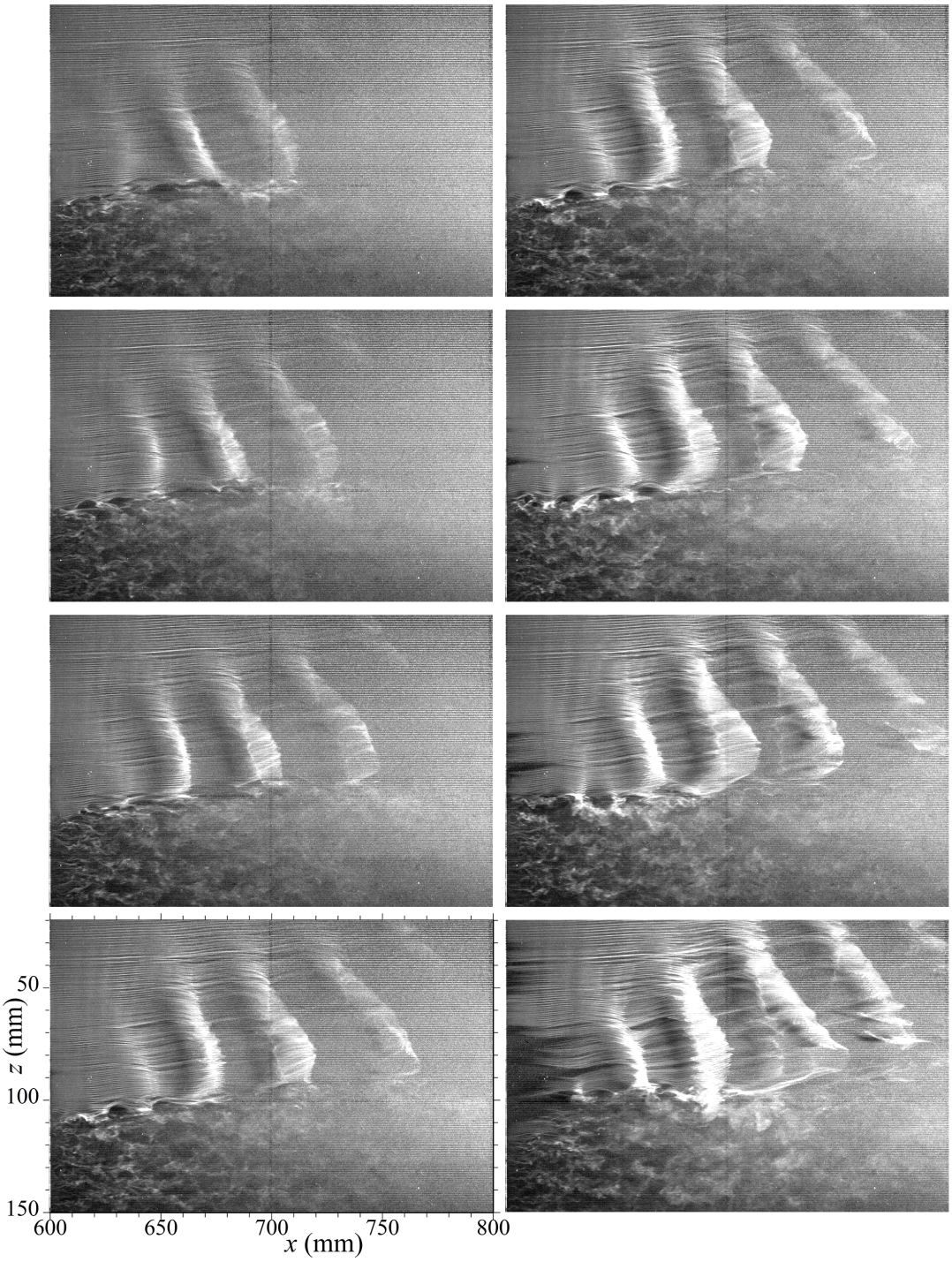

FIGURE 3.22: Smoke-wire visualization of the flow over riblets at U_∞ = 8 m/s. A smoke-wire was stretched at a height of $y \approx$ 1 mm. Time increases from top to bottom, and left to right with interval of 5 ms.

increase in the distance from the edge of the turbulent region; the maximum values of u'_{40-90} were about 0.60%, 0.33% and 0.14% of U_∞ at z = 35, 15 and -5 mm, respectively, strongly suggesting that these waves were excited in the interface region. Furthermore, the amplitude distribution took a maximum at a y-position slightly away from the surface, compared to the amplitude distribution of two-dimensional T-S wave, suggesting that these waves were of oblique type.

On the other hand, in the smooth surface, instability waves were not recognized in the spectra given in Fig. 3.9. However, since the measurement was conducted at y = 0.6 mm, the amplitude of the instability waves, if they occurred, might be very small. We therefore examined the wave development in the interface and laminar regions over the smooth surface more carefully. Figures 3.21(a) and (b) display the power spectra measured at y = 2 mm, around which the amplitude of the oblique wave took a maximum (see Fig. 3.20(b)) over both the smooth surface and riblets. Comparing the spectral components over 40 – 90 Hz in both cases, the magnitude was one order of magnitude smaller than over the riblets; that is, in terms of the rms value u'_{40-90}, the wave amplitude over the smooth surface was less than one-third that over the riblets.

To clarify the wave development more distinctly, we conducted flow visualization in the interface region by means of the smoke-wire technique. Figure 3.22 displays a sequence of visualization pictures of the near-wall flow around the laminar-turbulent interface. Here a smoke-wire was stretched parallel to the wall at (x, y) = (600 mm, 1 mm), and high-speed video pictures covered the streamwise distance of x = 600 – 800 mm. Consecutive smoke pictures show that oblique waves with a small oblique angle ($\sim 20^\circ$) could develop along the edge of the turbulent region. The oblique waves had a wavelength of about 34 mm and propagated downstream at $0.25U_\infty$. Thus, the frequency was estimated to be about 60 Hz, which corresponded to that of the spectral peak in Fig. 3.19 and 3.21(b). Importantly, the rms amplitude of these waves (u'_{40-90}) was below 1% of U_∞ as shown in Fig. 3.20 so that these waves could not undergo rapid growth due to the secondary instability (Herbert, 1988 [128]). We infer that lateral contamination caused by turbulent vortices in the interface region would precede faster than growth of oblique waves excited by turbulent fluctuations in the interface region, even if they could grow downstream. Therefore, the oblique waves excited could not directly contribute to the lateral contamination.

3.5 Conclusions

Influences of streamwise riblets on the lateral growth of turbulent region generated locally in span were examined experimentally in a zero-pressure-gradient boundary layer. Two rows of circular cylinders, the order of the boundary layer thickness high, were glued over a short span of the boundary layer plate at an upstream location to generate strong disturbance leading to transition to turbulence just behind the cylinder roughness. The possible influences of riblets on each of the laminar and turbulent boundary layers were considered; that is, we considered the destabilizing effect on the laminar region and suppression effect on the near-wall turbulence in the interface region between the laminar and turbulent regions. The x-Reynolds number (R_x) in the experiment was up to 6×10^5 where the momentum-thickness Reynolds number (R_θ) was about 1300 in the laminar boundary layer outside the turbulent region.

Riblets in this experiment had triangular ridges with a ridge angle of 30° and trapezoidal valleys, with a height-to-width ratio of 0.5. The cross-section geometry was a typical one used in engineering applications for turbulent drag reduction. The values of riblet-ridge spacing (or ridge height) were 20 and 28 (or 10 and 14) in wall units using the friction velocity in the developed turbulent region. Those were close to the optimal riblet size and the upper limit of the drag-reducing size, respectively, and thus the present riblets could be expected to appreciably reduce the activity of near-wall turbulence. In the laminar region where riblet height is important from the instability viewpoint, the riblet height (h) was at most half the displacement thickness (δ^*) of the laminar boundary layer. According to the stability experiment (Ho & Asai, 2018 [122]), the application of riblets with this height and spacing could be expected to markedly enhance boundary-layer instability.

The lateral spreading angle was compared at sufficiently large roughness Reynolds numbers (R_k = 1580 and 2270), where turbulent contamination began at the roughness location. The spreading angle of the turbulent region increased with R_x and tended to a value slightly larger than 10° for $R_x > 6 \times 10^5$ over the smooth surface, which was very close to the value observed in past experiments and numerical simulations of a turbulent wedge/spot. When the riblets were applied, the intensity of near-wall turbulence was reduced by about 10% in terms of u' in the laminar-turbulent

interface region, and a corresponding decrease was found in the spreading angle compared to the smooth surface. The lateral spreading angle at $R_x = 6 \times 10^5$ was about 10° over the smooth surface and about 9.4° over the riblets. The reduction in the lateral spreading angle, with almost the same reduction rate, was also confirmed in the lower-Reynolds-number experiment ($R_x = 2 - 4 \times 10^5$). Furthermore, we compared lateral spreading for a smaller roughness Reynolds number (R_k = 790) with the same laminar boundary layer condition, and confirmed that there was no distinct difference in the effect of riblets on the lateral spreading angle between R_k = 790 and 1580, despite the fact that the lateral growth started at a location some distance downstream from the roughness elements for the lower roughness Reynolds number R_k = 790.

In the laminar-turbulence interface region, in addition to successive occurrence of low-speed streaks (which generally dominated the initial stage of lateral growth of the turbulent wedge), a large-scale packet of turbulent eddies followed by many low-speed streaks was frequently observed in the downstream developed stage in the interface region. The occurrence of such a large-scale turbulent structure in the interface region became more appreciable which was recognized by increase in the intensity of turbulent fluctuations (mainly consisting of low-frequency spectral components) in the interface region, and could no doubt contribute to the lateral turbulent contamination. We speculate that when the turbulent wedge developed sufficiently in the downstream, the flow (with the velocity shear $\partial U/\partial z$) in the laminar-turbulent interface might undergo inflectional instability just like as in a turbulent mixing layer. Further investigations are necessary on the occurrence and growth of large-scale turbulent structure in the laminar-turbulence interface.

As for the destabilizing effect of streamwise riblets on the laminar boundary layer outside the turbulent region, development of oblique waves (with a small oblique angle) whose frequency was very close to the most amplified T-S waves was observed distinctly in the laminar region near the edge of the intermittent turbulent region over the riblets. In the smooth-surface case, such waves were much smaller in amplitude than those over the riblets. The wave amplitude was largest adjacent to the interface region, and decreased monotonously with spanwise distance from the edge of the turbulent region. Thus, it was reasonable to consider that the oblique waves were excited by

turbulence structures in the interface region. Importantly, however, the magnitude of the oblique waves remained small (less than 1% in terms of u'/U_∞) even in the more unstable flow over the riblets. Thus we may say that such oblique waves did not directly contribute to the lateral turbulent contamination.

Chapter 4

Dependence of streak breakdown on disturbance nature

4.1 Introduction

The laminar-to-turbulent transition in boundary layers is caused by a sequence of flow instabilities. These instability process are strongly influenced by the intensity and scales of freestream turbulence (vortical disturbances) and/or other disturbances such as acoustic disturbances even for the same flow geometry. Such external disturbances can excite the linear instability waves known as Tollmien-Schlichting (T-S) waves through a receptivity process in the leading-edge region while vortical disturbances in the freestream do not excite T-S waves but also penetrate into the boundary layer and cause low-speed streaks to develop by a transient growth mechanism [46–49]. In a zero-pressure-gradient boundary layer subjected to high-intensity freestream disturbances, the transition process can skip the amplification stage of T-S waves, and begin the transient growth of low-speed streaks. They subsequently undergo a secondary instability leading to streak breakdown into energetic coherent vortices such as a train of quasi-streamwise vortices with alternative sign of vorticity and/or hairpin-shaped vortices [53, 61, 129–132]. This is a prerequisite for the generation of wall turbulence. Streak instability and breakdown into quasi-streamwise vortices also play an important role in the regeneration cycle of wall turbulence at least at low Reynolds numbers [75–78]. The present study focuses on the streak instability and breakdown caused by disturbances with a spectrum of turbulent fluctuations.

In experiments of bypass boundary-layer transition subjected to freestream

turbulence, the turbulence level in the freestream has often been controlled by a turbulence grid installed upstream of the boundary-layer plate [45, 57–59]. Matsubara & Alfredsson [45] introduced freestream disturbances whose turbulence level Tu was 1.5%, 2.2% or 6.6% in terms of the rms value of streamwise velocity fluctuations at the leading edge location. They observed that some of the low-speed streaks that developed underwent localized oscillatory motions leading to turbulent spots, depending on the turbulence level. Fransson *et al.* [59] also studied boundary-layer transition under the similar turbulence levels using active turbulence-generating grids and showed that the transitional Reynolds number was inversely proportional to Tu. Man *et al.* [57, 58] visualized the bypass transition process under high freestream turbulence in detail, and clarified that the breakdown of low-speed streaks was caused by sinuous secondary instability, although they sometimes observed local occurrence of varicose instability at very high freestream turbulence (Tu = 6.7%) [57]. Mandal & Dey [133] examined a boundary layer transition induced by the wake of a circular cylinder in the freestream. Their results showed that wake-induced transition was essentially similar to that in the bypass transition under freestream turbulence.

In numerical simulations of bypass boundary-layer transition under freestream turbulence, disturbances were supplied as an inflow perturbation, *i.e.*, using a superposition of continuous-spectral modes of the linearized Orr-Sommerfeld and Squire equations [62, 65]. Brandt *et al.* [62] conducted computations that varied energy spectrum of input disturbances with turbulence intensity of 1.7 – 4.7% and showed that an increase in the integral length scale of simulated freestream turbulence caused earlier transition. Andersson *et al.* [130] performed secondary instability analyses of optimal low-speed streaks and obtained a critical streak amplitude (defined as the velocity difference across each low-speed streak) of about 26% of freestream velocity. Zaki & Durbin [134], focusing on the interaction between two freestream vortical modes, showed clearly that the low-frequency component of freestream disturbance plays a role in the transient growth of low-speed streaks while the high-frequency component contributes to streak breakdown. For details on the direct numerical simulations of the bypass transition under freestream turbulence and stability analyses of the secondary instability, see the reviews by Schlatter *et al.* [63] and [64].

On the other hand, Asai *et al.* [54–56] conducted experiments using well-controlled low-speed streak(s) to visualize the detailed process of streak instability and breakdown. Their experiments included the sinuous and varicose instabilities of a single low-speed streak [54], and the fundamental and subharmonic instabilities in spanwise-periodic low-speed streaks [55, 56]. In these experiments, the low-speed streak(s) were generated artificially in a laminar boundary layer using a small piece/pieces of screen set normal to the boundary-layer plate, and the breakdown process of low-speed streak(s) was triggered by well-controlled sinusoidal disturbances with mono-frequency. Results showed that sinuous instability could continue to grow downstream and lead to breakdown into quasi-streamwise vortices not unlike those observed in near-wall turbulence. Furthermore, Asai *et al.* [105] examined transient growth and subsequent breakdown of low-speed streaks in a re-transition caused by suction-surviving residual turbulent fluctuations. In their experiment, sinuous instability waves with rather selective wavelengths (close to that of the most unstable linear instability mode [78]) developed before streak breakdown, despite the disturbances exciting the streak instability being initially frequency-rich.

In the present study, we aimed to gain further insights into the instability and breakdown of low-speed streak(s) in natural or turbulent environments experimentally. A screen-generated low-speed streak was forced by disturbances with a continuous spectrum similar to that of developed wall turbulence. We describe how initial disturbances with a frequency spectrum similar to that of wall turbulence, but with various spanwise coherences, were introduced to excite streak instability. We focused particularly on the dependence of breakdown process caused by sinuous instability on the nature of the disturbances triggering the instability. Through this experiment, we also sought to recognize characteristic features of velocity fluctuations in near-wall turbulence from the viewpoint of streak instability.

4.2 Experimental setup and procedure

The experiment was conducted in a low-turbulence wind tunnel with an exit cross-section of 400×400 mm^2. As illustrated in Fig. 4.1, a boundary-layer plate, which was 10 mm thick and 1100 mm long, was set parallel to the oncoming uniform flow in the test section. This setup was the same as that used

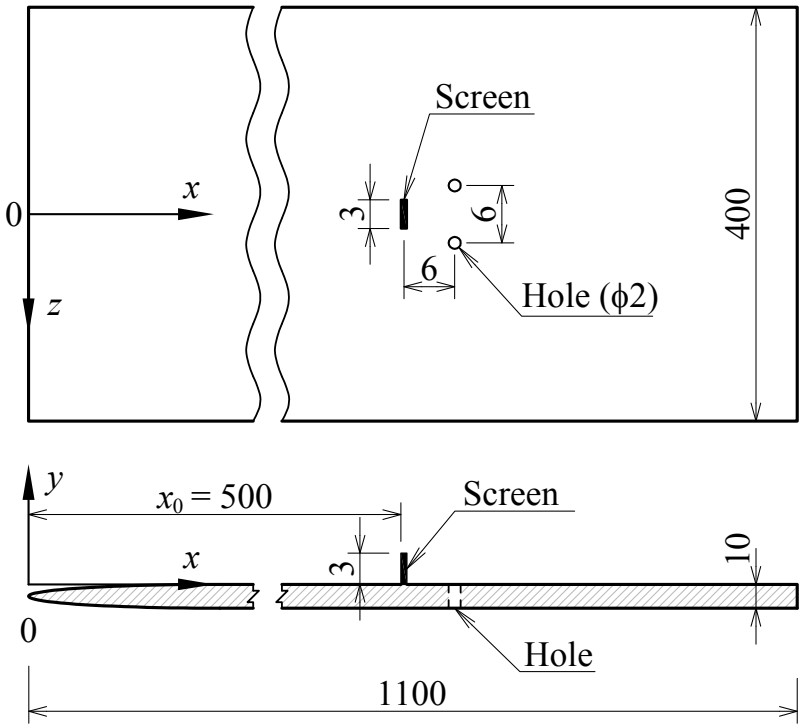

FIGURE 4.1: Schematic of boundary-layer plate (dimensions in mm, not in scale).

in the experiment by Asai *et al.* [54]. The freestream velocity U_∞ was fixed at 4 m/s throughout the experiment, while the freestream turbulence was less than 0.1% at the leading-edge location. A single low-speed streak was produced in a boundary layer using a small piece of 40-mesh screen (wire-gauze) set normal to the boundary-layer plate at a station 500 mm downstream of the leading edge; the porosity of the screen was 0.7. Screen height and width were both 3 mm. Note that the displacement thickness δ^* of the Blasius boundary layer was about 2.5 mm at the screen location in the absence of the screen. The coordinate system was such that x was the streamwise distance, measured from the leading edge, y the normal-to-wall distance and z the spanwise distance. The screen location (x = 500 mm) is denoted by x_0.

A constant-temperature hot-wire anemometer was used to measure time-mean and fluctuation velocities in the streamwise direction, U and u. The hot-wire probe (a tungsten wire 5 μm in diameter) had a sensitive length of 1 mm. A fourth-order polynomial curve was used for the hot-wire calibration. Room temperature was kept almost constant at 18°C with a temperature variation within $\pm$0.5°C during the experiment. Hot-wire signals were low-pass-filtered with a cutoff frequency of 5 kHz and then stored in a PC through

a 16-bit analog-to-digital converter with a sampling frequency of 10 kHz. In addition, flow visualization was conducted by a smoke-wire technique to visualize the development of streak instability and eventual breakdown. A smoke-wire was stretched in the spanwise direction, and time sequences of top-view pictures were taken with a digital high-speed video camera system.

The laminar streak flow was forced by external disturbances with the same frequency-spectrum as the velocity fluctuations of developed wall turbulence. They were introduced through two small holes drilled into the wall symmetrically with respect to the mid-span of the low-speed streak, 6 mm downstream of the screen, with a spanwise distance of 6 mm. The holes were connected to two loudspeakers by vinyl hoses. The turbulent signals used here were obtained by two hot-wires in the buffer region of a turbulent boundary layer generated in the same freestream condition. By changing the spanwise distance of the two hot-wire sensors Δz, we could obtain various pairs of turbulent-fluctuation signals with the same frequency-spectrum but different spanwise coherencies. The minimum distance between the two hot-wire sensors was 1.8 mm, which corresponded to 24 in wall units for the turbulent boundary layer at U_∞ = 4 m/s. Details on the input disturbances are described in the next section.

4.3 Base flow and disturbance conditions

First we would like to explain the screen-generated low-speed streak and disturbances that triggered streak instability in the present experiment. Figs. 4.2(a)–(d) illustrate distributions of the mean velocity U in the (y, z) plane at $x - x_0$ = 60, 100, 140 and 180 mm, respectively. The screen caused a velocity defect but did not give rise to a reversed flow behind it. The velocity difference across the low-speed streak ΔU (measured for z-distributions of U at y = 3.5 – 4.0 mm) was about 40%, 35%, 31% and 29% of U_∞, at $x - x_0$ = 60, 100, 140 and 180 mm, respectively. The velocity difference ΔU was larger than the critical value (about 27% of U_∞)for the growth of sinuous instability modes even at $x - x_0$ = 180 mm, according to the result by Andersson *et al.* [130]. Thus, a distinct streamwise low-speed streak developed downstream of the screen and maintained a sufficiently large ΔU far downstream. The width of the low-speed streak (the half width of the z distribution of U) was almost the same as the screen width (3 mm) at least up to $x - x_0$ = 180 mm. The

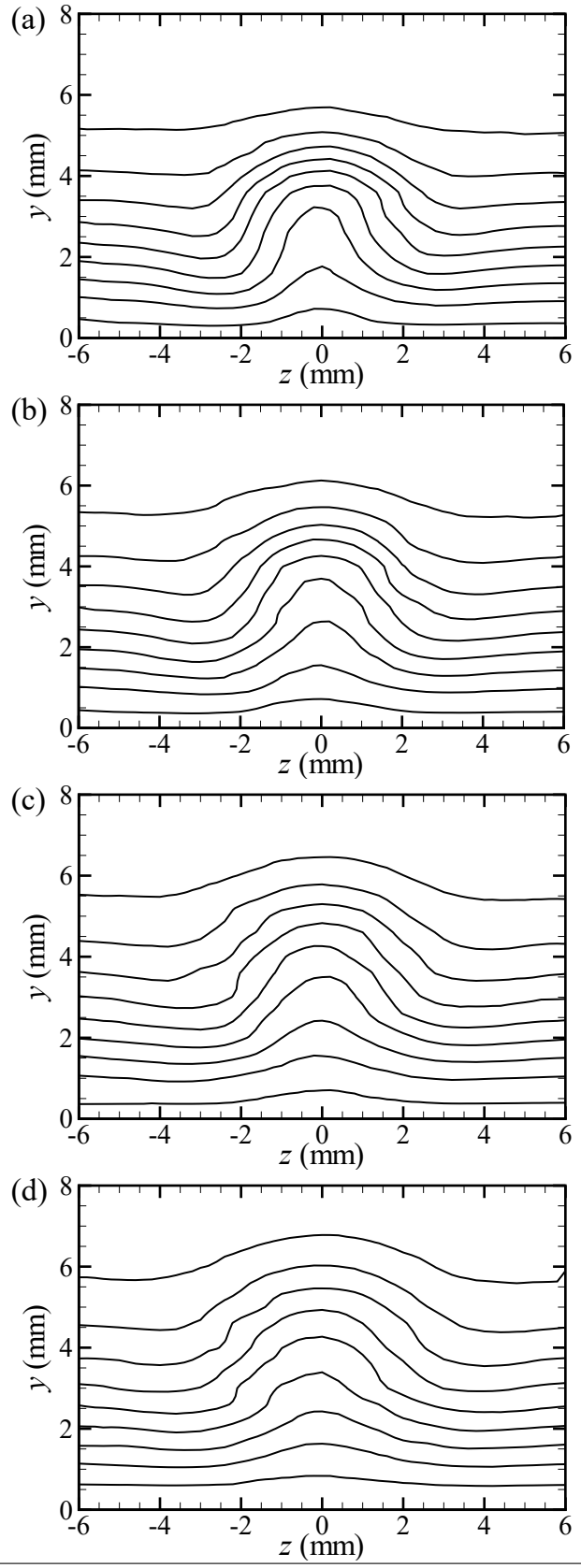

FIGURE 4.2: Distributions of U/U_∞ in the (y, z) plane. (a) $x - x_0$ = 60 mm, (b) 100 mm, (c) 140 mm and (d) 180 mm. Contour levels range from 0.1 to 0.9.

TABLE 4.1: Disturbance conditions.

	y^+	Δz^+	C_t (30–120 Hz)	C_t (5–2000 Hz)
Case 1	23	24	0.353	0.469
Case 2	23	49	-0.104	0.019
Case 3	23	77	-0.106	-0.097
Case 4	23	94	-0.067	-0.098
Case 5	23	149	-0.011	-0.053
Case 6	23	—	-1.0	-1.0
Case 7	23	—	1.0	1.0
Case 8	40	24	0.561	0.593
Case 9	40	49	0.016	0.144
Case 10	40	94	-0.097	-0.085
Case 11	40	—	-1.0	-1.0
Case 12	40	—	1.0	1.0

velocity distribution for $|z| > 5$ mm was close to the Blasius profile. The rms value of the u-fluctuation, u' increased downstream but the maximum value of u' was only about 0.5% at $x - x_0$ = 180 mm. In the absence of artificial disturbances, we confirmed that the low-speed streak maintained a laminar flow in the observation region up to $x - x_0$ = 250 mm.

In order to excite instability of the laminar low-speed streak, a pair of forcing signals was supplied to the two loudspeakers, by which normal-to-wall velocity fluctuations were induced by sucking/blowing air through the holes behind the screen. The input signals to the loudspeakers were produced from waveforms of turbulent velocity fluctuations deduced from a turbulent boundary layer. Here, the turbulent boundary layer was produced by gluing cylinder-roughness-elements onto the boundary layer plate at an upstream location, x = 100 mm, under the same freestream velocity U_∞ = 4 m/s. The cylinder diameter and height were 3 mm and 10 mm, respectively, and they were arranged in a two-row configuration. In each spanwise row, the cylinder spacing was 10 mm, and the two rows (separated by 10 mm in the streamwise direction) were staggered by 5 mm in the spanwise direction. The height of cylinder-roughness was three times larger than the boundary-layer thickness in the absence of roughness (about 3 mm at x = 100 mm), and a turbulent boundary layer with about 45-mm-thickness developed 800 mm downstream of the cylinder-roughness (x = 900 mm), where the momentum thickness Reynolds number was about 1090 and the friction Reynolds number (Re_τ) based on the friction velocity u_τ and the boundary-layer thickness was about 530. Using two hot-wires, we acquired a pair of turbulent fluctuation signals at two z-positions with distance Δz at x = 900 mm. We chose

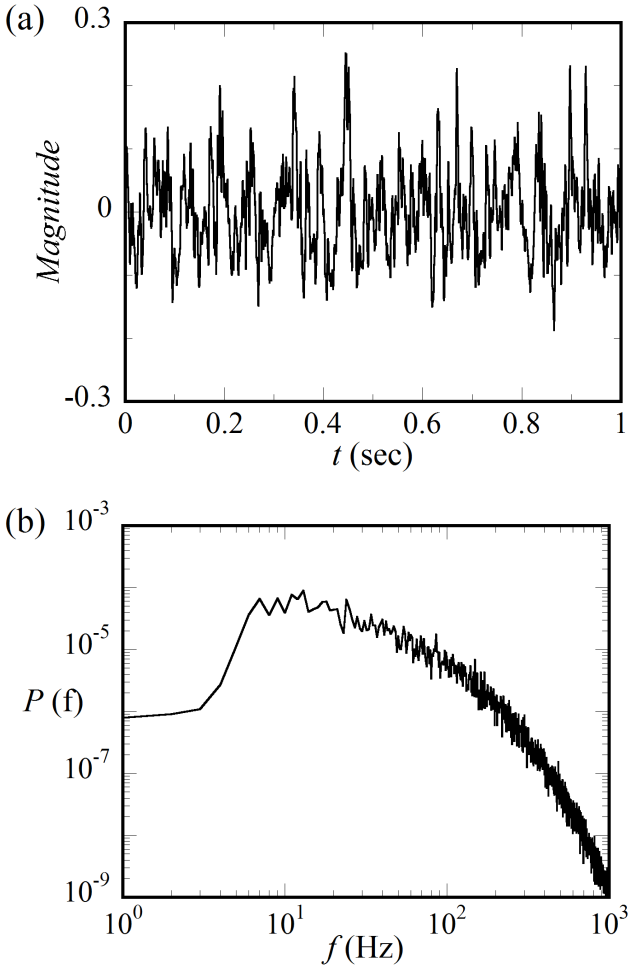

FIGURE 4.3: Waveform and power spectrum of turbulent signals supplied to the two loudspeakers (Case 1 – 7: Turbulent signals were obtained at $y^+ = 23$).

several cases for the spanwise distance Δz, in the range of 24 – 149 in terms of the wall unit Δz^+ (= $\Delta z u_\tau / \nu$), for two y positions in the buffer region, y^+ (= $y u_\tau / \nu$) = 23 and 40.

Figs. 4.3(a) and (b) display waveform and spectra of the turbulent signal supplied to the two loudspeakers for Cases 1 – 7. The spectrum exhibited the f^{-1} region over 20 – 100 Hz. Here, spectral components below 5 Hz were filtered out for the input signals to the loudspeakers. Pairs of turbulent signals had various coherencies as shown in Table 4.1. For turbulence data measured at $y^+ = 23$, the correlation coefficients (C_t) calculated for a pair of fluctuation signals over 30 – 120 Hz which was the frequency-range of growing disturbances for streak instability (as shown later) were about 0.353, -0.104, -0.106, -0.067 and -0.011 for Δz^+ = 24 (Case 1), 49 (Case 2), 77 (Case 3), 94 (Case 4) and 149 (Case 5), respectively. These values of Δz^+ ranged across

the mean streak spacing at y^+ = 23; according to Smith & Metzler [135], the mean streak spacing in wall turbulence is about 100, 120, 150 for y^+ = 5, 20 and 30, respectively. Here, the correlation coefficient C_t is defined as:

$$C_t = \frac{\overline{u_A u_B}}{\sqrt{\overline{(u_A)^2}}\sqrt{\overline{(u_B)^2}}} \tag{4.1}$$

where u_A and u_B are the two input turbulent-signals to the loudspeakers and the overlines denote time-averaging. For turbulence data measured at $y^+ = 40$ (Cases 8, 9 and 10), the correlation coefficients (C_t) were slightly different from those for the corresponding Δz^+ data at $y^+ = 23$ (Cases 1, 2 and 4) since the streak spacing in wall turbulence gradually increased with y^+ (see also [135]). We also considered two other cases. One was anti-symmetric forcing (Cases 6 and 11) in which two loudspeakers were driven with turbulent signals that were 180° out of phase and the other was symmetric forcing (Cases 7 and 12) in which two loudspeakers were driven with in-phase turbulent signal. Of course, we expected that the anti-symmetric forcing ($C_t = -1$) would be the most effective for excitation of sinuous instability modes, while the symmetric forcing would not excite sinuous instability but varicose instability only. The results were compared to the cases listed in Table 4.1. Spectra of streamwise velocity fluctuations excited with these signals (measured at just downstream of the holes) were found to be not so different from the spectrum of the input signals, as will be shown later.

4.4 Dependence of streak instability and breakdown on the disturbance condition

Before investigating the frequency-selective growth of disturbances excited by turbulent spectral components, we obtained the instability characteristics of the present low-speed streak by driving the loudspeakers at a single frequency. Symmetric and anti-symmetric forcing (using the two loudspeakers) easily excited the varicose and sinuous instability modes. Figs. 4.4(a) and (b) illustrate the amplitude distributions of the streamwise velocity fluctuation u (of the forcing frequency) in the (y, z) plane for varicose and sinuous modes, respectively; they were excited at 110 Hz and 90 Hz which were the frequencies of the most amplified sinuous and varicose modes, respectively.

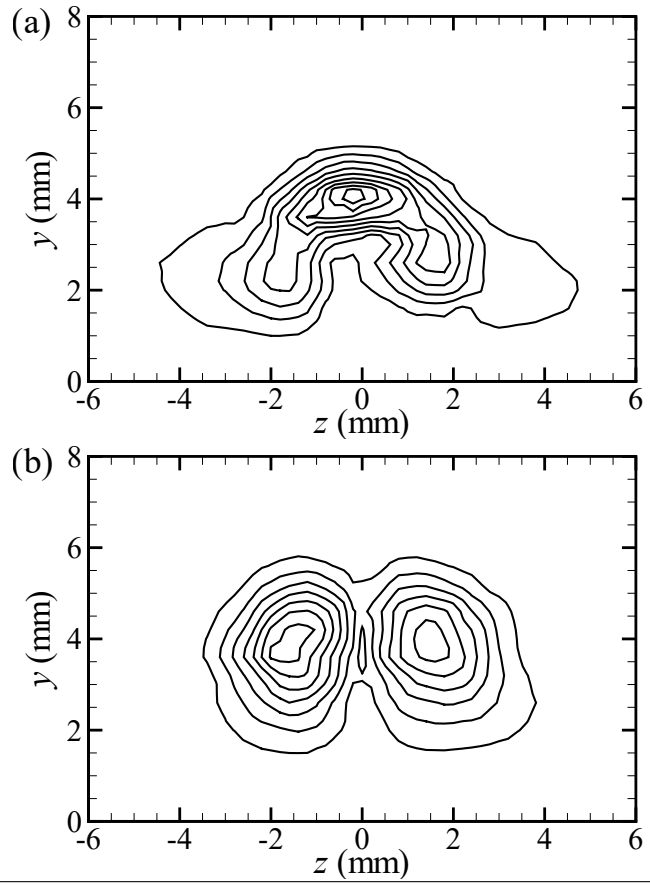

FIGURE 4.4: Distributions of u'/U_∞ in the (y, z) plane. (a) Varicose mode of $f = 110$ Hz at $x - x_0 = 50$ mm. Contour levels range from 0.002 to 0.018. (b) Sinuous mode of $f = 90$ Hz at $x - x_0 = 100$ mm. Contour levels range from 0.005 to 0.035.

The u component of the varicose mode took the maximum amplitude at the mid-span of the horizontal high-shear layer (at the inflection point in the y-distribution of U at $z = 0$), while the u component of the sinuous mode took two maxima in the right and left vertical shear layers at $z = \pm 1.5$ mm (the inflection points in the z-distribution of U).

Fig. 4.5(a) displays the streamwise development of both the modes in terms of the maximum rms amplitude u'_m. The symmetric, varicose mode could not continue to grow downstream beyond $x - x_0 = 60$ mm in the present low-speed streak, because the span width of the horizontal shear layer ($\partial U/\partial y$) away from the wall in the low-speed streak was small compared to the shear-layer thickness (see Fig. 4.2) due to thickening of the $\partial U/\partial y$-shear by viscous diffusion. In contrast, the anti-symmetric, sinuous mode continued to grow downstream with almost constant growth rate for $x - x_0 \geq 60$ mm until it reached a nonlinear saturation stage (beyond $x - x_0 = 180$ mm). Fig. 4.5(b)

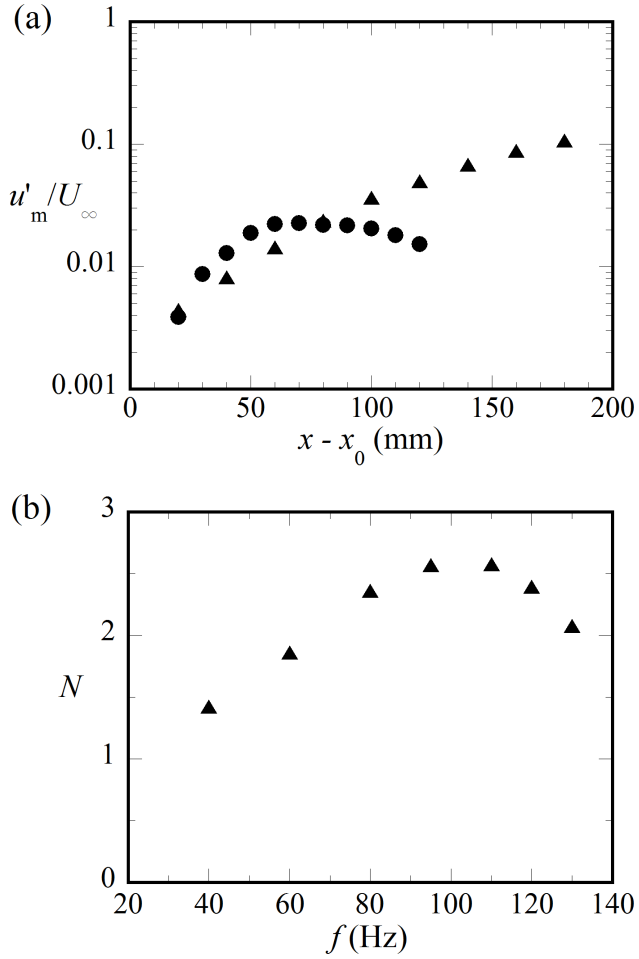

FIGURE 4.5: Instability characteristics of low-speed streak. (a) Streamwise growth of sinuous mode ($f = 90$ Hz, ▲) and varicose mode ($f = 110$ Hz, •). (b) Amplification of sinuous mode from $x - x_0 = 40$ mm to 180 mm. N versus f.

illustrates the frequency selective growth of sinuous disturbances in terms of N-value defined as $N = \ln[u'_m(x_2)/u'_m(x_1)]$, where $u'_m(x_1)$ and $u'_m(x_2)$ were the maximum rms value of the u-fluctuation component (at the forcing frequency) at $x - x_0$ = 40 mm, and 180 mm, respectively. Note that the sinuous mode has already completed its structure at $x - x_0$ = 40 mm. The maximum amplification of the sinuous mode occurred at and around 100 Hz in the present streak flow condition.

We then examined responses of the low-speed streak to disturbances with the turbulence spectrum mentioned above. Figs. 4.6(a) and (b) illustrate power spectra of u at $x - x_0$ = 10, 60, 100, 140 and 180 mm for Cases 1 and 2, respectively; they were measured at a vertical shear-layer ($\partial U/\partial z$) position where the disturbance took a maximum in amplitude at each x station. At

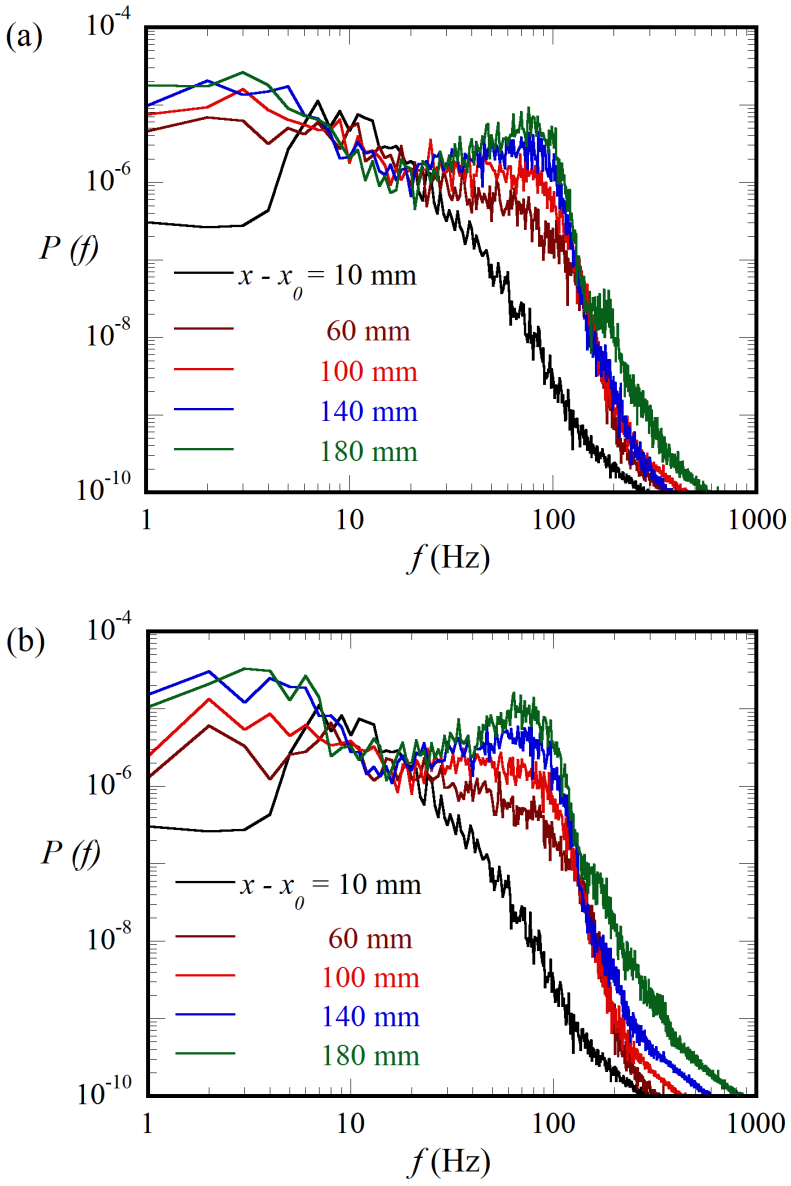

FIGURE 4.6: Power spectra of u at $x - x_0$ = 10 mm, 60 mm, 100 mm, 140 mm and 180 mm. (a) Case 1, (b) Case 2.

$x - x_0$ = 10 mm, immediately downstream of the screen, the spectra were similar to those of the input signals to the loudspeakers, and the rms value of u-fluctuations were calculated from the spectra to be about 1.3% of U_∞ in both cases. In the downstream locations, the figures show that disturbances underwent an intensive growth over a frequency range of 30 – 120 Hz in both cases, irrespective of the difference in the spanwise coherence of the initial disturbance. The peak frequency in the spectral growth was 70 – 80 Hz in both cases, which was slightly lower than the frequency of the most amplified sinuous mode given in Fig. 4.5(b). This is due to the fact that the spectrum component of the initial disturbance (Fig. 4.3b) decreased in proportion to

f^{-1} over 20 – 100 Hz. In addition, a close comparison of the magnitude of the spectral peak shows that disturbance growth is larger in Case 2 than in Case 1, indicating that the disturbance development was clearly dependent on the coherence of the initial disturbance.

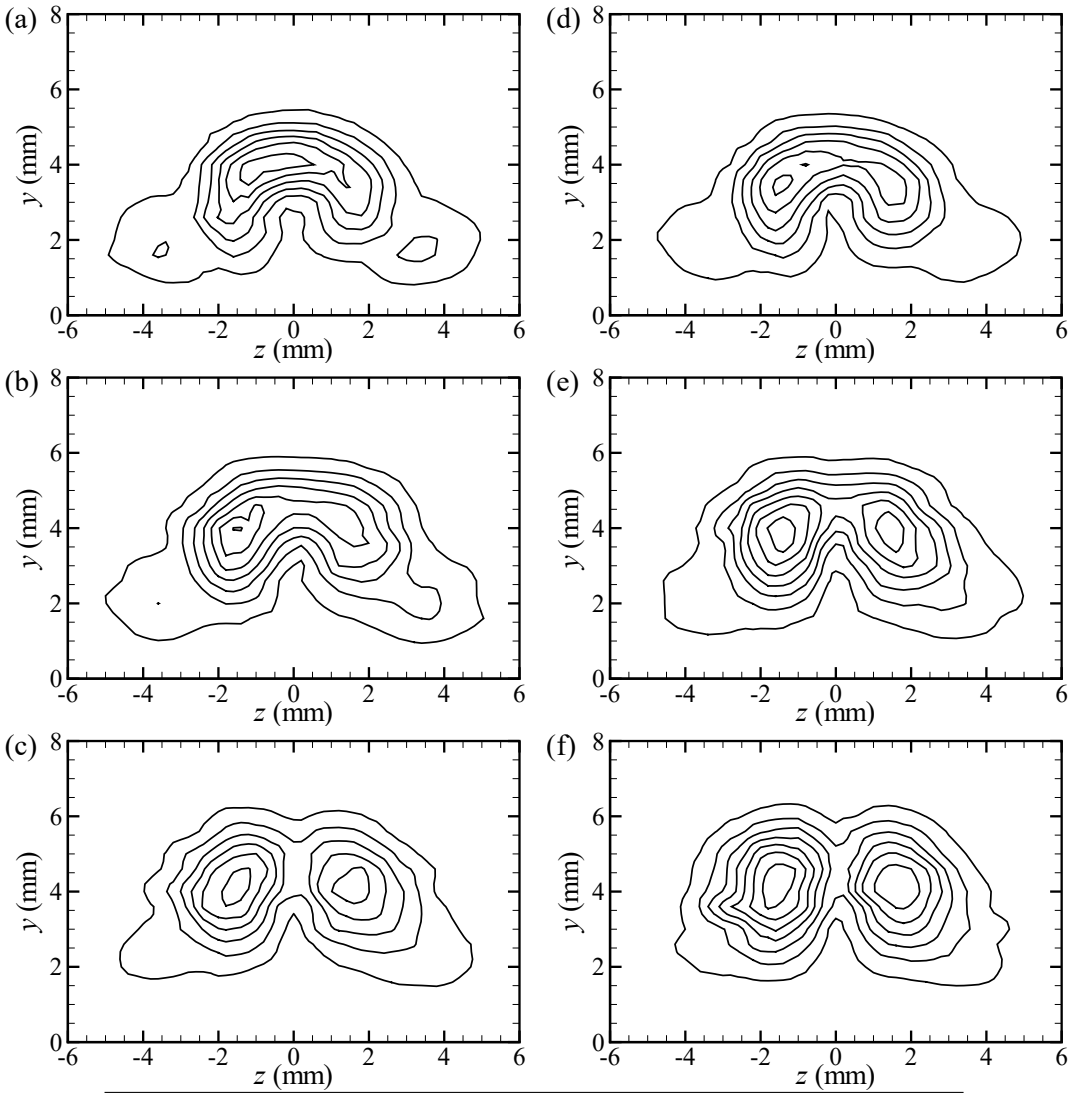

FIGURE 4.7: Distributions of u'/U_∞ in the (y, z) plane at $x - x_0$ = 60 mm (a, d), 100 mm (b, e) and 140 mm (c, f). (a) – (c) Case 1. (d) – (f) Case 2. Contour levels range from 0.0015 to 0.009 in (a) and (d), from 0.002 to 0.014 in (b) and (e), from 0.003 to 0.021 in (c) and (f).

Observed differences in these two cases were also distinct in the development of the disturbance structure. Figs. 4.7(a) – (f) display the amplitude distributions of the spectral components over 30 – 120 Hz in the (y, z) plane at $x - x_0$ = 60, 100 and 140 mm, respectively, in both cases. In Case 1 where C_t = +0.353, the excited disturbance had a large amplitude in both the horizontal ($\partial U/\partial y$) and vertical ($\partial U/\partial z$) shear layers at $x - x_0$ = 60 mm, as may

be seen in Fig. 4.7(a). In the downstream locations, however, it evolved into a sinuous instability mode whose amplitude distribution was symmetric with respect to the mid-span (z = 0), and whose amplitude vanished at z = 0 because it underwent a 180°-phase-jump across the midspan, as shown in the distributions at $x - x_0$= 100 mm (Fig. 4.7b) and 140 mm (Fig. 4.7c). In Case 2 where C_t = -0.104, on the other hand, the amplitude distribution already exhibited that of the sinuous mode at $x - x_0$ = 100 mm, as shown in Figs. 4.7(d) – (f).

To observe the development of sinuous streak instability in the present initial disturbance condition more clearly, Fig. 4.8 visualizes a sequence of the disturbance development leading to streak breakdown in Case 2 by means of the smoke-wire technique. Smoke was released from a smoke wire stretched at (x, y) = (100 mm, 4.5 mm), and the high-speed digital video pictures cover the region of $x - x_0$ = 100 – 250 mm. Here, the magnitude of the initial disturbance was set to be 1.5 times larger than that in Figs. 4.6 and 4.7 to observe the streak breakdown in the region up to $x - x_0$ = 250 mm. The maximum rms value u'_m attained about 10% of U_∞ at $x - x_0$ = 250 mm. We see a wavy motion of concentrated smoke along the low-speed streak, manifesting development of sinuous streak instability. The instability waves had a dominant wavelength of about 30 mm and convected at about 2.4 m/s (= $0.6U_\infty$), which corresponded to the frequency-selective disturbance growth around 80 Hz observed in the spectra. Corresponding to the broadband spectrum over 30 to 120 Hz, the sinuous instability waves appeared intermittently and took a large amplitude only within a few wavelengths. Fig. 4.9 displays waveforms of velocity (u) fluctuations measured at (y, z) = (4.5 mm, $\pm$1.5 mm) at $x - x_0$ = 180 mm in Case 2, showing that the phase relation of the u-fluctuations was 180° out of phase in most periods. Here, we examined the correlation coefficient of the two waveforms for 60 s and obtained a correlation coefficient of -0.95 at $x - x_0$ = 180 mm. Thus, a sinuous instability mode was dominantly amplified downstream, although waveforms were highly modulated in correspondence with the intermittent occurrence of the sinuous motion of a low-speed streak.

Then, let us compare the responses of the low-speed streak to the input disturbances (in Table 4.1) to that in the case of anti-symmetric excitation using the same turbulent signal. Fig. 4.10 illustrates the disturbance amplification for the anti-symmetric excitation (Case 6) in terms of the power spectra of u. The frequency-selective growth of 30 – 120 Hz-components were

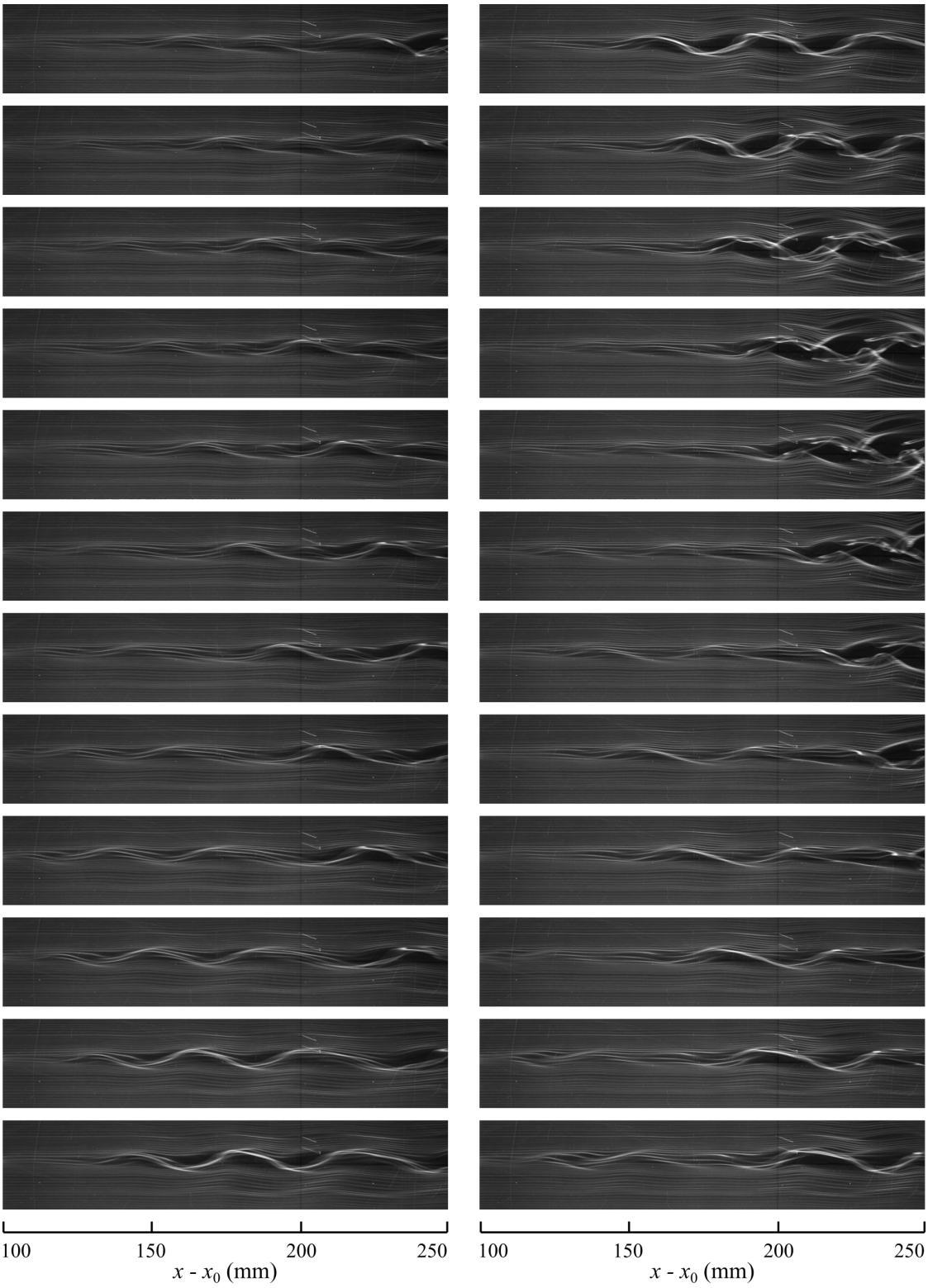

FIGURE 4.8: Flow visualization for Case 2. Smoke was released from a smoke-wire at (x, y) = (100 mm, 4.5 mm). Time increases from top to bottom. Time interval between pictures is 5.3 ms.

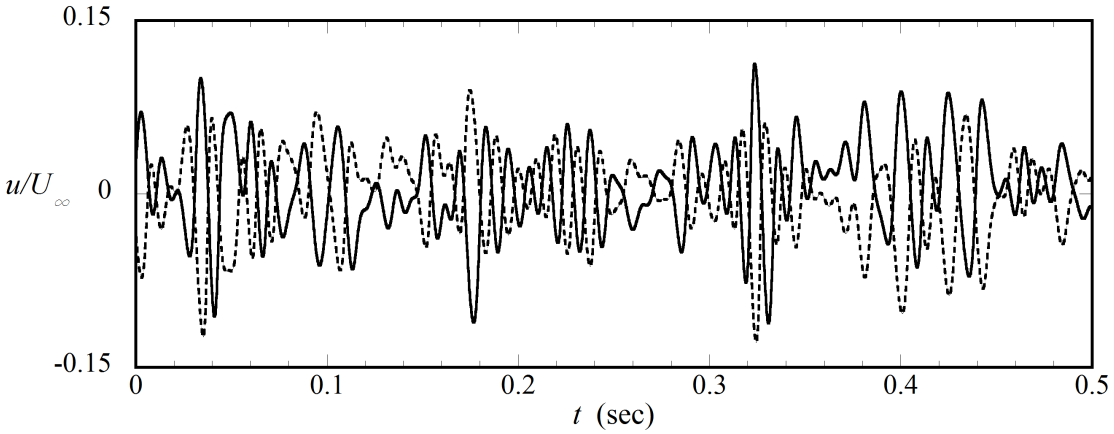

FIGURE 4.9: Waveforms of u measured at (y, z) = (4.5 mm, $\pm$ 1.5 mm) at $x - x_0$ = 180 mm for Case 2. Solid line; z = 1.5 mm, dotted line; z = -1.5 mm.

more distinguished at the downstream stations in this case, compared to Cases 1 and 2 (Figs. 4.6(a) and (b)). Fig. 4.11 compares streamwise growth of the disturbances (over 30 – 120 Hz) in Cases 1 and 2 to that in the case of anti-symmetric excitation (Case 6) in terms of u'_m, the maximum of u' at each x-location. In the figure, the result for symmetric excitation (Case 7) is also plotted for comparison. The disturbance growth in case of the anti-symmetric excitation was almost similar to that of sinuous mode (normal mode) excited at a single frequency. In Case 1 (C_t = +0.353), the disturbance grew more rapidly than that in the anti-symmetric excitation (Case 6) in the initial stage up to $x - x_0$ = 60 mm. This is due to growth of varicose mode as well as sinuous mode near the screen where the $\partial U/\partial y$-shear was intense, as understood from the disturbance growth in the symmetric excitation (Case 7) where only a varicose mode was excited by the forcing. The varicose mode ceased to grow beyond $x - x_0$ = 60 mm, while the sinuous mode continued to grow and became dominant beyond $x - x_0$ = 100 mm, where the disturbance had almost the same growth rate as that in the case of anti-symmetric excitation (Case 6). Importantly, the magnitude of disturbance in Case 1 (C_t = +0.353) was as large as 62% of that in the anti-symmetric excitation (Case 6) beyond $x - x_0$ = 100 mm. In Case 2 where C_t was slightly negative (C_t = -0.104), the magnitude of disturbance increased to about 78% of that in the anti-symmetric case. Thus, the spanwise coherence of the initial disturbance decisively governs the occurrence of streak instability modes.

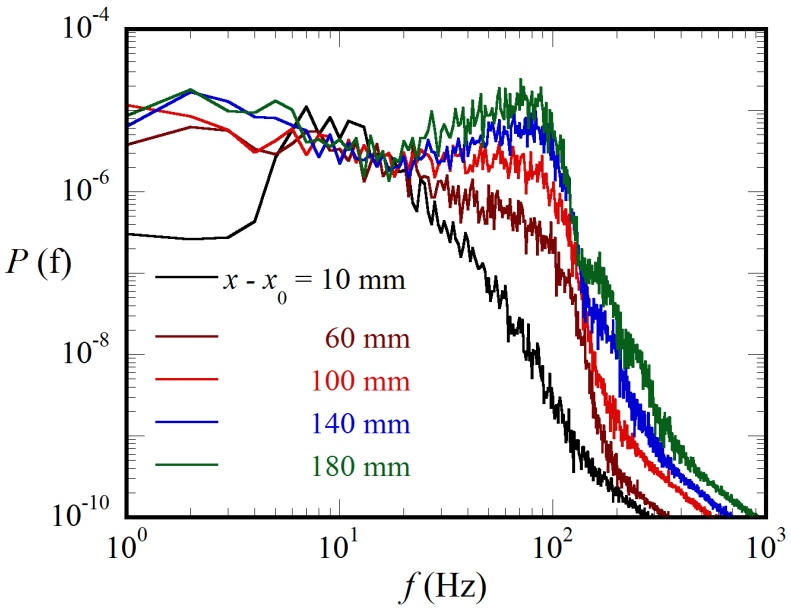

FIGURE 4.10: Power spectra of u in case of the anti-symmetric excitation (Case 6).

Regarding the disturbance development in the case of symmetric excitation with C_t = +1 (Case 7), we should add the following comments. If completely symmetric disturbances including background turbulence were provided, the value of u'_m would continue decaying downstream because the sinuous mode would not be excited directly by the forcing. However, the u'_m exhibited non-zero value. This is due to the fact that sinuous mode was excited by background turbulence and appear after the varicose mode decayed and vanished in the downstream region.

In order to see the dependence of the growth of sinuous streak instability on the spanwise coherence of initial disturbances more quantitatively, we conducted similar measurements in the other cases given in Table 4.1. Fig. 4.12 plots the ratio of the maximum rms value (u'_m) for each case to that for the anti-symmetric excitation $(u'_m)_a$, against the correlation coefficient C_t. Here, the magnitudes of the initial disturbance were the same for each set of disturbances (Cases 1 to 7 for turbulence data at $y^+ = 23$ and Cases 8 to 12 for turbulence data at $y^+ = 40$), and $u'_m/(u'_m)_a$ was calculated over 30 – 120 Hz at $x - x_0$ = 180 mm where the development of the sinuous mode was completely dominant. The correlation coefficients C_t (for 30 – 120 Hz components) were slightly negative (about -0.1) for Cases 2 to 4 and almost zero for Case 5. We see that the magnitudes of the sinuous instability mode excited

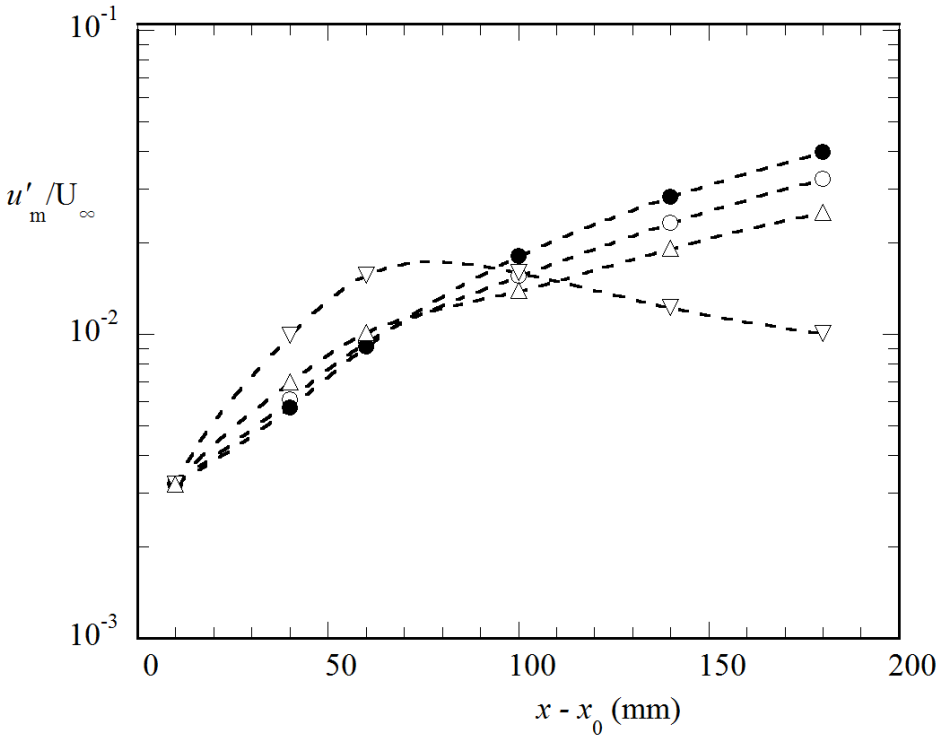

FIGURE 4.11: Streamwise development of disturbance (30 – 120 Hz) in Case 1 (△), Case 2 (○), Case 6 (●) and Case 7 (▽). u'_m/U_∞ versus $x - x_0$.

for these cases were more than 75% of that for the anti-symmetric excitation (C_t = -1). For Case 1 with positive-correlation of 0.353, the ratio $u'_m/(u'_m)_a$ was decreased but was still over 60%. This was also the case when we used turbulent-fluctuation data at $y^+ = 40$ as the initial disturbances. That is, the values of $u'_m/(u'_m)_a$ lied on the same curve for three cases of C_t = +0,561 (Case 8), +0.016 (Case 9) and -0.097 (Case 10), and approached zero as C_t tended to +1. Thus, the magnitude of streak instability mode excited is well correlated with the spanwise coherence of the initial disturbance. Here, it is noted that for the symmetric excitation with C_t = +1 (Cases 7 and 12), the varicose mode almost vanished at $x - x_0$ = 180 mm but the value of $u'_m/(u'_m)_a$ exhibited 0.15 – 0.2. This is because a sinuous mode originating from background turbulence developed and overcame the varicose mode (excited artificially) after the varicose mode decayed out.

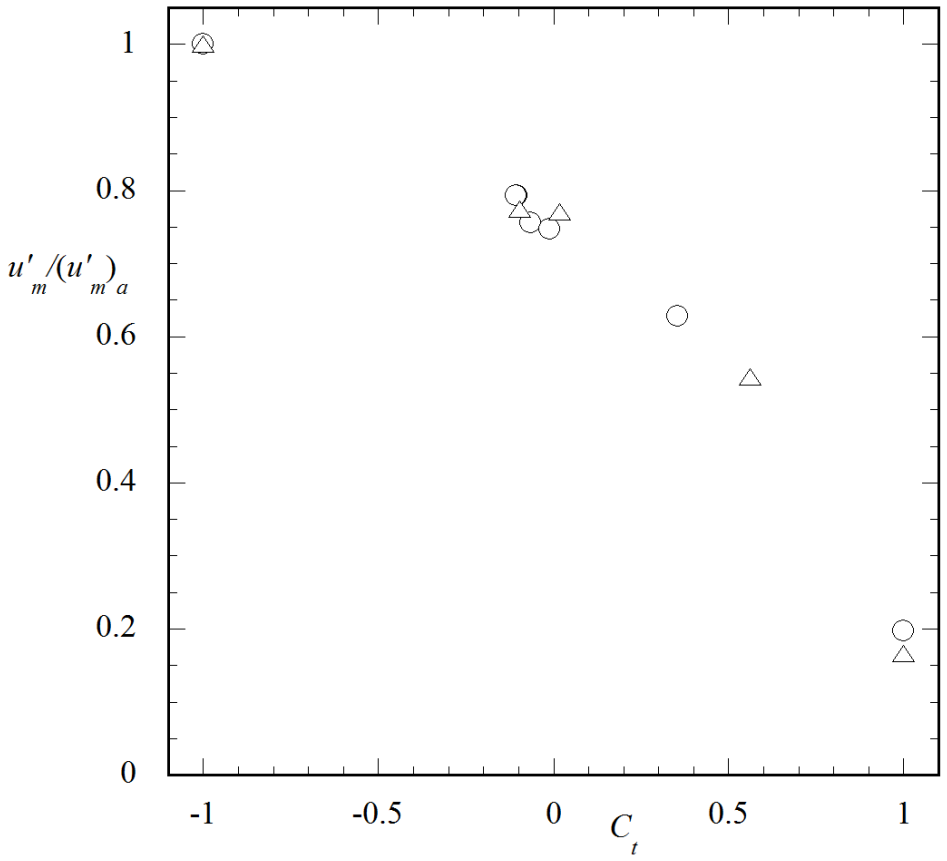

FIGURE 4.12: $u'_m/(u'_m)_a$ versus C_t at $x - x_0 = 180$ mm for spectral components over 30 – 120 Hz. ◯, Cases 1 to 7; △, Cases 8 to 12.

4.5 Conclusions

Instability and breakdown of a low-speed streak caused by disturbances whose frequency-spectrum was similar to that of wall turbulence were examined experimentally to understand how strongly the streak breakdown depended on the nature of external disturbances triggering the streak instability. A single low-speed streak which was almost free of longitudinal vortices was generated in a laminar boundary layer using a small piece of wire-gauze screen set normal to the wall, and disturbances were introduced by two loudspeakers through two small holes behind the screen, as previously done by Asai *et al.* [54]. A pair of velocity-fluctuation signals, measured simultaneously at two different spanwise locations with interval $\Delta z^+ = 24 - 149$ in the buffer region ($y^+ = 23$ and 40) of turbulent boundary layer at $Re_\tau \approx 530$ were used as the driving signals to the two loudspeakers. The correlation coefficients (C_t)

between the pair of velocity fluctuations ranged over -0.106 to +0.561. Development of streak instability for these initial disturbances was compared to that for anti-symmetric excitation using the same turbulence signal which was expected to be the most effective for exciting the sinuous streak instability.

Frequency-selective growth of the sinuous mode was observed far downstream in all cases. Even for the fluctuation signals with positive correlation coefficient, C_t = 0.351, the sinuous instability mode was dominant in the downstream region; a varicose mode grew more rapidly in the initial stage but soon turned to decay downstream. Comparison of development of the dominant sinuous mode showed that even when initial disturbances with a nearly zero correlation coefficient ($C_t \sim -0.01$) was provided, the magnitude of the sinuous instability mode was as large as 75% of that for the most efficient anti-symmetric forcing ($C_t = -1.0$), in terms of u'_m. When the low-speed streak was forced by turbulent-fluctuation signals with slightly negative correlation coefficient, $C_t \approx -0.1$ (made from velocity fluctuations at two different z positions with Δz^+ = 45 – 90 in the turbulent boundary layer), the magnitude of the sinuous mode excited was increased to about 80% of the value in the case of anti-symmetric excitation. Thus, contrary to our expectation, dependence of the magnitude of the sinuous mode on the nature of the initial disturbances was not so strong for $-1 \leq C_t \leq 0$. When a disturbance with the positive correlation coefficient of C_t = 0.561 (obtained for Δz^+ = 24 and y^+ = 40) was introduced, the magnitude of the sinuous mode excited was still more than 50% of the value of the anti-symmetric excitation. Based on the present experiment, we may infer that disturbances existing in near-wall turbulence are rather effective for causing sinuous streak instability and breakdown into a train of quasi-streamwise vortices.

Chapter 5

Summary

In order to better understand some fundamental aspects of instability events dominating the boundary-layer transition as well as to clarify the effects of riblets used for the turbulent drag reduction on the growth of Tollmien-Schlichting (T-S) waves and the lateral turbulent contamination process responsible for the lateral growth of turbulent wedge/spot. The main results presented in the thesis are summarized in this chapter.

First focus was on the influences of riblets on the linear instability mechanism causing the amplification of T-S waves. This experiment was carried out in a low-turbulence laminar channel flow which had the similar instability nature as the zero-pressure-gradient boundary layer (Blasius flow). Riblets having triangular ridges (with ridge angle of 30°) and trapezoidal valleys, with a height-to-width ratio of 0.5, were glued on the upper channel wall. The ridge spacing was 11% of the channel half-depth which gave a non-dimensional wavenumber of 57. In addition to the effects of streamwise riblets, the effects of oblique riblets whose direction was inclined to the streamwise direction were examined to see how the instability characteristics depended on the riblet alignment. The result showed that the critical Reynolds number for the linear instability Re_{cr} was reduced to about 4200 by the streamwise riblets, while the wavenumber of T-S wave was little influenced by the presence of riblets. For the present small-sized riblets, the parabolic velocity profile was modified only in the vicinity of ribbed surface, with the virtual wall position located inside the riblets. Such a local and small change in the velocity profile enhanced the instability of plane Poiseuille flow appreciably. When the riblets were inclined to the streamwise direction, Re_{cr} increased as the oblique angle of riblets ϕ was increased. For $\phi \geq 45°$, the riblets had no noticeable influence on the structure of T-S wave and the growth

rates were the same as those in the smooth-wall case.

Next experiment included the effects of streamwise riblets on the lateral growth of turbulent region localized in span in a zero-pressure-gradient boundary-layer. Riblets used here have the same geometry to one used in the experiment of Chapter 2. The riblet size (ridge spacing) was about 14 or 28 in wall units using the friction velocity in the developed turbulent region, whereas in the ambient laminar boundary-layer, the height of riblets was less than one-third the displacement thickness in the Reynolds-number range $R_x = 2 - 6 \times 10^5$. The lateral spreading angle of turbulent region (including the intermittent turbulent region) increased with R_x and tended to a value slightly larger than 10° for $R_x > 6 \times 10^5$ over the smooth surface. Detailed comparisons showed that riblets weakened the lateral growth of the turbulent region, with the spreading angle reduced by about 6% compared to the smooth surface in the Reynolds number range examined. The destabilizing effect of riblets intensified the amplitude of oblique waves developing outside the laminar-turbulent interface appreciably, but the result strongly suggested that the development of oblique waves had no decisive effect on lateral contamination. A large packet of turbulent eddies like a turbulent spot frequently appeared on the outer edge of the turbulent region in the downstream, and could have contributed to the lateral growth of turbulent region, in addition to the successive occurrence of low-speed streaks immediately outside the turbulent region. Riblets could have affected these near-wall turbulent structures in the laminar-turbulent-interface region, with a 10% reduction of the rms value of streamwise velocity fluctuations.

The third experiment was conducted to examine the instability and breakdown of a low-speed streak, one of the key mechanisms in generation and sustenance mechanism of the wall turbulence structure. In this study, a single low-speed streak was generated using a small piece of screen set normal to a boundary-layer plate, and disturbances made by two loudspeakers were introduced through two small holes. Streak instability was artificially excited by using a pair of forcing signals deduced from turbulent velocity fluctuations of near-wall turbulence with various spanwise coherences to see how strongly the streak breakdown depended on the nature of disturbances. The correlation coefficient C_t of the two turbulent signals ranged from -0.11 to 0.56. Both sinuous and varicose modes were excited but the former became dominant downstream in all cases. The magnitude of the sinuous instability mode excited was dependent on the initial disturbances, but not strongly for

$-1 \leq C_t \leq 0$. For instance, the magnitude (the rms value of velocity fluctuations) of the sinuous instability mode for the initial disturbance with $C_t \sim 0$ was about 75% of that in the case of anti-symmetric forcing which gave the largest magnitude.

Thus, the present results improved our knowledge on the instability and transition as well as effects of riblets, passive device of friction drag reduction, and no doubt make contributions to development of drag reducing technology of airfoil boundary layer.

Bibliography

[1]W. Pfenninger and V. D. Reed, "Laminar-Flow Research and Experiments", Astronautics and Aeronautics **4**, 44–47, 49, 50 (1966).

[2]B. J. Holmes and C. J. Obara, "Flight Research on Natural Laminar Flow Applications", in *Natural laminar flow and laminar flow control*, edited by R. Barnwell and M. Hussaini (Springer New York, 1992), pp. 73–142.

[3]J. N. Hefner, "Laminar Flow Control: Introduction and Overview", in *Natural laminar flow and laminar flow control*, edited by R. Barnwell and M. Hussaini (Springer New York, 1992), pp. 1–21.

[4]R. D. Wagner, D. V. Maddalon, D. W. Bartlett, F. S. Collier, and A. L. Braslow, "Laminar Flow Flight Experiments - A Review", in *Natural laminar flow and laminar flow control*, edited by R. Barnwell and M. Hussaini (Springer New York, 1992), pp. 23–71.

[5]C. J. Obara, "Sublimating Chemical Technique for Boundary-Layer Flow Visualization in Flight Testing", Journal of Aircraft **25**, 493–498 (1988).

[6]T. Herbert, "Modes of Secondary Instability in Plane Poiseuille Flow", in *Turbulence and chaotic phenomena in fluids; proceedings of the international symposium, kyoto, japan, september 5-10*, edited by T. Tatsumi (North-Holland Amsterdam, 1984), pp. 53–58.

[7]S. A. Orszag and A. T. Patera, "Secondary Instability of Wall-Bounded Shear Flows", Journal of Fluid Mechanics **128**, 347 (1983).

[8]E. Reshotko, "Disturbances in a Laminar Boundary Layer due to Distributed Surface Roughness", in *Turbulence and chaotic phenomena in fluids; proceedings of the international symposium, kyoto, japan, september 5-10*, edited by T. Tatsumi (North-Holland Amsterdam, 1984), pp. 39–46.

[9]M. V. Morkovin, "On Roughness - Induced Transition: Facts, Views, and Speculations", in *Instability and transition, volume i*, edited by M. Y. Hussaini and R. G. Voigt (Springer, New York, 1990), pp. 281–295.

[10]O. Reynolds, "An Experimental Investigation of the Circumstances Which Determine Whether the Motion of Water Shall Be Direct or Sinuous, and of the Law of Resistance in Parallel Channels", Philosophical Transactions of the Royal Society of London **174**, 935–982 (1883).

[11]L. Rayleigh, "On the Stability, or Instability, of Certain Fluid Motions", Proceedings of the London Mathematical Society **s1-11**, 57–72 (1879).

[12]L. Rayleigh, "On the Stability or Instability of Certain Fluid Motions, II", Proceedings of the London Mathematical Society **s1-19**, 67–75 (1887).

[13]L. Rayleigh, "On the Question of the Stability of the Flow of Fluids", Philosophical Magazine Series 5 **34**, 59–70 (1892).

[14]L. Rayleigh, "On the Stability or Instability of Certain Fluid Motions, III", Proceedings of the London Mathematical Society **s1-27**, 5–12 (1895).

[15]L. Rayleigh, "On the Dynamics of Revolving Fluids", Proceedings of the Royal Society A: Mathematical, Physical and Engineering Sciences **93**, 148–154 (1917).

[16]W. M. Orr, "The Stability or Instability of the Steady Motions of a Perfect Liquid and of a Viscous Liquid. Part II: A Viscous Liquid", Proceedings of the Royal Irish Academy. Section A: Mathematical and Physical Sciences **27**, 69–138 (1907).

[17]A. Sommerfeld, "Ein Beitrag Zur Hydrodynamischen Erklärung der Turbulenten Flüssigkeitsbewegung", Proceedings of the 4th International Mathematical Congress, Rome **3**, 116–124 (1908).

[18]W. Tollmien, "Über die Entstehung der Turbulenz", Nachrichten von der Gesellschaft der Wissenschaften zu Göttingen, Mathematisch-Physikalische Klasse, 21–44 (1929).

[19]H. Schlichting, "Zur Enstehung der Turbulenz bei der Plattenströmung", Nachrichten von der Gesellschaft der Wissenschaften zu Göttingen, Mathematisch-Physikalische Klasse, 181–208 (1933).

[20]G. B. Schubauer and H. K. Skramstad, "Laminar Boundary-Layer Oscillations and Stability of Laminar Flow", Journal of the Aeronautical Sciences **14**, 69–78 (1947).

[21]M. V. Morkovin, "On the Many Faces of Transition", in *Viscous drag reduction* (Springer US, Boston, MA, 1969), pp. 1–31.

[22]H. Schlichting and K. Gersten, *Boundary-Layer Theory* (Springer, 2000), p. 799.

[23]M. Nishioka, S. Iida, and Y. Ichikawa, "An Experimental Investigation of the Stability of Plane Poiseuille Flow", Journal of Fluid Mechanics **72**, 731 (1975).

[24]M. Nishioka, M. Asai, and S. Iida, "An Experimental Investigation of the Secondary Instability", in Laminar-turbulent transition; proceedings of the symposium, stuttgart, west germany, september 16-22, 1979. (1980), pp. 37–46.

[25]M. Nishioka and M. Asai, "Evolution of Tollmien-Schlichting Waves into Wall Turbulence", in *Turbulence and chaotic phenomena in fluids; proceedings of the international symposium, kyoto, japan, september 5-10*, edited by T. Tatsumi (North-Holland Amsterdam, 1984), pp. 87–92.

[26]W. S. Saric, H. L. Reed, and E. J. Kerschen, "Boundary-Layer Receptivity to Freestream Disturbances", Annual Review of Fluid Mechanics **34**, 291–319 (2002).

[27]M. V. Morkovin, *Critical Evaluation of Transition from Laminar to Turbulent Shear Layers with Emphasis on Hypersonically Traveling Bodies*, tech. rep. (Air Force Flight Dynamics Lab., Wright-Patterson AFB, Ohio, 1969).

[28]M. Nishioka and M. V. Morkovin, "Boundary-layer receptivity to unsteady pressure gradients: experiments and overview", Journal of Fluid Mechanics **171**, 219 (1986).

[29]W. S. Saric, E. B. White, and H. L. Reed, "Boundary-Layer Receptivity to Freestream Disturbances and Its Role in Transition", in 30th fluid dynamics conference (1999).

[30]H. Schlichting, "Amplitudenverteilung und Energiebilanz der Kleinen Störungen bei der Plattenströmung", Math. Phys. Klasse, Fachgruppe, Nachr. Ges. Wiss. Göttingen, Göttingen **1**, 47–78 (1935).

[31]A. V. Boiko, A. V. Dovgal, G. R. Grek, and V. V. Kozlov, "Instability of the Flat-Plate Boundary Layer", in *Physics of transitional shear flows*, Volume I (Springer Netherlands, 2012), pp. 47–66.

[32]B. G. B. Klingmann, "Experiments on the Stability of Tollmien-Schlichting Waves", Eur. J. Mech., B/Fluids **12**, 493–514 (1993).

[33]M. Gaster, "On the Effects of Boundary-Layer Growth on Flow Stability", Journal of Fluid Mechanics **66**, 465 (1974).

[34]T. Herbert, "Secondary Instability of Plane Channel Flow to Subharmonic Three-Dimensional Disturbances", Physics of Fluids **26**, 871 (1983).

[35]W. S. Saric and A. S. W. Thomas, "Experiments on the Subharmonic Route to Turbulence in Boundary Layers", in *Turbulence and chaotic phenomena in fluids; proceedings of the international symposium, kyoto, japan, september 5-10*, edited by T. Tatsumi (North-Holland Amsterdam, 1984), pp. 117–122.

[36]A. D. D. Craik, "Non-Linear Resonant Instability in Boundary Layers", Journal of Fluid Mechanics **50**, 393 (1971).

[37]P. S. Klebanoff, K. D. Tidstrom, and L. M. Sargent, "The Three-Dimensional Nature of Boundary-Layer Instability", Journal of Fluid Mechanics **12**, 1 (1962).

[38]Y. S. Kachanov, V. V. Kozlov, and V. Y. Levchenko, "Nonlinear Development of a Wave in a Boundary Layer", Fluid Dynamics **12**, 383–390 (1978).

[39]F. R. Hama and J. Nutant, "Detailed Flow-Field Observations in the Transition Process in a Thick Boundary Layer", Proc. 1963 Heat Transfer and Fluid Mechanics Inst., 2877–93 (1963).

[40]L. S. G. Kovasznay, H. Komoda, and B. R. Vasudeva, "Proceedings of the 1962 Heat Transfer and Fluid Mechanics Institute", in (1962).

[41]M. Nishioka, M. Asai, and S. Iida, "Wall Phenomena in the Final Stage of Transition to Turbulence", in *Transition and turbulence; proceedings of the symposium on transition and turbulence in fluids, madison, wi, october 13-15, 1980* (Academic Press, New York, 1981), pp. 113–126.

[42]M. Asai and M. Nishioka, "Origin of The Peak-Valley Wave Structure Leading to Wall Turbulence", Journal of Fluid Mechanics **208**, 1–23 (1989).

[43]N. D. Sandham and L. Kleiser, "The Late Stages of Transition to Turbulence in Channel Flow", Journal of Fluid Mechanics **245**, 319 (1992).

[44]U. Rist and H. Fasel, "Direct Numerical Simulation of Controlled Transition in a Flat-Plate Boundary Layer", Journal of Fluid Mechanics **298**, 211 (1995).

[45]M. Matsubara and P. H. Alfredsson, "Disturbance Growth in Boundary Layers Subjected to Free-Stream Turbulence", Journal of Fluid Mechanics **430** (2001).

[46]P. Andersson, M. Berggren, and D. S. Henningson, "Optimal Disturbances and Bypass Transition in Boundary Layers", Physics of Fluids **11**, 134 (1998).

[47]P. Luchini, "Reynolds-Number-Independent Instability of the Boundary Layer Over a Flat Surface: Optimal Perturbations", Journal of Fluid Mechanics **404** (2000).

[48]M. T. Landahl, "A Note on an Algebraic Instability of Inviscid Parallel Shear Flows", Journal of Fluid Mechanics **98**, 243 (1980).

[49]L. S. Hultgren and L. H. Gustavsson, "Algebraic Growth of Disturbances in a Laminar Boundary Layer", Physics of Fluids **24**, 1000 (1981).

[50]K. M. Butler and B. F. Farrell, "Three-Dimensional Optimal Perturbations in Viscous Shear Flow", Physics of Fluids A: Fluid Dynamics **4**, 1637–1650 (1992).

[51]P. J. Schmid and D. S. Henningson, "Transition to Turbulence", in *Stability and transition in shear flows* (Springer-Verlag, 2001) Chap. 2, pp. 401–475.

[52]J. H. M. Fransson, L. Brandt, A. Talamelli, and C. Cossu, "Experimental and Theoretical Investigation of the Nonmodal Growth of Steady Streaks in a Flat Plate Boundary Layer", Physics of Fluids **16**, 3627–3638 (2004).

[53]P. A. Elofsson, M. Kawakami, and P. H. Alfredsson, "Experiments on the Stability of Streamwise Streaks in Plane Poiseuille Flow", Physics of Fluids **11**, 915 (1999).

[54]M. Asai, M. Minagawa, and M. Nishioka, "The Instability and Breakdown of a Near-Wall Low-Speed Streak", Journal of Fluid Mechanics **455**, 289–314 (2002).

[55]Y. Konishi and M. Asai, "Experimental Investigation of the Instability of Spanwise-Periodic Low-Speed Streaks", Fluid Dynamics Research **34**, 299–315 (2004).

[56]Y. Konishi and M. Asai, "Development of Subharmonic Disturbance in Spanwise-Periodic Low-Speed Streaks", Fluid Dynamics Research **42**, 035504 (2010).

[57]J. Mans, E. C. Kadijk, H. C. de. Lange, and A. A. van. Steenhoven, "Breakdown in a Boundary Layer Exposed to Free-Stream Turbulence", Experiments in Fluids **39**, 1071–1083 (2005).

[58]J. Mans, H. C. de. Lange, and A. A. van. Steenhoven, "Sinuous Breakdown in a Flat Plate Boundary Layer Exposed to Free-Stream Turbulence", Physics of Fluids **19**, 088101 (2007).

[59]J. H. M. Fransson, M. Matsubara, and P. H. Alfredsson, "Transition Induced by Free-Stream Turbulence", Journal of Fluid Mechanics **527**, 1–25 (2005).

[60]H. Q. Ho, M. Asai, and S. Takagi, "Experimental Study on Dependence of Streak Breakdown on Disturbance Nature", European Journal of Mechanics, B/Fluids **66**, 1–9 (2017).

[61]L. Brandt and D. S. Henningson, "Transition of Streamwise Streaks in Zero-Pressure-Gradient Boundary Layers", Journal of Fluid Mechanics **472** (2002).

[62]L. Brandt, P. Schlatter, and D. S. Henningson, "Transition in Boundary Layers Subject to Free-Stream Turbulence", Journal of Fluid Mechanics **517**, 167–198 (2004).

[63]P. H. Schlatter, L. Brandt, H. C. de. Lange, and D. S. Henningson, "On Streak Breakdown in Bypass Transition", Physics of Fluids **20**, 101505 (2008).

[64]T. A. Zaki, "From Streaks to Spots and on to Turbulence: Exploring the Dynamics of Boundary Layer Transition", Flow, Turbulence and Combustion **91**, 451–473 (2013).

[65]M. J. P. Hack and T. A. Zaki, "Streak Instabilities in Boundary Layers Beneath Free-Stream Turbulence", Journal of Fluid Mechanics **741**, 280–315 (2014).

[66]W. Schoppa and F. Hussain, "Genesis of Longitudinal Vortices in Near-Wall Turbulence", Meccanica **33**, 489–501 (1998).

[67]J. Jeong, F. Hussain, W. Schoppa, and J. Kim, "Coherent Structures Near the Wall in a Turbulent Channel Flow", Journal of Fluid Mechanics **332**, 185–214 (1997).

[68]R. E. Falco, "Coherent Motions in the Outer Region of Turbulent Boundary Layers", Physics of Fluids **20**, S124 (1977).

[69]G. L. Brown and A. S. W. Thomas, "Large Structure in a Turbulent Boundary Layer", Physics of Fluids **20**, S243 (1977).

[70]G. R. Offen and S. J. Kline, "Combined Dye-Streak and Hydrogen-Bubble Visual Observations of a Turbulent Boundary Layer", Journal of Fluid Mechanics **62**, 223 (1974).

[71]G. R. Offen and S. J. Kline, "A Proposed Model of the Bursting Process in Turbulent Boundary Layers", Journal of Fluid Mechanics **70**, 209 (1975).

[72]S. K. Robinson, "Coherent Motions in the Turbulent Boundary Layer", Annual Review of Fluid Mechanics **23**, 601–639 (1991).

[73]J. Jeong and F. Hussain, "On the Identification of a Vortex", Journal of Fluid Mechanics **285**, 69 (1995).

[74]J. M. Hamilton, J. Kim, and F. Waleffe, "Regeneration Mechanisms of Near-Wall Turbulence Structures", Journal of Fluid Mechanics **287**, 317 (1995).

[75]J. Jiménez and A. Pinelli, "The Autonomous Cycle of Near-Wall Turbulence", Journal of Fluid Mechanics **389** (1999).

[76]G. Kawahara and S. Kida, "Periodic Motion Embedded in Plane Couette Turbulence: Regeneration Cycle and Burst", Journal of Fluid Mechanics **449**, 291 (2001).

[77]T. Itano and S. Toh, "The Dynamics of Bursting Process in Wall Turbulence", Journal of the Physical Society of Japan **70**, 703–716 (2001).

[78]W. Schoppa and F. Hussain, "Coherent Structure Generation in Near-Wall Turbulence", Journal of Fluid Mechanics **453**, 57–108 (2002).

[79]R. J. Adrian, C. D. Meinhart, and C. D. Tomkins, "Vortex Organization in the Outer Region of the Turbulent Boundary Layer", Journal of Fluid Mechanics **422** (2000).

[80]D. W. Bechert, M. Bruse, W. Hage, J. G. T. Van Der Hoeven, and G. Hoppe, "Experiments on Drag-Reducing Surfaces and Their Optimization with an Adjustable Geometry", Journal of Fluid Mechanics **338** (1997).

[81]M. J. Walsh, "Drag Characteristics of V-Groove and Transverse Curvature Riblets", in *Viscous flow drag reduction, progress in astronautics and aeronautics*, edited by G. R. Hough (American Institute of Aeronautics and Astronautics, New York, 1980), pp. 168–184.

[82]M. J. Walsh, "Riblets as a Viscous Drag Reduction Technique", AIAA Journal **21**, 485–486 (1983).

[83]M. J. Walsh, "Effect of Detailed Surface Geometry on Riblet Drag Reduction Performance", Journal of Aircraft **27**, 572–573 (1990).

[84]M. J. Walsh, "Riblets", in *Viscous drag reduction in boundary layers*, edited by D. M. Bushnell and J. N. Hefner (AIAA, Washington DC, 1990), pp. 203–261.

[85]K. Choi, "Near-Wall Structure of a Turbulent Boundary Layer with Riblets", Journal of Fluid Mechanics **208**, 417 (1989).

[86]D. W. Bechert and M. Bartenwerfer, "The Viscous Flow on Surfaces with Longitudinal Ribs", Journal of Fluid Mechanics **206**, 105 (1989).

[87]H. Choi, P. Moin, and J. Kim, "Direct Numerical Simulation of Turbulent Flow over Riblets", Journal of Fluid Mechanics **255**, 503 (1993).

[88]R. García-Mayoral and J. Jiménez, "Hydrodynamic Stability and Breakdown of the Viscous Regime over Riblets", Journal of Fluid Mechanics **678**, 317–347 (2011).

[89]Y. Suzuki and N. Kasagi, "Turbulent Drag Reduction Mechanism above a Riblet Surface", AIAA Journal **32**, 1781–1790 (1994).

[90]R. García-Mayoral and J. Jiménez, "Scaling of Turbulent Structures in Riblet Channels up to $Re_\tau \approx 550$", Physics of Fluids **24**, 105101 (2012).

[91]P. Luchini, F. Manzo, and A. Pozzi, "Resistance of a Grooved Surface to Parallel Flow and Cross-Flow", Journal of Fluid Mechanics Digital Archive **228**, 87 (1991).

[92]P. Luchini and G. Trombetta, "Effects of Riblets upon Flow Stability", Applied Scientific Research **54**, 313–321 (1995).

[93]U. Ehrenstein, "On the Linear Stability of Channel Flow over Riblets", Physics of Fluids **8**, 3194 (1998).

[94]H. V. Moradi and J. M. Floryan, "Stability of Flow in a Channel with Longitudinal Grooves", Journal of Fluid Mechanics **757**, 613–648 (2014).

[95]G. R. Grek, V. V. Kozlov, and S. V. Titarenko, "An Experimental Study of the Influence of Riblets on Transition", Journal of Fluid Mechanics **315**, 31 (1996).

[96]A. Inasawa, J. M. Floryan, and M. Asai, "Flow Recovery Downstream from a Surface Protuberance", Theoretical and Computational Fluid Dynamics **28**, 427–447 (2014).

[97]R. M. Sadri and J. M. Floryan, "Entry Flow in a Channel", Computers & Fluids **31**, 133–157 (2002).

[98]M. Asai and J. M. Floryan, "Certain Aspects of Channel Entrance Flow", Physics of Fluids **16**, 1160–1163 (2004).

[99]M. Nishioka and M. Asai, "Some Observations of the Subcritical Transition in Plane Poiseuille Flow", Journal of Fluid Mechanics **150**, 441 (1985).

[100]M. Asai and J. M. Floryan, "Experiments on the Linear Instability of Flow in a Wavy Channel", European Journal of Mechanics - B/Fluids **25**, 971–986 (2006).

[101]J. M. Floryan, "Two-Dimensional Instability of Flow in a Rough Channel", Physics of Fluids **17**, 044101 (2005).

[102]J. M. Floryan and M. Asai, "On the Transition Between Distributed and Isolated Surface Roughness and Its Effect on the Stability of Channel Flow", Physics of Fluids **23**, 104101 (2011).

[103]M. D. Ma'mun, M. Asai, and A. Inasawa, "Effects of Surface Corrugation on the Stability of a Zero-Pressure-Gradient Boundary Layer", Journal of Fluid Mechanics **741**, 228–251 (2014).

[104]M. D. Ma'mun and M. Asai, "Influences of Oblique Surface Corrugation on Boundary-Layer Instability", Journal of the Physical Society of Japan **83**, 084402 (2014).

[105]M. Asai, Y. Konishi, Y. Oizumi, and M. Nishioka, "Growth and Breakdown of Low-Speed Streaks Leading to Wall Turbulence", Journal of Fluid Mechanics **586**, 371 (2007).

[106]M. Mochizuki, "Smoke Observation on Boundary Layer Transition Caused by a Spherical Roughness Element", Journal of the Physical Society of Japan **16**, 995–1008 (1961).

[107]H. W. Emmons, "The Laminar-Turbulent Transition in a Boundary Layer - Part I", Journal of the Aeronautical Sciences **18**, 490–498 (1951).

[108]G. B. Schubauer and P. S. Klebanoff, "Contributions on the Mechanics of Boundary-Layer Transition", NACA-TR-1289 (1956).

[109]J. W. Elder, "An Experimental Investigation of Turbulent Spots and Breakdown to Turbulence", Journal of Fluid Mechanics **9**, 235 (1960).

[110]I. Wygnanski, M. Sokolov, and D. Friedman, "On a Turbulent 'Spot' in a Laminar Boundary Layer", Journal of Fluid Mechanics **78**, 785 (1976).

[111]M. Gad-El-Hak, R. F. Blackwelderf, and J. J. Riley, "On the Growth of Turbulent Regions in Laminar Boundary Layers", Journal of Fluid Mechanics **110**, 73 (1981).

[112]A. E. Perry, T. T. Lim, and E. W. Teh, "A Visual Study of Turbulent Spots", Journal of Fluid Mechanics **104**, 387 (1981).

[113]I. Wygnanski, M. Zilberman, and J. H. Haritonidis, "On The Spreading of a Turbulent Spot in the Absence of a Pressure Gradient", Journal of Fluid Mechanics **123**, 69 (1982).

[114]P. Lindeerg, E. M. Fahlgren, P. H. Alfredsson, and A. V. Johansson, "An Experimental Study of the Structure and Spreading of Turbulent Spots", in *Laminar-turbulent transition* (Springer Berlin Heidelberg, Berlin, Heidelberg, 1985), pp. 617–624.

[115]D. S. Henningson, P. R. Spalart, and J. Kim, "Numerical Simulations of Turbulent Spots in Plane Poiseuille and Boundary-Layer Flow", Physics of Fluids **30**, 2914 (1987).

[116]M. Asai, K. Sawada, and M. Nishioka, "Development of Turbulent Patch in a Subcritical Boundary-Layer Transition", Fluid Dynamics Research **18**, 151–164 (1996).

[117]A. Jocksch and L. Kleiser, "The Effect of Shock-Wave / Boundary-Layer Interaction on Turbulent Spot Propagation", PAMM **7**, 4110009–4110010 (2007).

[118]M. S. Kuester and E. B. White, "Structure of Turbulent Wedges Created by Isolated Surface Roughness", Experiments in Fluids **57**, 47 (2016).

[119]D. B. Goldstein, J. Chu, and G. Brown, "Lateral Spreading Mechanism of a Turbulent Spot and a Turbulent Wedge", Flow, Turbulence and Combustion **98**, 21–35 (2017).

[120]J. S. Strand and D. B. Goldstein, "Direct Numerical Simulations of Riblets to Constrain the Growth of Turbulent Spots", Journal of Fluid Mechanics **668**, 267–292 (2011).

[121]M. Asai and M. Nishioka, "Boundary-Layer Transition Triggered by Hairpin Eddies at Subcritical Reynolds Numbers", Journal of Fluid Mechanics **297**, 101 (1995).

[122]H. Q. Ho and M. Asai, "Experimental Study on the Stability of Laminar Flow in a Channel With Streamwise and Oblique Riblets", Physics of Fluids **30**, 024106 (2018).

[123]H. Fasel and U. Konzelmann, "Non-parallel Stability of a Flat-plate Boundary Layer Using the Complete Navier-Stokes Equations", Journal of Fluid Mechanics **221**, 311 (1990).

[124]F. P. Bertolotti, T. Herbert, and P. R. Spalart, "Linear and Nonlinear Stability of the Blasius Boundary Layer", Journal of Fluid Mechanics **242**, 441 (1992).

[125]R. J. Adrian, "Hairpin Vortex Organization in Wall Turbulence", Physics of Fluids **19**, 041301 (2007).

[126]S. Deng, C. Pan, J. Wang, and G. He, "On the Spatial Organization of Hairpin Packets in a Turbulent Boundary Layer at Low-to-Moderate Reynolds Number", Journal of Fluid Mechanics **844**, 635–668 (2018).

[127]C. R. Smith, J. D. A. Walker, A. H. Haidari, and U. Sobrun, "On the Dynamics of Near-Wall Turbulence", Philosophical Transactions of the Royal Society of London. Series A: Physical and Engineering Sciences **336**, edited by J. D. A. Walker and F. T. Smith, 131–175 (1991).

[128]T. Herbert, "Secondary Instability of Boundary Layers", Annual Review of Fluid Mechanics **20**, 487–526 (1988).

[129]S. C. Reddy, P. J. Schmid, J. S. Baggett, and D. S. Henningson, "On Stability of Streamwise Streaks and Transition Thresholds in Plane Channel Flows", Journal of Fluid Mechanics **365** (1998).

[130]P. Andersson, L. Brandt, A. Bottaro, and D. S. Henningson, "On the Breakdown of Boundary Layer Streaks", Journal of Fluid Mechanics **428** (2001).

[131]L. Brandt, C. Cossu, J. Chomaz, P. Huerre, and D. S. Henningson, "On the Convectively Unstable Nature of Optimal Streaks in Boundary Layers", Journal of Fluid Mechanics **485** (2003).

[132]N. J. Vaughan and T. A. Zaki, "Stability of Zero-Pressure-Gradient Boundary Layer Distorted by Unsteady Klebanoff Streaks", Journal of Fluid Mechanics **681**, 116–153 (2011).

[133]A. C. Mandal and J. Dey, "An Experimental Study of Boundary Layer Transition Induced by a Cylinder Wake", Journal of Fluid Mechanics **684**, 60–84 (2011).

[134]T. A. Zaki and P. A. Durbin, "Mode Interaction and the Bypass Route to Transition", Journal of Fluid Mechanics **531**, 85–111 (2005).

[135]C. R. Smith and S. P. Metzler, "The Characteristics of Low-Speed Streaks in the Near-Wall Region of a Turbulent Boundary Layer", Journal of Fluid Mechanics **129**, 27 (1983).